

# Some Topics in the Physics of Solar Flares

*A thesis submitted for the degree of  
Doctor of Philosophy*

by

Michael Scott Wheatland

*Research Centre for Theoretical Astrophysics  
School of Physics  
University of Sydney  
Australia*

*January 1995*

*To Nola*

“I find my zenith doth depend upon  
A most auspicious star, whose influence  
If I court not, but omit, my fortunes  
Will ever after droop.”

*The Tempest, I, ii.*

# Contents

<b>1</b>	<b>Solar flare physics - an overview</b>	<b>1</b>
1.1	Introduction . . . . .	1
1.2	Flare observations . . . . .	2
1.2.1	Solar flare X-ray emission . . . . .	3
1.2.2	Currents at the photosphere . . . . .	6
1.3	Flare theories . . . . .	6
1.3.1	Energy release mechanisms . . . . .	7
1.3.2	Sources of magnetic free energy . . . . .	8
1.3.3	Energy propagation into the flare site . . . . .	9
1.3.4	Specific problems with the viewpoints . . . . .	10
1.4	Conclusions . . . . .	11
<b>2</b>	<b>Energy propagation into a flare energy release site</b>	<b>12</b>
2.1	Introduction . . . . .	13
2.1.1	The existing model . . . . .	13
2.1.2	Towards a more realistic treatment . . . . .	17
2.2	The impulsive turning-off of energy release . . . . .	17
2.2.1	Timescales for energy release and resupply . . . . .	19
2.3	The gradual turning-on of energy release . . . . .	20
2.4	Towards a force-free model . . . . .	23
2.5	Zaitsev and Stepanov: accounting for $R_c$ ? . . . . .	28
2.6	Conclusions . . . . .	31
2.7	APPENDIX . . . . .	33
2.7.1	Derivation of Equations (2.8)—(2.10) . . . . .	33
<b>3</b>	<b>Interpreting Yohkoh hard and soft X-ray flare observations</b>	<b>36</b>
3.1	Introduction . . . . .	37

3.2	Accounting for a loop-top source . . . . .	40
3.3	A detailed model for the spectra of the loop-top and footpoint sources . . . . .	41
3.3.1	Evolution of the electron flux spectrum . . . . .	41
3.3.2	The photon spectrum from the loop-top . . . . .	42
3.3.3	The photon spectrum from the footpoints . . . . .	43
3.3.4	The photon spectrum from between the loop-top and footpoints . . . . .	43
3.3.5	Behaviour of model spectra . . . . .	44
3.3.6	Ratio of count rates . . . . .	45
3.3.7	A modified model . . . . .	46
3.4	Comparison with Masuda's observations . . . . .	47
3.4.1	Masuda's spectral indices . . . . .	47
3.4.2	The break in spectral index . . . . .	49
3.4.3	Behaviour at high and low energies . . . . .	49
3.4.4	Type A flare observation . . . . .	50
3.4.5	Relative brightness of the footpoints and loop-top . . . . .	52
3.5	The heating of the loop-top source . . . . .	52
3.5.1	The energy deposited at the loop-top . . . . .	52
3.5.2	Comparison with the observed heating . . . . .	54
3.6	Discussion . . . . .	55
3.7	Conclusions . . . . .	56
3.8	APPENDIX . . . . .	59
3.8.1	Derivation of Equations (3.2)—(3.5) . . . . .	59
3.8.2	Derivation of Equations (3.6) and (3.7) . . . . .	61
<b>4</b>	<b>Cross-field current closure below the solar photosphere</b>	<b>62</b>
4.1	Introduction . . . . .	63
4.2	Description of subphotospheric currents . . . . .	67
4.3	Model for response of the subphotosphere to a current imposed from above . . . . .	69
4.4	Limiting cases . . . . .	71
4.4.1	Infinite conductivity ( $\gamma \rightarrow \infty$ ) . . . . .	71
4.4.2	Zero Alfvén speed ( $v_A \rightarrow 0$ ) . . . . .	72
4.4.3	Steady state ( $t \rightarrow \infty$ ) . . . . .	73

4.4.4	An approximation valid for large conductivity . . . . .	75
4.5	The general case . . . . .	76
4.6	Discussion . . . . .	80
4.7	Line-tying revisited . . . . .	81
4.7.1	A reflection coefficient for the photosphere . . . . .	82
4.7.2	Comparison with the Earth's magnetosphere . . . . .	85
4.8	Modelling the shearing of an arcade . . . . .	87
4.8.1	A two-dimensional model . . . . .	88
4.8.2	The role of the subphotosphere . . . . .	92
4.9	Conclusions . . . . .	95
4.10	APPENDIX . . . . .	97
4.10.1	Derivation of Equation (4.6) and discussion of the use of Equation (4.4) . . . . .	97
4.10.2	Derivation of Equation (4.15) . . . . .	99
4.10.3	Derivation of Equation (4.18) from (4.15) . . . . .	100
<b>5</b>	<b>An equivalent circuit for Alfvén waves in a stratified atmosphere</b>	<b>101</b>
5.1	Introduction . . . . .	102
5.2	Alfvén waves in a stratified atmosphere . . . . .	103
5.3	Alfvén waves in an exponential atmosphere . . . . .	104
5.3.1	A bi-exponential chromosphere . . . . .	106
5.3.2	The input impedance . . . . .	108
5.3.3	An equivalent circuit when $\Lambda_1 = \Lambda_2$ . . . . .	109
5.3.4	An equivalent circuit when $\Lambda_1 \neq \Lambda_2$ . . . . .	110
5.4	Conclusions . . . . .	111
5.5	APPENDIX . . . . .	113
5.5.1	The transmission line equations . . . . .	113
5.5.2	Interpreting the input impedance . . . . .	113
	REFERENCES . . . . .	115

# List of Figures

1.1	A typical X-ray spectrum from a flare. (From Tanaka, 1986.) . . .	4
1.2	The vertical current density derived for an active region by Ding <i>et al.</i> (1987) . . . . .	7
2.1	A simple model for the expansion of the force-free flux tube . . .	26
2.2	A schematic diagram of Zaitsev and Stepanov's (1991; 1992) flare model . . . . .	29
3.1	The coaligned hard and soft X-ray images obtained by Masuda (1994). (From Kosugi, 1994.) . . . . .	39
3.2	The electron flux injection spectrum $F = F(E, N_0)$ for the foot- point source . . . . .	43
3.3	The scaled photon spectra . . . . .	45
3.4	The ratio $r(\epsilon > \epsilon_0)$ . . . . .	46
3.5	The time history of hard X-ray emission for the flare of December 6, 1992. (From Masuda, 1994.) . . . . .	51
3.6	The fraction of electrons stopped at the loop-top . . . . .	53
4.1	A theoretical model for the shearing of a coronal arcade . . . . .	65
4.2	Kuperus and Raadu's (1974) model for the support of a current- carrying filament . . . . .	66
4.3	The geometry of the simple model photosphere considered . . . . .	68
4.4	The scaled current density . . . . .	73
4.5	The vector field of the current density . . . . .	74
4.6	$J_x(x = 0, z, t)/(I_0/l)$ for the case $R_M = 10$ . . . . .	77
4.7	The cross-field current density . . . . .	78
4.8	$J_x(x = 0, z, t)/(I_0/l)$ for the case $R_M = 1$ . . . . .	78
4.9	Scaled current density $J_x(x = 0, z, t)/(I_0/l)$ in the photosphere . .	79

4.10	The fraction of the total current $I_0$ closing in the first characteristic length . . . . .	80
4.11	The generalised reflection coefficient . . . . .	85
4.12	The velocity of the impinged medium . . . . .	86
4.13	The geometry of a coronal magnetic arcade . . . . .	89
4.14	The shearing of the arcade is assumed here to be driven by a sub-photospheric layer of thickness $L$ . . . . .	93
5.1	The transmission line derived for Alfvén wave propagation in a stratified atmosphere . . . . .	105
5.2	The geometry of the model for Alfvén wave propagation in a bi-exponential chromosphere . . . . .	107
5.3	The constituent element for the transmission line, representing the change in impedance between $z$ and $z + \delta z$ . . . . .	113

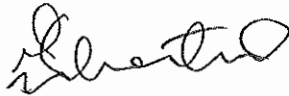
# List of Tables

3.1	The spectral indices derived by Masuda (1994) . . . . .	48
-----	---	----



# Declaration of originality

This thesis contains no material which has been presented for a degree at this or any other university. To the best of my knowledge and belief, this thesis contains no copy or paraphrase of work published by another person, except where duly acknowledged in the text.

A handwritten signature in black ink, appearing to read 'Michael Wheatland', written in a cursive style.

Michael Wheatland

# Acknowledgements

I would like to thank my supervisor, Don Melrose, for his consistent support during the last three years, his good humour, and for his insight into solar physics. I also thank the Solar Theory group at the University of St. Andrews, Scotland, for their hospitality during my visit there. The members of the Theoretical Physics Department and the RCfTA also deserve thanks for their help at different times, and in particular I extend thanks to my fellow students. I thank my family for their support and encouragement, and Nola for her unfailing belief in me.

I also acknowledge the financial support provided by an Australian Post-graduate Research Award.

# Publications

The following publications are based on material contained within this thesis:

1. Wheatland, M. S. and Melrose, D. B., (1994) "Alfvénic fronts and the turning-off of the energy release in solar flares," *Proceedings of the Astronomical Society of Australia*, **11**, 25–27.
2. Wheatland, M. S. and Melrose, D. B., (1994) "Cross-field current closure in the solar photosphere," *Australian Journal of Physics*, **47**, 361–374.
3. Wheatland, M. S. and Melrose, D. B., (1994) "Interpreting Yohkoh hard and soft X-ray flare observations," submitted to *Solar Physics*.
4. Wheatland, M. S. and Melrose, D. B., (1994) "Energy release in a prominence-loaded flaring loop," submitted to *Solar Physics*.

Paper 1 and paper 4 are based on material in chapter 2; paper 2 is based on material in chapter 4; and paper 3 is based on material in chapter 3.

# Summary

In this thesis the emphasis is on the magnetohydrodynamical description of processes associated with solar flares. A brief review of both the observational and theoretical aspects of solar flare physics is presented in chapter 1, which provides a context for the individual topics addressed.

In chapter 2, energy propagation into the site of energy release in a solar flare is studied in detail, in the context of an existing model. The existing model describes the unwinding of a twisted magnetic flux tube when a dissipative region turns on somewhere along its length; the dissipative region is a simple model for the primary site of energy release in a flare. It is shown that the evolution of the system after the termination of energy release leads to a resupply of energy to the coronal part of the flux tube, thereby providing a simple model for the phenomenon of homologous flaring. It is also shown that the model can be generalised to describe a time dependent, rather than impulsive, turning-on and -off of energy release, and the generalisation of the model to describe the same processes in a force-free flux tube is also investigated. Chapter 2 concludes with a critical examination of a particular energy release mechanism, due to Zaitsev and Stepanov (1991; 1992). It is shown that this mechanism does not constitute a tenable flare model.

Chapter 3 of this thesis is concerned with the interpretation of several hard and soft X-ray flare observations made with the Yohkoh spacecraft. A model is presented to account for the loop-top hard X-ray sources found by Masuda (1994) and the soft X-ray observations of Feldman *et al.* (1994). Electrons accelerated by the flare energy release mechanism near the apex of a coronal loop are assumed to encounter an intermediate thick-thin target in an overdense loop-top region. Some of the energised electrons are stopped at the loop-top, and some precipitate to the footpoints of the loop. The model predicts theoretical photon spectra for the loop-top dense region and the footpoints of the loop which qualitatively agree with the observations of Masuda (1994). The model also accounts for the heating

of the dense loop-top region, and provides a natural explanation for Type A flare observations.

In chapter 4, a simple, two-dimensional model is presented to describe how an externally imposed current closes as a function of time beneath the photosphere. The model shows that currents close in a given layer of the subphotosphere only during an Alfvén propagation time of that layer. The implication is that currents observed at the solar photosphere close along field lines beneath the photosphere, a conclusion inconsistent with the boundary condition of line-tying, often imposed to describe the behaviour of plasma and fields at the photospheric boundary. The implications of this conclusion for the dynamics of coronal magnetic structures are then investigated. A simple model for the shearing of a magnetic arcade is presented, and it is shown that if one side of the arcade is driven continuously, the other row of footpoints is set into motion as well, with a timescale determined by the transfer of momentum between footpoints. The role of the subphotosphere in this process is investigated, and it is shown that if a finite layer of subphotosphere at one footpoint of an arcade is initially set into motion, the propagation of Alfvénic fronts into the subphotosphere at that footpoint effectively brakes the driving motion.

Chapter 5 presents a circuit model for Alfvén wave propagation in a stratified atmosphere. The model extends the analysis of Scheurwater and Kuperus (1988) to describe vertically propagating Alfvén waves in an atmosphere with arbitrary density and conductivity profiles. By way of example, the model is applied to waves in an infinitely conducting, exponential atmosphere.

# Chapter 1

## Solar flare physics - an overview

### 1.1 Introduction

Solar flares are events in which energy is explosively released in the solar atmosphere. Typically the energy release is  $10^{22} - 10^{25}$  J in  $10^2 - 10^3$  s, making solar flares the most energetic events in the solar system. The motivation to understand flares has been driven in part by the practical consideration that large solar flares have associated terrestrial effects, e.g. interruptions to radio communications, although it has recently been argued (Gosling, 1993; cf. Hudson *et al.* 1994 however) that the principal culprits in this respect are the related solar phenomena, coronal mass ejections (CMEs). Solar flares produce radiation ranging from radio frequencies to extremely energetic gamma rays. Flares have long been observed as  $H\alpha$  events at the chromosphere, but in recent years the focus has been on the information provided by solar flare hard X-ray emission. The Japanese Institute of Space and Astronomical Science satellite Yohkoh, launched in 1991, has provided the most detailed hard and soft X-ray observations to date.

Despite decades of intensive theoretical and observational work, the fundamental question of solar flare physics – the mechanism of energy release – remains unresolved. The only general agreement is that the source of the energy must be the magnetic fields above the active regions in which flares occur. A wealth of indirect evidence suggests that the site of energy release is in the corona (Švestka, 1976), and X-ray observations imply that a substantial fraction of the impulsive energy release goes into producing 10 – 100 keV electrons (Dennis, 1988). The interaction of these electrons with the ambient solar plasma produces the variety of observed flare emission. However, the mechanism of electron acceleration in

a flare is not understood, and there is no accepted theory for how the energy in coronal magnetic fields appears as energetic particles (Melrose, 1990).

This chapter presents a brief overview of solar flare physics, and provides a context for the specific topics addressed in this thesis. More comprehensive surveys of the field may be found in the literature (e.g. Švestka, 1976; Brown and Smith, 1980; Melrose, 1993). In §1.2 below, solar flare observations are briefly reviewed, with the emphasis on hard and soft X-ray emission and observations of photospheric magnetic fields. In §1.3 the present state of theoretical understanding of solar flares is surveyed, with the emphasis on topics discussed in this thesis.

## 1.2 Flare observations

There is an enormous body of literature devoted to flare observations, and no existing flare model can account for all of the details. The following is a brief summary of some important observations.

Flares are observed to occur in active regions, i.e. sites containing one or more bipolar regions. The most active of active regions are those with a complicated, rather than simple bipolar, magnetic topology. In particular, active regions with a ‘ $\delta$ -configuration’ (i.e. having both polarities occurring within a common penumbra) are usually sites of repeated flaring (Švestka, 1976; Zirin, 1988), although only if the polarities comprising the  $\delta$ -configuration are magnetically connected (Rust *et al.* 1994). Flares may re-occur periodically in the same part of an active region; these events are known as homologous flares (Švestka, 1976).

Flare observations began with the sighting, in 1859, of a brightening in white light on the solar disk. White-light flares visible to the naked eye are rare events, however. Until about the 1970s, flares were studied almost exclusively as chromospheric brightenings in  $H\alpha$ , and the name ‘flare’ derives from their appearance in  $H\alpha$ . The area of brightening is proportional to the power released in the flare, and a detailed classification scheme is applied to describe flares as they appear in  $H\alpha$ . The impulsive phase of flaring is also characterised by the production of hard X-rays (see below), soft X-rays (due to  $\geq 10^7$  K plasma appearing in the corona), type III radio bursts (due to electron beams propagating outward through the corona), spike radio bursts (see below),  $\gamma$ -ray lines (produced by the prompt acceleration of  $> 40$  Mev ions), and a  $\gamma$ -ray continuum (attributed to

relativistic electrons).

Flares have been classified by their geometry in  $H\alpha$  into the following two classes. *Two-ribbon flares* are observed on the solar disc as two extended, separating bands of  $H\alpha$  emission running parallel to the magnetic neutral line of an active region, which is marked by a filament, or prominence (Švestka, 1976). *Compact flares* are indeed more compact, may occur well away from the neutral line of a given region, and are not necessarily associated with a filament (Moore *et al.* 1980). Two-ribbon flares are associated with a magnetic arcade geometry, whereas compact flares are associated with individual magnetic loops. The majority of flares and sub-flares are compact, whereas almost all major (i.e. very energetic) flares are two-ribbon events. The impulsive phase of large (two-ribbon) flares is often accompanied by a CME, but the relationship between flares and CMEs is not one of simple causality (e.g. Hudson *et al.* 1994).

### 1.2.1 Solar flare X-ray emission

Even the smallest flares observed in  $H\alpha$  produce hard X-ray emission which is now considered the basic signature of impulsive flaring. The onset of hard X-ray emission contains information about the earliest possible time after the flare energy release (with the possible exception of spike radio bursts, described below). In practice, however, it is difficult to extract reliable information about the energetic electron population responsible for the X-rays (and about plasma conditions at the source) from the observed emission.

Solar flare hard X-ray emission is attributed to electron-ion bremsstrahlung, either thermal or non-thermal. Thermal bremsstrahlung is the result of electron-ion collisions in a hot plasma, whereas non-thermal bremsstrahlung is the result of an energetic electron beam interacting with ambient plasma. A simple non-thermal model for impulsive solar flare X-ray emission is the thick-target model (Brown, 1971). In this model, a beam of electrons (with a power law distribution of energy,  $> 20$  keV, say) is produced in the corona by the flare energy release mechanism and precipitates to the chromosphere where it is completely stopped. Thick-target emission naturally produces a power law photon spectrum, characterised by spectral index,  $\gamma$ , which is qualitatively consistent with spectral observations of solar flares. Typically the (early) spectra of impulsive flares are power laws over the 10 – 100 keV range, with a thermal contribution at lower energies. Figure 1.1 shows a typical spectrum. Observations do not, however, conclusively



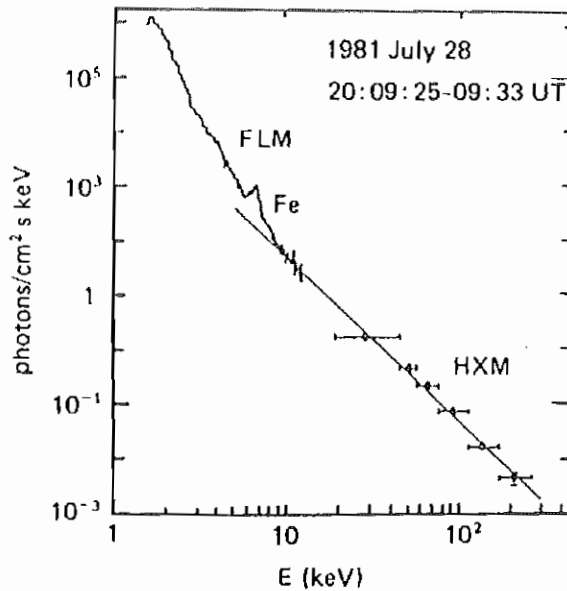


Figure 1.1: A typical X-ray spectrum from a flare, showing the transition from thermal emission at low energies ( $\leq 10$  keV) to power-law hard X-ray emission. FLM and HXM refer to the instruments used in the respective observations. (From Tanaka, 1986.)

rule out thermal models (e.g. Brown *et al.* 1979), since a non-isothermal source at  $10^8$  K could also produce the observed power law emission.

Solar flare soft X-ray emission is unambiguously attributed to thermal bremsstrahlung from plasma at a temperature  $T \geq 10^7$  K. The origin of the soft X-ray emitting plasma is, however, disputed. A popular model is the ‘chromospheric evaporation’ picture, in which the soft X-ray plasma is dense chromospheric material, ablated or evaporated into the corona by the deposition of energy at the chromosphere by precipitating electrons (Doschek *et al.* 1990).

Solar flare hard X-ray observations, interpreted in terms of the thick-target model, imply that  $10^{35} - 10^{36}$  energetic electrons ( $> 20$  keV) precipitate per second in a typical flare. The inferred flux of electrons is very large because of the low efficiency of thick-target bremsstrahlung. Such a flux would evacuate the electrons out of a typical coronal volume in minutes, but theoretical studies suggest that a return current of electrons is established (van den Oord, 1990). The high flux of electrons also implies that a substantial fraction of the total flare energy goes into energising electrons, although the actual fraction is sensitively dependent on the lower cut-off to the electron distribution, which is not well constrained (Dennis,

1988).

An X-ray classification scheme for flares was proposed following the Solar Maximum Mission satellite observations (Dennis, 1988):

*Type A, or hot thermal flares:* Characterised by a gradual rise and fall of hard X-ray; spectrum well fitted by thermal bremsstrahlung with  $T \approx 3 - 4 \times 10^7$  K; very steep spectra above 40 keV with an index  $\gamma \geq 7$ ; spatially compact.

*Type B, or impulsive flares:* Impulsive, spiky hard X-ray with a variability of seconds; soft-hard-soft spectral evolution.

*Type C, or gradual-hard flares:* Gradually varying hard X-ray emission over  $\geq 30$  min; spectrum above 50 keV hardens from  $\gamma \geq 5$  to  $\gamma \leq 2$ .

The vast majority of flares are of Type B; a few percent belong to the other two classes, although a given flare may show characteristics of more than one type. It is also worth noting that Lin *et al.* (1981) studied the spectral evolution of an impulsive (Type B) flare and showed the development, from late in the impulsive phase, of a thermal component at  $T \approx 3 \times 10^7$  K which dominates the spectrum below about 50 keV.

The Yohkoh satellite, launched in 1991, has provided the most detailed soft and hard X-ray images of solar flares to date (Hudson, 1994; Kosugi, 1994). Chapter 3 of this thesis is concerned with the interpretation of a number of hard and soft X-ray observations made with Yohkoh. The model developed in chapter 3 also challenges the validity of chromospheric evaporation models.

High time resolution hard X-ray observations show the existence of rapid fluctuations in flare X-ray emission (with a timescale of seconds), and the fluctuations are thought to be composed of 'elementary flare bursts', or EFBs (Sturrock, 1986). More fundamental, sub-EFB structure ( $\approx 100$  ms) has recently been reported (Brown *et al.* 1994). The finest structure is observed in radio spike bursts (Benz, 1985; 1986). An individual flare may produce as many as  $10^4$  spikes, each with a duration of about 50 ms. Benz (1985; 1986) interpreted these events as the signature of the primary acceleration of electrons in small (200 km) regions of energy release, or 'microflares'. Each microflare must produce  $10^{21}$  J in 50 ms. A comparison of millisecond radio spikes with hard X-ray emission (Aschwanden and Güdel, 1992) demonstrated that the radio bursts correlate with, but occur 2 - 5 s after, the hard X-ray. This result complicates the simple interpretation of Benz.

### 1.2.2 Currents at the photosphere

Flares occur in active regions where the magnetic field is strongly sheared across the neutral line (Moore *et al.* 1987; Machado *et al.* 1988), implying the presence of large currents. The three-dimensional magnetic field of the active region at the photosphere can be determined by the three Zeeman components, and hence the line of sight current can be calculated from Ampere's law applied to the transverse components of magnetic field (e.g. Moreton and Severny, 1968; Hagyard, 1988; Canfield *et al.* 1993; de La Beaujardière *et al.* 1993; Leka *et al.* 1993). The maps of magnetic field obtained in this way are known as vector magnetograms. Vector magnetograms confirm that flares correlate with regions where large currents flow through the photosphere (Krall *et al.* 1982; Ding *et al.* 1987; Lin and Gauzauskas, 1987; Romanov and Tsap, 1990). Typically the currents are observed to flow out of the photosphere on one side of the neutral line of an active region, and back into the photosphere on the other. Figure 1.2 shows a vector magnetogram derived for a particular active region. The questions of how these currents are generated, and how they relate to energy stored (and released) in solar flares, remain incompletely answered. A related problem (addressed in chapter 4 of this thesis) is the question of where the observed currents close. As explained below, this problem is relevant to a class of models for energy storage prior to a flare.

## 1.3 Flare theories

In this section, a brief overview is presented of some of the outstanding theoretical problems in solar flare physics. No attempt is made to provide a complete summary of individual flare models.

Solar flares theories divide into those based on the magnetic viewpoint, and those based on the electric current viewpoint (Melrose, 1993). Models based on the electric current viewpoint are also referred to as circuit models. It should of course be irrelevant whether a theoretical description of a flare follows the evolution of magnetic fields or the currents associated with those fields, but in practice the two perspectives are irreconcilable because of specific assumptions made in the respective models. An example of the magnetic viewpoint is the 'emerging flux' flare model due to Heyvaerts *et al.* (1977). The prototype flare model in the circuit viewpoint is the Alfvén and Carlqvist (1967), 'current interruption' model.

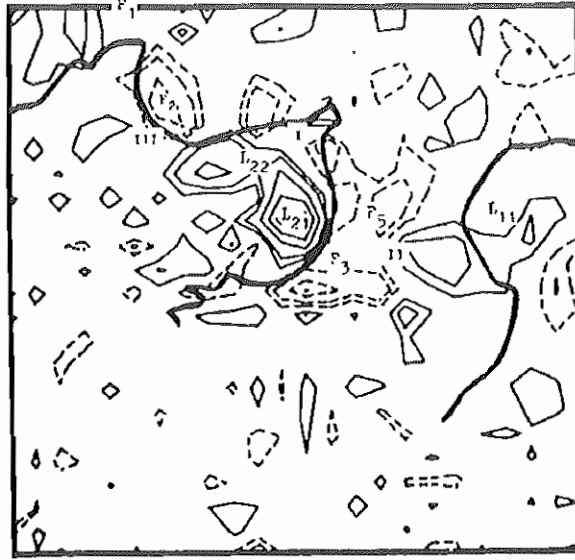


Figure 1.2: The vertical current density derived for an active region by Ding *et al.* (1987). The solid (dashed) contours represent current flowing out of (into) the photosphere, and the heavy solid line follows the magnetic neutral line of the active region.

The distinction between the electric current and magnetic viewpoints is evident in the respective approaches to the source of flare energy, the storage of flare energy, the propagation of energy into the energy release site, and most importantly, the mechanism of energy release.

### 1.3.1 Energy release mechanisms

In the electric current viewpoint, energy release in a flare is attributed to the local appearance of a resistivity,  $\eta$ , associated with a field-aligned current density  $\mathbf{J}$  in a coronal magnetic loop. Integrating  $\eta J^2$  over the energy release site gives the power,  $RI^2$ , associated with the flare, where  $R$  is a resistance assigned to the flaring loop. Classical estimates of  $R$ , however, do not adequately account for the power associated with even modest flares, and it is necessary to appeal to some form of anomalous resistivity (Melrose and McClymont, 1987). Chapter 2 of this thesis includes a critical examination of the specific mechanism of Zaitsev and Stepanov (1991; 1992) for producing enhanced resistance in a flaring coronal loop. More generally, the natural choice for providing anomalous resistivity in a current-carrying, flaring coronal loop is a current-driven instability.

In the magnetic viewpoint, the energy released in a flare is attributed to the

magnetic reconnection (or annihilation) of coronal magnetic fields. However, the high classical conductivity of the coronal plasma implies that field lines are frozen into the plasma and so precludes a change in magnetic topology. The resolution of this problem (cf. the appeal to anomalous resistivity in the electric current viewpoint) is to invoke reconnection at specific sites in the magnetic field (viz. neutral lines, or X-points) where the frozen-in condition is locally broken. Theoretical descriptions of reconnection are generally local, two-dimensional models of the fluid behaviour around the neutral point, which is co-spatial with one or more current sheets (e.g. Vasylunas, 1975; Priest, 1982). The magnetic field is antiparallel either side of a current sheet, and perpendicular to the current in the sheet. This is in contrast to the electric current picture, where the current associated with dissipation is field-aligned (Spicer and Brown, 1980). Flare models adopting the magnetic viewpoint are generally two-dimensional, and follow the procedure of identifying the location of an X-point or current sheet in a two-dimensional model of the coronal magnetic field above an active region, and attributing the flare energy release to that site. Recently, the three-dimensional magnetic topology above an active region has been considered (Priest, 1992). The X-point is replaced by a separator, a curve defined by the intersection of two separatrices (surfaces dividing magnetically disjoint regions). Although three-dimensional theoretical models of magnetic reconnection are still an active area of research (Priest and Forbes, 1989; Lau and Finn, 1990; Hesse, 1991), energy release is expected to be associated with a current along a separator.

### 1.3.2 Sources of magnetic free energy

As mentioned above, another distinction between the electric current and magnetic viewpoints is the identification of the source of the magnetic energy released in a flare (McClymont and Fisher, 1989). In electric current based models, the field-aligned currents involved are identified with those inferred at the photosphere from vector magnetograms. These currents are generally attributed to the solar dynamo (Hudson, 1987). In the magnetic viewpoint, the source of flare energy is generally assumed to be the stressing of coronal magnetic fields by photospheric velocity fields, or by emerging flux; the so called coronal storage models. For example, a wide body of literature attributes the build-up of energy in a two-ribbon flare to the gradual shearing of a coronal magnetic arcade by incompatible photospheric flows at the two rows of footpoints of the arcade (e.g. Low, 1977).

Two arguments against such a mechanism for flare energy storage are mentioned here. The first is that the current patterns inferred from vector magnetograms are inconsistent with those expected if shearing motions are the generators of the relevant currents (Melrose, 1991). A contrary opinion was, however, presented by Wilkinson *et al.* (1992). Another argument against models for the storage of energy in a coronal magnetic structure due to photospheric shearing is that the models presented implicitly impose unphysical boundary conditions on currents at the photosphere. Models for the shearing of arcades typically invoke the ‘line-tying’ boundary condition on fields at the photosphere. As argued in chapter 4 of this thesis, line-tying implicitly requires that currents close across field lines in the photospheric boundary. Chapter 4 presents an investigation of current closure in the subphotosphere and then reconsiders the shearing of a coronal arcade.

It is a general feature of models based on the magnetic viewpoint that the associated currents are incompatible with, or more generally not related to, those inferred from vector magnetogram data. The current sheets of interest in magnetic reconnection are not expected to be observable (Brown *et al.* 1994). A recent attempt to relate the magnetic viewpoint and vector magnetogram data involved the calculation of the magnetic connectivity of an active region from the extrapolation of the observed photospheric field into the corona (Van Driel-Gesztelyi *et al.* 1994). In particular, the intersections of the separatrices and separators with the photosphere were calculated and compared with the inferred currents. Brown *et al.* (1994) concluded that the results support the idea that the energy released in a flare is that stored in field-aligned currents in bipoles, rather than associated with currents along the calculated separators.

### 1.3.3 Energy propagation into the flare site

Models based on the magnetic and electric current viewpoints also differ fundamentally in their approach to energy propagation in a flare. Due to the emphasis on a local description in models based on the magnetic viewpoint, the question of global energy propagation into the site of energy release in a flare is generally neglected. This becomes relevant if, for example, magnetic energy stored everywhere in a flaring loop is supposed to supply energy release at a specific location in the loop. Then the energy propagation to the site of release must be predominantly field-aligned. In the local description of the magnetic viewpoint, however, the Poynting flux of energy to the dissipative region is perpendicular to the field.

The need to reconcile these differences motivated the model for energy transport in a solar flare of Melrose (1992). In chapter 2 of this thesis, this theoretical description of energy transport is re-investigated and extended.

Circuit models of solar flares naturally provide a global description of the energetics of a flare, but often omit some of the relevant plasma physics in their ‘lumped parameter’ approach. In particular, the propagation of energy in a flaring loop is generally neglected because the simple circuits invoked do not describe the propagation of Alfvén waves. The model developed in chapter 2 of this thesis provides a detailed magnetohydrodynamic description of energy propagation into the site of energy release in a flare, and it is shown that the long term behaviour of the model can be predicted by a simple circuit analogy. In addition, chapter 5 of this thesis extends the circuit description of Alfvén wave propagation due to Scheurwater and Kuperus (1988) to describe Alfvén wave propagation in a stratified atmosphere.

### 1.3.4 Specific problems with the viewpoints

The discussion above is sufficient to show that there is no satisfactory flare model, from either the magnetic, or the electric current viewpoint. Furthermore, it is not clear how to produce a complementary model, i.e. a model which incorporates both aspects. The most serious shortcomings of each viewpoint may be summarised as follows:

1. Neither approach resolves the details of energy release. In the magnetic viewpoint, the problem is that the existence of explosive reconnection is still a matter of theoretical speculation (Akasofu, 1984; 1994), despite decades of intensive research. In the electric current viewpoint, the central problem remains the identification of the relevant current instability.
2. Neither viewpoint naturally accounts for the acceleration of  $> 20$  keV electrons, at a rate of  $10^{35} - 10^{36} \text{ s}^{-1}$ , as inferred from hard X-ray observations (Melrose, 1990).
3. Energetics arguments imply a fragmentation of energy release (independent of the specific model, or viewpoint) and so it is necessary to account for the production and interaction of many reconnection regions, or sites of

anomalous resistivity (Sturrock, 1986; Melrose, 1993). As discussed above, EFBs and spike radio bursts also point to a fragmentation of energy release.

4. Models adopting the magnetic viewpoint fail to associate the currents involved in energy release (the current sheets) with the currents inferred at the photosphere from vector magnetograms.
5. Current viewpoint-based models are generally circuit models and so omit some of the relevant plasma physics in favour of a lumped parameter description (Melrose, 1993).

## 1.4 Conclusions

Solar flares are energetic events in the solar corona, involving the explosive release of energy stored in stressed coronal magnetic fields. Despite decades of theoretical and observational work, the details of the mechanism of energy release in flares, as well as the storage of energy prior to release and the ultimate source of that energy, remain incompletely understood.

Theoretical models of flares are based on either the magnetic viewpoint, or the electric current viewpoint. No individual model can account, even qualitatively, for the bulk of flare observations. Dramatic improvements in the resolution of observations (e.g. from the Yohkoh spacecraft, and its successor, Solar B) may resolve some of the outstanding questions, but substantial theoretical progress is also required. In particular, the reconciliation of the differences between the magnetic and electric current viewpoints will be a long overdue first step.

This thesis is concerned with several topics in solar flare physics, including the interpretation of solar flare hard and soft X-ray emission (as observed with the Yohkoh satellite), the theoretical description of energy propagation in a solar flare, and the closure of currents observed at the photosphere (and associated with flares) below the photosphere.



## Chapter 2

# Energy propagation into a flare energy release site

**Abstract:** Several refinements of an existing model for energy propagation into the primary energy release site in a solar flare (Melrose, 1992) are presented. The existing model describes the unwinding of a twisted magnetic flux tube when a dissipative region turns on somewhere along its length. The dissipative region is a simple model for the primary site of energy release in a flare. The unwinding of the flux tube, and the flux of energy into the dissipative region is effected by Alfvénic fronts that propagate away from the dissipative region. The evolution of the system after the flare energy release ends is considered, as well as the generalisation of the model to describe time-dependent (rather than impulsive) turning-on and -off of energy release, and the changes necessary to describe the same processes in a force-free coronal flux tube.

A critical discussion is also presented of the flare energy release mechanism presented by Zaitsev and Stepanov (1991; 1992).

## 2.1 Introduction

A solar flare involves the release of magnetic energy from a current-carrying, or equivalently, twisted coronal magnetic loop. The primary energy release site is assumed here to be located near the apex of the loop. If energy stored globally (i.e. everywhere in the loop) is continuously released locally (near the apex of the loop), a mechanism is required for energy propagation into the energy release site. That propagation must be predominantly field-aligned, as distant regions of the loop supply energy to a dissipative process occurring at its apex.

Most models for solar flares invoke magnetic reconnection as the energy release mechanism. In the standard, X-type neutral point description of reconnection, the energy propagation into the dissipative region occurs perpendicular to the magnetic field. In any realistic flare model based on reconnection, this local description must be reconciled with the global requirement that the mean energy flow into the flare site is field-aligned.

### 2.1.1 The existing model

These considerations motivated an existing model for field-aligned energy propagation in a flare (Melrose, 1992). In Melrose's model, the energy release site is represented by a dissipative region in a cylindrical flux tube carrying a current  $I$ . The power release in the flare (typically  $10^{21}$ – $10^{22}$  W for a large flare) may be equated to  $I^2 R_c$ , to define a characteristic resistance  $R_c$  for the dissipation. The dissipative region is also referred to here as the *resistive* region.

The mechanism for dissipation in the resistive region is not addressed directly in Melrose's model. The dissipation mechanism in solar flares is not well understood and  $R_c$  is introduced only as a simple way of relating the dissipation to the current  $I$ . This step is motivated by observational evidence that flare regions correlate with regions of high current ( $I \approx 10^{12}$  A) flowing into the corona (Moreton and Severny, 1968; Krall *et al.* 1982; Ding *et al.* 1987; Lin and Gaizauskas, 1987; Hagyard, 1988; Romanov and Tsap, 1990; Canfield *et al.* 1993; Leka *et al.* 1993; de La Beaujardière *et al.* 1993). The failure of the existing model to describe the microphysics of the resistive region is not addressed here, beyond a few comments. It has been widely recognised that the classical (Spitzer) resistivity of coronal plasma is insufficient by many orders of magnitude to account, by Ohmic dissipation, for the power release of even a modest flare (Melrose and McClymont,

1987). Specifically, the (classical, Spitzer) coronal resistance is of order  $10^{-12}$ – $10^{-11} \Omega$ , whereas the estimates of power release and current for a flaring coronal loop quoted above imply  $R_c \approx 10^{-4}$ – $10^{-3} \Omega$ . It is necessary to appeal to some form of anomalous resistivity to account for this dramatic increase in resistance. The existing model is biased in favour of a central dissipative region consisting of field-aligned double layers. Raadu (1989) and recently Volwerk (1993) considered an analogous model in which the dissipative region consists of a single, macroscopic double layer. Energetics arguments (Melrose, 1990) imply that the flare energy release must be a fragmented process and so it is necessary to appeal to a filamented energy release region involving many double layers (Khan, 1989) rather than a single, macroscopic double layer.

Recently, Zaitsev and Stepanov (1991; 1992) presented a model to account for the requisite eight to ten orders of magnitude increase in the resistance of a flaring coronal loop. A prominence, or filament overlying a coronal loop is supposed to intrude into the loop via an instability, thereby introducing dense plasma and non-steady state conditions near the loop apex, and providing the trigger for a flare. Zaitsev and Stepanov argued that the dense neutral gas and non-steady state conditions account for the increased resistance. Their mechanism is critically examined in §2.5 of this chapter and is found to be based on the erroneous assumption of non force-free conditions in the coronal loop before the intrusion of the filament.

In the existing model for energy propagation into a solar flare, the resistive region is assumed to turn on impulsively at a time  $t = 0$  in the cylindrical flux tube, modelling the impulsive onset of a flare. The flux tube is threaded by a uniform axial magnetic field with magnitude  $B_0$ . The ends of the flux tube represent the photospheric boundaries and the resistive region is represented by a cylindrical disk at the midpoint of the flux tube. The system is described in terms of cylindrical coordinates  $r, \phi, z$  with origin in the resistive region. The radius of the flux tube is  $r_0$  and its length is  $l$ . Alfvénic fronts are launched along field lines away from the central dissipative disk in response to the sudden appearance of the cross field potential implied by  $R_c$ . Goertz and Boswell (1979) provide a kinetic theory description of this process in the context of a model for magnetosphere-ionosphere coupling. The Alfvénic fronts carry behind them a new current density but the same current still flows in the loop, to satisfy the requirement that the current itself only change over the longer, inductive

timescale of the current loop circuit (Melrose, 1993). Effectively, a fraction of the current  $I$  is deflected to the surface of the flux tube in the plane of the advancing front and thereby avoids flowing through  $R_c$ . For simplicity it is assumed that a purely axial current with uniform density  $J_0$  flows in the flux tube initially, and is replaced by a purely axial current with constant current density  $J_1$  with the passage of the front. The azimuthal magnetic field of the flux tube changes discontinuously with the passage of the front according to Ampere's law, so that the propagating Alfvénic fronts effect an 'unwinding' of the flux tube. Note that these simplifying assumptions about the current density imply that the flux tube is not a force-free structure (see § 2.4).

Behind the fronts, a radial electric field is established by the time rate of change of  $B_\phi$ . This electric field causes a bulk rotation  $v_\phi$  of the plasma behind the front according to  $\mathbf{E} = -\mathbf{v} \times \mathbf{B}$ . Fronts propagate outwards in both directions ( $z > 0$  and  $z < 0$ ) from the resistive region, and the established (radial) electric field is odd in  $z$ , i.e.  $E_r(-z) = -E_r(z)$ . Consequently, the plasma in the flux tube counter-rotates either side of  $z = 0$ . Slippage of field lines continuously occurs at the resistive region; elsewhere the field lines are frozen-in to the plasma. This slippage represents a form of generalised magnetic reconnection according to the definition of Hesse and Schindler (1988a; 1988b; Schindler *et al.* 1991; Hesse, 1991), although the geometry of the process is not that of the familiar X-type neutral point model (Sonnerup *et al.* 1990).

At the propagating fronts, energy stored in the azimuthal component of the magnetic field of the loop is partially converted into a Poynting flux (to supply the resistive region) and partially into the bulk rotation of the plasma within the tube. Equating the power in the Poynting flux to that dissipated at  $z = 0$  gives

$$\frac{J_1}{J_0} = \frac{R_{A1}}{R_{A1} + R_c}, \quad (2.1)$$

where  $R_{A1} = \mu_0 v_{A1}$  is the Alfvénic impedance of the flux tube, with  $v_{A1} = B_0/(\mu_0 \rho_1)^{1/2}$  the coronal Alfvén speed, where  $\rho_1$  is the coronal density. Equation (2.1) implies that the power dissipated in the central resistive region is given by

$$P_{\text{diss}} = R_c I_1^2 = \left( \frac{R_{A1}}{R_{A1} + R_c} \right)^2 R_c I_0^2, \quad (2.2)$$

where  $I_i = \pi r_0^2 J_i$  is the total current inside radius  $r_0$  ahead of ( $i = 0$ ) and behind ( $i = 1$ ) the advancing front. This expression shows that a maximum initial power release occurs when  $R_c = R_{A1}$ , the case of *impedance matching*.

When the Alfvénic fronts reach the photosphere ( $z = l/2$ ), they are partially reflected and partially transmitted. A uniform Alfvén speed is assumed above the photosphere, so that the propagation time to the photosphere is  $\tau_A = l/2v_{A1}$ . This assumption means that we are dealing with a simplified model of wave propagation in the solar atmosphere; a more sophisticated model would require an accurate description of the decrease in Alfvén speed through the corona and chromosphere, where reflection of the front may occur. In this model, reflection occurs at a step in density attributed to the photosphere, although it may be thought of as representing the transition region (separating the corona and chromosphere), where a steep increase in density occurs (e.g. Lang, 1992). Melrose considered two boundary conditions at  $z = l/2$ . In the first, the subphotosphere is treated as a resistive region through which the front cannot propagate. This boundary condition is often applied to Alfvén waves incident on the ionosphere of the earth from the magnetosphere, since the ionosphere is a thin layer bounded below by the neutral atmosphere, in which Alfvén waves cannot propagate (e.g. Scholer, 1970; Goertz and Boswell, 1979). The relevance of this boundary condition in the solar context is investigated in chapter 4 of this thesis. The second, more realistic boundary condition (which is adopted here) treats the subphotosphere as a uniform region with a lower Alfvén speed  $v_{A2}$ . Assuming the second boundary condition, Melrose showed that the current in the flux tube evolves with repeated reflections of the Alfvénic fronts according to the pair of difference equations

$$J_{2n+2} - J_{2n+1} = \alpha_{12}(\alpha_{12}\alpha_c)^n(J_0 - J_1), \quad (2.3)$$

and

$$J_{2n+1} - J_{2n} = -(\alpha_{12}\alpha_c)^n(J_0 - J_1), \quad (2.4)$$

where  $\alpha_{12}$  and  $\alpha_c$  are the reflection coefficients at the photosphere and the central resistive region respectively, viz.,

$$\alpha_{12} = \frac{R_{A2} - R_{A1}}{R_{A2} + R_{A1}}, \quad (2.5)$$

and

$$\alpha_c = \frac{R_c - R_{A1}}{R_c + R_{A1}}. \quad (2.6)$$

The impedances  $R_{Ai} = \mu_0 v_{Ai}$  describe the coronal ( $i = 1$ ) and subphotospheric ( $i = 2$ ) plasma. The solution of Equations (2.3) and (2.4) after many reflections is

$$\frac{I_\infty}{I_0} = \frac{R_{12}}{R_{12} + R_c}. \quad (2.7)$$

Equation (2.7) is also the result predicted by a simple circuit theory analogy.

### 2.1.2 Towards a more realistic treatment

Most of this chapter is concerned with the relaxation of some of the restrictive assumptions in the existing model. The chapter is divided as follows. In §2.2 the model is generalised to describe the evolution of the system after the period of flare energy release ends. In §2.3, the model is generalised to describe a gradual, rather than an impulsive turning-on and -off of energy release. §2.4 discusses the necessary description of the flux tube as a force-free magnetic structure. In §2.5, the flare mechanism of Zaitsev and Stepanov (1991; 1992) — which claims to account for the appearance of  $R_c$  in the existing model — is critically examined. Finally, the results of the various changes are discussed in §2.6.

## 2.2 The impulsive turning-off of energy release

To model an impulsive end to solar flare energy release, the resistive region  $R_c$  is assumed to turn off after the  $2m$ th reflection of an Alfvénic front from the photospheric boundary and the resistive region. That is, at a time  $t_{2m} = 2m\tau_A$  when a front carrying a current density  $J_{2m}$  behind it returns to the origin. As in the original model, the current densities behind fronts are assumed purely axial and uniform in  $r$  for simplicity, and the boundary condition at the photosphere is modelled as a discontinuous jump in Alfvén speed from  $v_{A1}$  down to  $v_{A2}$ , due to increasing density.

In the following, we also assume that the turning-off of  $R_c$  occurs before the Alfvénic fronts generated by  $R_c$  have time to propagate around the complete (subphotospheric) current circuit. This is consistent with the argument that current closure occurs deepbelow the photosphere, perhaps at the base of the convection zone (see chapter 4).

The turning-on and -off of  $R_c$ , like the dissipation itself, is not explicitly addressed in terms of microphysics. A simple picture is that the new current density  $J_{2m}$  has reached a critical value below which the resistive processes can no longer be sustained. This would be appropriate if for instance  $R_c$  was the result of anomalous resistivity, or double layers, as discussed above.

The sudden turning-off of  $R_c$  launches Alfvénic fronts to communicate the

change at the origin. Behind these fronts a current density  $\bar{J}_1$  is established. (All current densities after the turning-off of  $R_c$  are denoted with a bar;  $J_{2m}$  is taken to be equivalent to  $\bar{J}_0$ .) The simple geometry of the original model implies that the radial electric field  $E_r$  within the flux tube is odd in  $z$  and so continuity of  $E_r$  in the plane  $z = 0$  implies zero electric field behind the new fronts. Consequently the plasma is at rest behind the outgoing fronts. This is consistent with the reasoning that there can no longer be slippage of field lines in the plane  $z = 0$  in the absence of a resistive disk; ideal magnetohydrodynamics is restored when  $R_c = 0$ .

Considering the system after  $k$  more reflections have occurred, the current density behind the propagating front inside  $0 \leq z \leq l/2$  is  $\bar{J}_{k+1}$ . Applying the boundary condition of continuity of Poynting flux at  $z = 0$  and  $z = l/2$  behind and ahead of fronts establishes the difference equations describing the evolution of  $\bar{J}_i$ :

$$\bar{J}_{2k+1} - \bar{J}_{2k} = (-\alpha_{12})^k (\bar{J}_1 - \bar{J}_0) \quad (2.8)$$

and

$$\bar{J}_{2k+2} - \bar{J}_{2k+1} = (-\alpha_{12})^{k+1} (\bar{J}_1 - \bar{J}_0), \quad (2.9)$$

where

$$\bar{J}_1 - \bar{J}_0 = \frac{R_{A2}}{R_{A1}} (J_0 - J_{2m}). \quad (2.10)$$

Equations (2.8)–(2.10) are derived in the Appendix to this chapter (§ 2.7.1). Comparing Equations (2.8) and (2.9) with Equations (2.3) and (2.4) — the corresponding equations describing fronts generated after  $R_c$  first turns on — clearly the former may be derived from the latter with the formal substitution  $\alpha_c = -1$ . This corresponds to  $R_c = 0$  as might be expected.

Equations (2.8)–(2.10) may be solved to give

$$\bar{J}_{2k} = J_{2m} + [1 - (-\alpha_{12})^k] (J_0 - J_{2m}). \quad (2.11)$$

The asymptotic value of current implied by Equation (2.11) is

$$\bar{J}_\infty = J_0, \quad (2.12)$$

that is, the current returns to its initial state after infinitely many reflections. Equation (2.12) also follows from the requirement that the steady state of the system is that predicted by a simple circuit model (cf. Equation (2.7)).

Equation (2.12) proves that the flux tube as a whole returns to its initial state, allowing the possibility of later flaring activity associated with the same flux tube. This provides an explanation, in the context of this model for *homologous* flares, the name assigned to flares that recur in almost identical form in a particular part of an active region (Švestka, 1976). The occurrence of homologous flares suggests that flaring activity does not catastrophically disrupt the magnetic topology of the flare site, and that energy resupply to the corona takes place after the flare ends. The model developed here meets both these requirements. In particular, the energy stored in the magnetic field of the flux tube above the corona increases after the flare energy release turns off. This occurs because energy is being continually supplied as a Poynting flux from the subphotosphere. Magnetic energy is being released from the subphotospheric portion of the flux tube by the unwinding of the field at fronts propagating downwards.

### 2.2.1 Timescales for energy release and resupply

The timescales for energy release and resupply to the corona in this model may be estimated from the series describing the current density, as follows. If the resistance  $R_c$  turns off after many Alfvén transit times, then a time of interest is that for the current density to fall a fraction  $f$  of the way to its asymptotic value. Using Equations (2.3) and (2.4), this is given by

$$t_{f_{\text{down}}} = \frac{\ln(1-f)}{\ln(\alpha_{12}\alpha_c)}\tau_A, \quad (2.13)$$

where both logarithmic terms involve fractional arguments and so are negative. Similarly, the time for the current to return to a fraction  $f$  of its asymptotic value after  $R_c$  has impulsively switched off follows from Equation (2.11);

$$t_{f_{\text{up}}} = \frac{\ln(1-f)}{\ln(-\alpha_{12})}\tau_A. \quad (2.14)$$

For significant change, say  $f = \frac{1}{2}$ ,  $\ln(1-f) = -\ln 2$ , which is of order  $-1$ . The  $\ln(1-f)$  factors are replaced by  $-1$  in the semiquantitative estimates to follow. The important ratios in the times given by Equations (2.13) and (2.14) are

$$x \equiv \frac{R_{A2}}{R_{A1}}, \quad y \equiv \frac{R_c}{R_{A1}}. \quad (2.15)$$

Clearly  $x \ll 1$  but the value of  $y$  is not determined independently in the model. However, maximum power release corresponds to  $y = 1$ , the case of impedance



matching, and for a large flare it is expected that the system is driven hard and so impedance matching may be approached (Melrose, 1992).

Two limiting cases are of relevance here. In the first,  $R_c$  does not turn off until the current density has almost reached its asymptotic value, i.e. after many reflections. This corresponds to  $y \ll 1$ . Then the characteristic times for winding up and down are given by Equations (2.13) and (2.14) in the limit of small  $x$  and  $y$ ;

$$t_{\text{down}} \approx \frac{\tau_A}{x + y}, \quad t_{\text{up}} \approx \frac{\tau_A}{x}. \quad (2.16)$$

In this limit the times for relaxation and re-stressing are comparable.

The second limit applies when the system is driven hard, so that there is impedance matching and  $R_c$  turns off in about one Alfvén transit time, i.e.  $t_{\text{down}} \approx \tau_A$  (so Equation (2.13) is not appropriate). The characteristic time for the current density to rise is again given by Equation (2.16),  $t_{\text{up}} \approx \tau_A/x$ . This shows that when the system is driven hard, it returns to its original state in a characteristic time  $1/x = R_{A1}/R_{A2}$  longer than the energy release time. With  $R_{A1}/R_{A2} = v_{A1}/v_{A2} \approx 10^2$ , a release time of a few minutes implies resupply occurs over several hours, qualitatively consistent with the timescales observed in homologous flares (Švestka, 1976; Sturrock, 1980). Melrose (1992) arrived at this same conclusion by a qualitative argument based on the Poynting flux arriving from below the photosphere before  $R_c$  turns off. Here, the result has been rigorously derived by considering the evolution of the system after  $R_c$  turns off.

### 2.3 The gradual turning-on of energy release

In practice the turning-on (and -off) of  $R_c$  cannot occur abruptly, and the dissipative region cannot appear instantly across the flux tube cross section. A simple argument suggests that the time-dependent behaviour of the dissipative region also involves a continuous propagation transverse to field lines, as follows. When dissipation is established in any localised region in the flux tube, current is deflected around the region by the process of propagation of Alfvénic fronts along field lines, as described above. If the onset of the dissipation is caused by a current instability triggered when the current density locally exceeds some critical value, then the deflection of current is likely to increase the current density above that critical value in the plasma surrounding the dissipative region, and dissipation is triggered there too. Haerendel suggested such a cross-field growth of a region

of enhanced resistivity in his ‘fracture model’ of stressed magnetospheric field lines (Haerendel, 1980; 1983; 1987; 1988; 1990; 1994). In Haerendel’s model the dissipation propagates transversely with a speed determined by the dimension of the region in which magnetic energy is stored and the return time of propagating fronts deflecting the current. In the context of the model presented here, the process continues until the dissipative region is established across the diameter of the current-carrying flux tube.

To avoid the complication of the necessary transverse growth of  $R_c$ , consider a narrow flux tube, so that changes in resistivity can be considered to propagate instantly across the width of the tube. In this simple picture, a single value  $R_c(t)$  can be assigned as the resistance in the plane  $z = 0$  and inside the flux tube, just as in the impulsive case. Since the dissipation turns on at  $t = 0$ , we can take  $R_c(0) = 0$ . The discussion here is limited to the gradual turning-on of  $R_c$ , with some consideration of the implications for the corresponding gradual turning-off. We also limit the discussion to the properties of the flux tube for times less than the Alfvén propagation time to the photosphere.

If the current density through the origin at time  $t$  is  $J(t)$  then we require  $J(t) = J_0$  for all  $t < 0$  and so a suitable form for  $J(t)$  is

$$J(t) = J_0 + [j(t) - J_0] \theta(t), \quad (2.17)$$

where  $\theta(t)$  is the step function. This current profile rigidly propagates away from the origin with the Alfvén speed for times less than the propagation time to the photosphere, i.e. for  $0 < t < \tau_A$ . The current density can be thought of as changing behind a continuous sequence of Alfvénic fronts, in contrast to the impulsive case, where the passage of fronts is discrete. So for  $0 < t < \tau_A$ , the current in the flux tube is

$$J(z, t) = J(t'), \quad t' = t - z/v_{A1}. \quad (2.18)$$

The magnetic field associated with this current is

$$B_\phi(r, t') = \frac{1}{2} \mu_0 r J(t'), \quad (2.19)$$

and using the  $\phi$ -component of the Faraday-Maxwell equation assuming  $E_z = 0$ , i.e.  $\partial E_r / \partial z = -\partial B_\phi / \partial t$ , we obtain the corresponding radial electric field

$$E_r(r, t') = -\frac{1}{2} \mu_0 v_{A1} r [J_0 - j(t')] \theta(t'). \quad (2.20)$$

The azimuthal bulk flow corresponding to this electric field is

$$v_\phi(r, t') = -E_r(r, t')/B_0 = \Omega(t')r, \quad (2.21)$$

where the angular velocity of the motion is  $\Omega(t') = (\mu_0/\rho_1)^{\frac{1}{2}} [J_0 - j(t')]$ .

Now consider the energetics of the relaxation of the flux tube. The quantities of interest are the power in the release of magnetic energy in the flux tube  $P_{\text{mag}}(t)$ , the Poynting flux  $P_S(z, t)$  and the power associated with the kinetic energy going into bulk rotation of the plasma in the flux tube,  $P_{\text{kin}}(t)$  (cf. Melrose, 1992). These may be calculated as follows.

The  $z$ -component of the Poynting vector is  $S_z(r, t') = E_r(r, t')B_\phi(r, t')/\mu_0$  and integrating this over the flux tube cross section gives

$$P_S(z, t) = \frac{1}{4}\pi\mu_0v_{A1}r_0^4j(t')[J_0 - j(t')] \theta(t'). \quad (2.22)$$

In particular, the power arriving at the origin at time  $t$  ( $t > 0$ ) is

$$P_S(0, t) = \frac{1}{4}\pi\mu_0v_{A1}r_0^4j(t)[J_0 - j(t)]. \quad (2.23)$$

Equation (2.23) may be equated with the power dissipated at the origin at time  $t$ , viz.

$$P_{\text{diss}}(t) = [\pi r_0^2 j(t)]^2 R_c(t), \quad (2.24)$$

to give

$$\frac{j(t)}{J_0} = \frac{R_A}{R_A + R_c(t)}. \quad (2.25)$$

Equation (2.25) is analogous to the impulsive case, cf. Equation (2.1).

Next consider the total magnetic energy in the flux tube of length  $l$ , which is given by

$$E_{\text{mag}}(t) = \frac{2\pi}{\mu_0} \int_0^{r_0} r dr \int_0^{l/2} dz [B_\phi(r, z, t)^2 + B_0^2]. \quad (2.26)$$

The power released in the flux tube as the tube unwinds is given by  $P_{\text{mag}}(t) = -dE_{\text{mag}}(t)/dt$ , which may be evaluated to give

$$P_{\text{mag}}(t) = \frac{1}{8}\pi\mu_0v_{A1}r_0^4 [J_0^2 - j(t)^2]. \quad (2.27)$$

The power going into kinetic energy of rotation is calculated in a similar fashion. The total kinetic energy in the flux tube is given by

$$E_{\text{kin}}(t) = 2\pi \int_0^{r_0} r dr \int_0^{l/2} dz \rho v_\phi(r, z, t)^2 \quad (2.28)$$

and so the power going into rotation is  $P_{\text{kin}}(t) = dE_{\text{kin}}(t)/dt$  which may be evaluated to give

$$P_{\text{kin}}(t) = \frac{1}{8}\pi\mu_0 v_{A1} r_0^4 [J_0 - j(t)]^2. \quad (2.29)$$

Equations (2.23), (2.27) and (2.29) are completely analogous to the impulsive case, with the replacements  $R_c \rightarrow R_c(t)$  and  $J_1 \rightarrow j(t)$ . Conservation of energy is satisfied (as required by the Poynting theorem) on inspection since

$$P_S(0, t) + P_{\text{kin}}(t) = P_{\text{mag}}(t). \quad (2.30)$$

The power dissipated in the resistive region is given by

$$P_{\text{diss}} = \left[ \frac{R_{A1}}{R_{A1} + R_c(t)} \right]^2 R_c(t) I_0^2, \quad (2.31)$$

which is analogous to the impulsive case and establishes that the maximum rate of energy release occurs for  $R_c(t) = R_{A1}$ , i.e. the case of (instantaneous) impedance matching. It is reasonable to speculate that in a large flare, the resistance  $R_c(t)$  increases rapidly from zero to the impedance matched value  $R_{A1}$ .

The results above demonstrate a straightforward generalisation of the existing model to the case of a gradual turning-on of  $R_c$ , in which all essential features of the model are maintained. The corresponding case of a gradual end to energy release (cf. § 2.2) is expected to be just as straightforward.

## 2.4 Towards a force-free model

Coronal magnetic flux tubes are generally modelled as static structures subject to negligible pressure and gravity forces. With these assumptions the hydrostatic equation for the flux tube becomes the *force-free* equation  $\mathbf{J} \times \mathbf{B} = 0$ , where  $\mathbf{J}$  is the current density in the tube and  $\mathbf{B}$  is the magnetic field. This equation implies that the current density is aligned with the magnetic field, and is usually written

$$\text{curl } \mathbf{B} = \alpha \mathbf{B}, \quad (2.32)$$

where  $\alpha$  is in general some function of position. The model for energy propagation in a solar flare presented above (Melrose, 1992) is not force-free, and we consider here the changes necessary to make it so.

Force-free fields are difficult to describe analytically, because Equation (2.32) is intractable for general  $\alpha$ . The problem is simpler for the case of cylindrically

symmetric fields  $\mathbf{B} = [0, B_\phi(\varpi), B_z(\varpi)]$  (where  $\varpi$  denotes the radial co-ordinate) because then all solutions to Equation (2.32) can be characterised in a straightforward way. The hydrostatic balance equation  $\mathbf{J} \times \mathbf{B} = 0$  for a cylindrically symmetric flux tube is

$$\frac{d}{d\varpi} \left( \frac{B_\phi^2 + B_z^2}{2\mu_0} \right) + \frac{B_\phi^2}{\mu_0\varpi} = 0, \quad (2.33)$$

which is satisfied by fields described by the *generating function*  $f(\varpi)$ , where

$$B_\phi^2 + B_z^2 = f(\varpi), \quad (2.34)$$

and

$$B_\phi^2 = -\frac{1}{2}\varpi \frac{df}{d\varpi}. \quad (2.35)$$

Consider an Alfvénic front propagating down a cylindrically symmetric, force free flux tube, carrying behind it a new current density. The appropriate boundary condition to relate the fields behind and ahead of the front is continuity of the normal component of magnetic field across the front. If the field behind the front is also cylindrically symmetric then this boundary condition is equivalent to continuity of the axial component of magnetic field across the front. If the field behind the front is also force free, then Equations (2.34) and (2.35) imply that the generating function ahead of the front ( $f$ ) is related to that behind the front ( $f'$ ) by

$$f + \frac{1}{2}\varpi \frac{df}{d\varpi} = f' + \frac{1}{2}\varpi \frac{df'}{d\varpi}, \quad (2.36)$$

or

$$\frac{d}{d\varpi} \left[ \varpi^2 (f - f') \right] = 0. \quad (2.37)$$

The solution to Equation (2.37) is  $f' = f + C/\varpi^2$ , where  $C$  is a constant. Although the  $C/\varpi^2$  term is not itself unphysical (a line current is implied) clearly only restrictive changes in fields (and hence currents) are possible if the passage of the front is to maintain a force-free, cylindrically symmetric flux tube. For example, for the constant  $\alpha$  ('linear force-free') case,  $C = 0$ , implying that a front cannot propagate and change the current whilst maintaining the symmetry and force-free conditions.

This reasoning suggests that as the front propagates into the force-free flux tube, the fields and current densities behind the front are not immediately force-free. They relax to the force-free state dynamically, with the appropriate dynamic timescale (the Alfvén speed). At some distance behind the Alfvénic front the

flux tube is force-free. One approach to the problem is then to consider how two force-free, cylindrically symmetric sections of a flux tube may be matched, via an intermediate, non force-free and non cylindrically symmetric section. Parker (1979) has considered a related problem, namely the connection of two cylindrically symmetric sections of a static flux tube by an intermediate non cylindrically symmetric section, where the axial variation of the tube is brought about by a static, prescribed variation in external fluid pressure. The treatment here borrows some aspects of Parker's (1979) approach.

Consider a field line in the cylindrically symmetric section ahead of the front at radius  $\varpi$  which after the passage of the front and relaxation to a force-free, cylindrically symmetric state is at radius  $\Pi$ . The problem is then, given the 'initial' generating function  $f(\varpi)$  to determine  $\Pi = \Pi(\varpi)$  and the 'final' generating function  $F(\Pi)$ . Figure 2.1 illustrates the problem. Following Parker (1979), one relation between the initial and final fields is provided by conservation of axial flux between  $\varpi$  and  $\varpi + d\varpi$  and  $\Pi$  and  $\Pi + d\Pi$ ;

$$B_z(\Pi) \Pi d\Pi = b_z(\varpi) \varpi d\varpi, \quad (2.38)$$

where the lower case and capital quantities refer to the fields ahead of and behind the front respectively. Parker's second condition — allowing elimination of  $F(\Pi)$  and hence solution for  $\Pi(\varpi)$  — comes from the azimuthal component of the Maxwell stress. The idea is that for equilibrium of the two sections of the flux tube at different pressure, no rings of flux should be allowed to slide between sections. Here, however, this is no longer appropriate since we are considering a time-dependent process. Instead, some simplifying assumptions are needed about the form of the fields and currents.

Consider first the case of a uniform axial density current ahead of the front;

$$j_z = \begin{cases} j_0 & \text{if } \varpi \leq \varpi_0 \\ 0 & \text{if } \varpi > \varpi_0. \end{cases} \quad (2.39)$$

Then the appropriate cylindrically symmetric force-free solution ahead of the front is described (for  $\varpi < \varpi_0$ ) by the generating function

$$f(\varpi) = b_0^2 - \frac{1}{4} \mu_0^2 \varpi^2 j_0^2, \quad (2.40)$$

where  $b_0$  is the value of the axial field along  $\varpi = 0$ . (The force-free field for  $\varpi > \varpi_0$  is trivial because the current density is assumed to be zero there.)

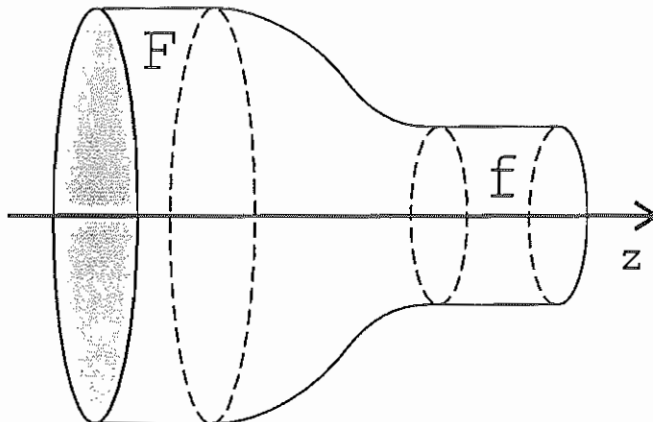


Figure 2.1: A simple model for the expansion of the force-free flux tube due to the propagation of an Alfvénic front. A cylindrically symmetric force-free section ahead of the front (with generating function  $f = f(\varpi)$ ) is assumed to be matched, via a non force-free, non cylindrically symmetric section of tube to a second force-free, cylindrically symmetric section behind the front (with generating function  $F = F(\Pi)$ ). The surface in the diagram is the surface on which one group of magnetic field lines lies.

First we present a simple argument suggesting that the flux tube expands in response to a propagating front carrying a lower current density with it. For simplicity, we assume that a uniform current density  $j_1$  is set up immediately behind the front, owing to the deflection of current in the front. We denote the magnetic field ahead of the front  $\mathbf{b} = (0, b_\phi, b_z)$ , corresponding to the generating function (2.40), and the corresponding current density is  $\mathbf{j} = (0, j_\phi, j_z)$ , where  $j_z = j_0$ . We denote the field immediately behind the front  $\mathbf{b}' = (b'_\varpi, b'_\phi, b'_z)$ , with corresponding current density  $\mathbf{j}' = (j'_\varpi, j'_\phi, j'_z)$ , where  $j'_z = j_1$ . Continuity of the normal component of magnetic field at the front (assumed transverse) implies that  $b'_z = b_z$ . By Ampere's law  $b'_\phi = \mu_0 \varpi j_1 / 2$ , and

$$j'_\phi = \frac{1}{\mu_0} \left( \frac{\partial b'_\varpi}{\partial z} - \frac{\partial b'_z}{\partial \varpi} \right). \quad (2.41)$$

Using these expressions for the magnetic field and current just behind the front and the generating function (2.40), the radial force on the plasma just behind the front is

$$(\mathbf{j}' \times \mathbf{b}')_\varpi = j'_\phi b'_z - j'_z b'_\phi \approx \frac{1}{2} \mu_0 \varpi (j_0^2 - j_1^2), \quad (2.42)$$

where I neglect a term involving  $\partial b'_\varpi / \partial z$ . Appeal to  $\text{div } \mathbf{b}' = 0$  suggests that this term is small. Equation (2.42) implies that the flux tube expands in response to

the passage of a front that deflects current density to the surface of the flux tube.

The expansion of the flux tube may be described by the following simple model. Assume that the current density in the force-free region behind the front has the uniform value  $J_f$ . This region is a circularly symmetric, force-free section of the flux tube and so is described by the generating function

$$F(\Pi) = B_0^2 - \frac{1}{4}\mu_0^2\Pi^2 J_f^2, \quad (2.43)$$

where  $B_0$  is the central axial field value. Then applying conservation of axial flux — i.e. Equation (2.38) — between the initial and final sections,

$$\Pi(B_0^2 - \frac{1}{2}\mu_0^2\Pi^2 J_f^2)^{\frac{1}{2}} d\Pi = \varpi(b_0^2 - \frac{1}{2}\mu_0^2\varpi^2 j_0^2)^{\frac{1}{2}} d\varpi. \quad (2.44)$$

This equation is integrable and gives the result

$$\frac{\Pi}{\varpi} = \left(\frac{j_0}{J_f}\right)^{\frac{1}{3}}, \quad (2.45)$$

where  $\Pi(\varpi = 0) = 0$  is assumed. Equation (2.45) shows that the expansion of the flux tube is linear under the present assumptions. The initial and final total currents,  $I_0$  and  $I_f$  respectively, are related by the particularly simple expression

$$\frac{I_0}{I_f} = \frac{\Pi_0}{\varpi_0}, \quad (2.46)$$

where  $\Pi(\varpi_0) = \Pi_0$  is also assumed.

The treatment presented in this section is valid within the context of the overall model. However, the dynamics of that model are somewhat uncertain. In the original model for energy propagation in a solar flare (Melrose, 1992) the propagation of the Alfvénic front was introduced only as a simplified description of the dynamics of the response of the flux tube to  $R_c$  turning on. A more sophisticated treatment must derive the details of the propagation of an Alfvénic front from the equations of motion of the plasma and Maxwell's equations (cf. Goertz and Boswell, 1979). An abrupt change of current density at a propagating front is equivalent to saying that the azimuthal component of the magnetic field, or the bulk azimuthal velocity, satisfies the wave equation with the relevant speed the Alfvén speed. In the existing model, only the azimuthal component of the momentum equation is satisfied. This simplified description becomes suspect when applied to detailed questions of the dynamics of the flux tube. Nevertheless, this section establishes that changing the existing model to describe the relaxation



of a stressed, force-free flux tube is a non-trivial exercise. In particular, a simple model is presented above that suggests that when magnetic free energy is released from the flux tube it expands radially.

## 2.5 Zaitsev and Stepanov: accounting for $R_c$ ?

As discussed in § 2.1, Zaitsev and Stepanov (1991; 1992; hereafter ZS) addressed the central problem in solar flare theory seen from a circuit viewpoint<sup>1</sup>: the need for a flare loop resistance of order  $R_c = 10^{-4}$ – $10^{-3}\Omega$  to account for the observed power release, whereas a classical estimate of the resistance of a coronal loop gives a value  $\approx 10^{-11}\Omega$ . ZS presented a mechanism by which the resistance of the flaring loop is increased by eight to ten orders of magnitude over the classical value. Their argument is reproduced briefly here, followed by a specific criticism of the mechanism.

ZS considered that the increase in coronal resistance of a flaring loop is a result of the non-steady state, partially ionised conditions set up when a filament overlying the loop intrudes into the loop via the flute instability, introducing neutral plasma. Figure 2.2 illustrates this process. The intrusion of the filament provides the trigger for the flare.

ZS derived a generalised Ohm's law relevant to non-steady, partially ionised conditions, from the three-fluid equations of motion. The form found (in which terms of order  $(m_e/m_i)^{\frac{1}{2}}$  are ignored) is

$$\mathbf{E}' = \frac{m_e(\nu_{ei} + \nu_{en})}{e^2 n} \mathbf{J} + \frac{1}{en} \mathbf{J} \times \mathbf{B} - \frac{F}{nm_i \nu_{in}} \nabla p_n \times \mathbf{B} - \frac{1}{en} \nabla p_e - \frac{\rho F^2}{nm_i \nu_{in}} \frac{d\mathbf{V}}{dt} \times \mathbf{B}, \quad (2.47)$$

where  $\mathbf{V}$  is the mean plasma velocity,  $\mathbf{E}' = \mathbf{E} + \mathbf{V} \times \mathbf{B}$  is the electric field in the moving frame,  $F = n_n m_n / \rho$  is the relative density of neutrals and the other symbols have their usual meaning. Note that SI units are adopted here, whereas ZS used Gaussian units. Gravity terms are neglected. A similar Ohm's law is discussed by Cowling (1976). Note that, if Equation (2.47) is to revert to the familiar, completely ionised time-dependent Ohm's law in the limit  $n_n \rightarrow 0$ , an additional term  $(m_e/ne^2) d\mathbf{J}/dt$  is required on the right-hand side.

<sup>1</sup>See § 1.3 of chapter 1.

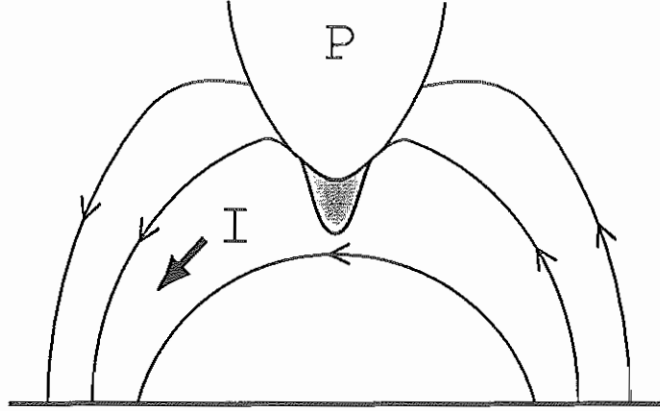


Figure 2.2: A schematic diagram of Zaitsev and Stepanov's (1991; 1992) 'prominence-loading' model to account for the increase in resistance of a flaring coronal loop. A prominence, P, overlying a current-carrying loop, intrudes into the loop via a plasma instability and introduces dense, neutral material (the shaded region) as well as non-steady state conditions. The arrowed curves represent field lines; their twist is not represented.

ZS applied Equation (2.47) as follows. Consider a cylindrical current channel, of cross section  $S$  and length  $d$ . In this region prior to the intrusion of the filament material, the  $\mathbf{J} \times \mathbf{B}$  force density must be balanced by the gradient of the gas pressure. When the flute instability develops, the neutral material introduced into the loop is assumed to smooth out the original pressure distribution, leaving a non equilibrium state described by  $\rho d\mathbf{V}/dt = \mathbf{J} \times \mathbf{B}$ . Using this expression in the final term of Equation (2.47), the density of power dissipated in the volume of interest is

$$q = \mathbf{E}' \cdot \mathbf{J} = \frac{m_e(\nu_{ei} + \nu_{en})}{e^2 n} J^2 - \frac{F}{nm_i \nu_{in}} \nabla p_n \times \mathbf{B} \cdot \mathbf{J} - \frac{1}{en} \nabla p_e \cdot \mathbf{J} + \frac{F^2}{nm_i \nu_{in}} (\mathbf{J} \times \mathbf{B})^2. \quad (2.48)$$

By integrating  $q$  over the cylindrical volume of the current channel, ZS arrived at the total power dissipated,  $\dot{W}$ . ZS argued that the cylindrical geometry considered implies  $\nabla p_e \cdot \mathbf{J} = 0$  (so the third term on the right-hand side of Equation (2.48) makes no contribution) and that the  $\nabla p_n \times \mathbf{B} \cdot \mathbf{J}$  term is of smaller magnitude than the first and last terms on the right-hand side of Equation (2.48), and so may also be neglected. ZS additionally assumed a purely axial current  $I$ , with a constant current density  $\mathbf{J}$ . The only magnetic field included in the

calculation is the azimuthal field  $B_\phi$  produced by this  $\mathbf{J}$ . Then a straightforward calculation gives  $\dot{W} = RI^2$ , where

$$R = R_l + R_{nl}, \quad (2.49)$$

with

$$R_l = \frac{m_e(\nu_{ei} + \nu_{en})d}{2\pi e^2 n S}, \quad (2.50)$$

and

$$R_{nl} = \frac{\mu_0^2 F^2 I^2 d}{8\pi n m_i \nu_{in} S^2}. \quad (2.51)$$

Equation (2.50) is the usual Ohmic dissipation; Equation (2.51) is an additional resistance due to collisions between ions and neutrals under non-steady state conditions. The subscripts ‘ $l$ ’ and ‘ $nl$ ’ refer to the linear and non-linear dependences, respectively, on the appropriate collision frequencies.

The evaluation of  $R$  quoted in ZS may be reproduced as follows. The solar parameters used by ZS are  $n_\Sigma = n_n + n = 10^{18} \text{ m}^{-3}$ ,  $T = 10^7 \text{ K}$ ,  $d = 5 \times 10^6 \text{ m}$ ,  $S = 10^{12} \text{ m}^2$ ,  $F = 0.1$ , and  $I = 3 \times 10^{11} \text{ A}$ . Note that, assuming  $m_i \approx m_n$  and neglecting  $m_e$  with respect to  $m_i$ , the number density of neutrals is given by  $n_n \approx nF/(1 - F)$ . Only the collision frequencies are then needed to estimate  $R_l$  and  $R_{nl}$ . Using the standard form  $\nu_{\alpha n} = n_n \sigma (k_B T / m_\alpha)^{\frac{1}{2}}$  where  $\sigma$  is the effective collision cross section (e.g. Krall and Trivelpiece, 1973) allows the estimates  $R_l = 4 \times 10^{-13} (\sigma / 10^{-20} \text{ m}^2) \Omega$  and  $R_{nl} = 7 \times 10^{-4} (10^{-20} \text{ m}^2 / \sigma) \Omega$ . These values are comparable with ZS and reproduce the eight to ten order of magnitude increase in  $R$  that they claimed. Following ZS, we then find  $R_{nl} I^2 \approx 10^{20} \text{ W}$ , which is of order the power associated with small flares.

ZS’s calculation — as reproduced above — produces a serious overestimate of the resistance of the loop for the following reason. ZS stated that before the filament intrudes into the loop, the loop is in equilibrium, with the Ampere force density,  $\mathbf{J} \times \mathbf{B}$ , balanced by the gradient of gas pressure. However, for the perpendicular current density and magnetic field geometry they assumed in the derivation of Equation (2.49), this could not be the case. For their geometry,  $|\mathbf{J} \times \mathbf{B}| = JB_\phi \leq (I/S)\mu_0 I / [2\pi(S/\pi)^{\frac{1}{2}}] \approx 3 \times 10^{-2} \text{ Nm}^{-3}$  is very much greater than any relevant pressure force. For example, a plausible estimate of the pressure force density is  $|\nabla p| \approx nk_B T / (S/\pi)^{\frac{1}{2}} \approx 2 \times 10^{-4} \text{ Nm}^{-3}$ , implying  $|\nabla p| \ll |\mathbf{J} \times \mathbf{B}|$  for most of the cylinder of interest. The geometry of  $\mathbf{J}$  and  $\mathbf{B}$  assumed by ZS is the underlying problem: the current density and magnetic field in the corona are

not perpendicular (as ZS assumed) but are close to parallel (i.e. force-free), with the departure from parallel defined by a residual pressure gradient,  $|\mathbf{J} \times \mathbf{B}| = |\nabla p| \approx nk_B T / (S/\pi)^{\frac{1}{2}}$ . Following ZS's own argument, after the filament material intrudes into the loop, the pressure gradient is smoothed out and the  $\mathbf{J} \times \mathbf{B}$  force density is unbalanced. Its magnitude must still be of order  $nk_B T / (S/\pi)^{\frac{1}{2}}$ , however, which provides a more self consistent estimate of the contribution of the final term in Equation (2.48) to the resistance of the flaring loop:

$$\begin{aligned} R_{nl} &= \frac{F^2}{nm_i \nu_{in} I^2} \int |\mathbf{J} \times \mathbf{B}|^2 dV \approx \frac{F^2 S d}{nm_i \nu_{in} I^2} \left[ \frac{nk_B T}{(S/\pi)^{\frac{1}{2}}} \right]^2 \\ &\approx 6 \times 10^{-8} (10^{-20} \text{ m}^2 / \sigma) \Omega. \end{aligned} \quad (2.52)$$

This (revised) estimate is about four orders of magnitude smaller than ZS's value. Whilst  $R_{nl}$  provides a considerable increase over  $R_l$ , the increase is not enough to account for the energy release in even the most modest flares. There are many other possible criticisms of ZS's approach. Their mechanism predicts, for example that energy release should occur more powerfully at the chromospheric level (where the cross-sectional area of the tube,  $S$ , is smaller), but there is no observational support for this. The criticism detailed here is enough, however, to show that the mechanism of ZS does not produce the spectacular (eight to ten orders of magnitude) increase in the resistance of a coronal loop claimed.

## 2.6 Conclusions

This chapter presents several refinements of an existing model for energy propagation into the primary site of energy release in a solar flare. The existing model (Melrose, 1992) describes the relaxation of a stressed magnetic flux tube when a dissipative region turns on at its midpoint. The dissipative region is a simple model for the flare energy release site.

In § 2.2 the model is generalised to describe the evolution of the system after the flare energy release turns off. It is shown that energy is resupplied to the corona after an impulsive end to the flare, from the subphotospheric portions of the flux tube. The system finally returns to its original (pre-flare) state. This process may provide a simple explanation of the phenomenon of homologous flares, where repeated flaring activity is observed in the same site in an active region. For a flare to re-occur in a given region, the magnetic and current topology

of the region must be re-established. This implies energy resupply to the coronal magnetic fields, as demonstrated by the present model. The timescale for energy resupply in this model is much greater than that for release if the system is driven hard in the release phase (a reasonable assumption for energetic flares), consistent with the observed delay between homologous flares.

In § 2.3, the model is generalised to describe a gradual, rather than an impulsive turning-on and -off of energy release. The model retains its principal features, with time variations in the resistance of the dissipative region communicated to the flux tube by a continuous sequence of Alfvénic fronts. In particular, the maximum rate of energy release occurs when the resistance of the dissipative region instantaneously matches the Alfvénic impedance of the coronal portion of the flux tube.

§ 2.4 discusses the necessary description of the flux tube as a force-free magnetic structure. The model presented is incomplete, but it introduces the new result that the relaxation of the stressed, force-free coronal magnetic flux tube involves the radial expansion of the tube.

Finally, § 2.5 presents a critical examination of Zaitsev and Stepanov's (1991; 1992) model to account for the dramatically increased resistance of a flaring coronal loop. In Zaitsev and Stepanov's model, a filament overlying a current-carrying loop was assumed to intrude into the loop via an instability, introducing dense neutral material and non-steady state conditions near the loop apex. The Ohm's law relevant to these conditions predicts an increase in resistance over the classical, Spitzer resistivity. It is shown, however, that the eight to ten orders of magnitude increase estimated by Zaitsev and Stepanov is based on the incorrect assumption of non force-free conditions in the loop before the introduction of the filament plasma. Consequently, the model is not a satisfactory flare mechanism.

## 2.7 APPENDIX

### 2.7.1 Derivation of Equations (2.8)—(2.10)

First, define  $t_k \equiv k\tau_A$ , the time of the  $k^{\text{th}}$  reflection of a front, recalling that  $R_c$  turned on at  $t = 0$ . We assume that  $R_c$  switches off at  $t = t_{2m}$ , when the front with current density  $J_{2m}$  behind it passes through the origin. A front is launched to communicate the impulsive end of energy release, carrying behind it a new current  $\bar{J}_1$ , where for simplicity we assume  $\bar{J}_0 = J_{2m}$ .

Consider the system just after time  $t = t_{2(n+m)}$ . A front leaves the origin, with a current density  $\bar{J}_{2n+1}$  behind it and current density  $\bar{J}_{2n}$  ahead. The electric field in the region  $0 < z < l/2$  may be written (cf. Melrose, 1992)

$$E_r = -\frac{1}{2}\mu_0 v_{A1} r \left\{ \bar{j}_{2n+1} + (\bar{j}_{2n} - \bar{j}_{2n+1}) \theta \left[ z - v_{A1}(t - t_{2(n+m)}) \right] \right\}. \quad (2.53)$$

As stated above, the radial electric field in this model is an odd function of  $z$ . This follows because the current density and hence  $B_\phi$  are even functions of  $z$  (by symmetry), and so, from  $\partial E_r / \partial z = -\partial B_\phi / \partial t$ ,  $E_r$  is odd in  $z$ . The radial electric field must be continuous at the origin, and requiring  $E_r$  as defined by Equation (2.53) to be odd about the origin and continuous there implies

$$\bar{j}_{2n+1} = 0. \quad (2.54)$$

The electric field may also be written in terms of the current densities, as

$$E_r = -\frac{1}{2}\mu_0 v_{A1} r (\bar{J}_{2n} - \bar{J}_{2n+1}) \theta \left[ z - v_{A1}(t - t_{2(n+m)}) \right], \quad (2.55)$$

and comparing Equations (2.53) and (2.55) and using Equation (2.54),

$$\bar{j}_{2n} = \bar{J}_{2n+1} - \bar{J}_{2n}. \quad (2.56)$$

Next, consider the flux tube just after time  $t = t_{2(m+n)+1}$ , as fronts depart  $z = l/2$ . A front propagates into the region  $z > l/2$ , carrying behind it a current density  $\bar{J}_{2n+2}$  and ahead of it the current density is  $\bar{J}_{2n}$ . A front propagates in the negative  $z$  direction away from  $z = l/2$  as well, with a current density  $\bar{J}_{2n+2}$  behind it and a current density  $\bar{J}_{2n+1}$  ahead. The radial electric fields in  $0 < z < l/2$  (denoted ‘-’) and in  $z > l/2$  (denoted ‘+’) may be written

$$E_r^- = -\frac{1}{2}\mu_0 v_{A1} r \left\{ \bar{j}_{2n+1} + (\bar{j}_{2n+2} - \bar{j}_{2n+1}) \theta \left[ z - v_{A1}(t - t_{2(n+m)+1}) \right] \right\}, \quad (2.57)$$

and

$$E_r^+ = -\frac{1}{2}\mu_0 v_{A2} r \left\{ \bar{k}_{2n+2} + (\bar{k}_{2n} - \bar{k}_{2n+2}) \theta \left[ z - v_{A2}(t - t_{2(n+m)+1}) \right] \right\}. \quad (2.58)$$

Following the procedure to obtain Equation (2.56), comparing Equations (2.57) and (2.58) with the electric field calculated from the current densities and using Equation (2.54),

$$\bar{j}_{2n+2} = \bar{J}_{2n+2} - \bar{J}_{2n+1}, \quad (2.59)$$

and

$$\bar{k}_{2n} - \bar{k}_{2n+2} = \bar{J}_{2n+2} - \bar{J}_{2n}. \quad (2.60)$$

Also, requiring  $E_r$  to be continuous at  $z = l/2$  behind the fronts gives that

$$R_{A1} \bar{j}_{2n+2} = R_{A2} \bar{k}_{2n+2}. \quad (2.61)$$

For consistency in the definitions of the  $\bar{k}_i$  it is necessary that

$$\bar{k}_0 = J_0 - J_{2m}. \quad (2.62)$$

Equation (2.10) may be obtained from Equation (2.61) when  $n = -1$ , together with Equations (2.62) and (2.56) when  $n = 0$ :

$$\bar{J}_1 - \bar{J}_0 = \frac{R_{A2}}{R_{A1}} (J_0 - J_{2m}). \quad (2.63)$$

Next we derive Equations (2.8) and (2.9). Equation (2.61) implies that

$$R_{A1} (\bar{j}_{2n+2} - \bar{j}_{2n}) = R_{A2} (\bar{k}_{2n+2} - \bar{k}_{2n}), \quad (2.64)$$

which can be rewritten by noting that Equation (2.56) and (2.59) imply

$$\bar{j}_{2n+2} - \bar{j}_{2n} = \bar{J}_{2n+2} - 2\bar{J}_{2n+1} + \bar{J}_{2n}, \quad (2.65)$$

as

$$R_{A1} (\bar{J}_{2n+2} - 2\bar{J}_{2n+1} + \bar{J}_{2n}) = R_{A2} (\bar{J}_{2n} - \bar{J}_{2n+2}), \quad (2.66)$$

where Equation (2.60) is also used. After some manipulation, Equation (2.66) may be recast as

$$\bar{J}_{2n+2} - \bar{J}_{2n+1} = \alpha_{12} (\bar{J}_{2n} - \bar{J}_{2n+1}), \quad (2.67)$$

which describes the boundary condition on current changes at  $z = l/2$ . The corresponding condition at  $z = 0$  may be obtained by combining Equations (2.56) and (2.59) to give

$$\bar{J}_{2n+2} - \bar{J}_{2n+3} = \bar{J}_{2n+1} - \bar{J}_{2n+2}. \quad (2.68)$$

Together, Equations (2.67) and (2.68) give

$$\bar{J}_{2n+1} - \bar{J}_{2n} = -\alpha_{12} (\bar{J}_{2n-1} - \bar{J}_{2n-2}). \quad (2.69)$$

Applying Equation (2.69)  $n$  times gives Equation (2.8), viz.

$$\bar{J}_{2n+1} - \bar{J}_{2n} = (-\alpha_{12})^n (\bar{J}_1 - \bar{J}_0). \quad (2.70)$$

Equations (2.67) and (2.70) give Equation (2.9).



## Chapter 3

# Interpreting Yohkoh hard and soft X-ray flare observations

**Abstract:** A simple model is presented to account for the Yohkoh flare observations of Feldman *et al.* (1994), and Masuda (1994). Electrons accelerated by the flare are assumed to encounter the dense, small regions observed by Feldman *et al.* at the tops of impulsively flaring coronal magnetic loops. The values of electron density and volume inferred by Feldman *et al.* imply that these dense regions present an intermediate thick-thin target to the energised electrons. Specifically, they present a thick (thin) target to electrons with energy much less (greater) than  $E_c$  where  $15 \text{ keV} < E_c < 40 \text{ keV}$ . The electrons are either stopped at the loop-top or precipitate down the field lines of the loop to the footpoints. Collisional losses of the electrons at the loop-top produce the heating observed by Feldman *et al.* and also some hard X-rays. It is argued that this is the mechanism for the loop-top hard X-ray sources observed in limb flares by Masuda. Adopting a simple model for the energy losses of electrons traversing the dense region and the ambient loop plasma, hard X-ray spectra are derived for the loop-top source, the footpoint sources and the region between the loop-top and footpoints. These spectra are compared with the observations of Masuda. The model spectra are found to agree qualitatively with the data, and in particular account for the observed steepening of the loop-top and footpoint spectra between 14 and 53 keV and the relative brightnesses of the loop-top and footpoint sources.

### 3.1 Introduction

Recent observations by the Yohkoh spacecraft have provided new insight into the vexed question of the physical processes behind solar flare hard and soft X-ray emission. For the first time the distribution of hard X-ray emission with height in the solar atmosphere has been unambiguously determined by well resolved observations of limb flares (Masuda, 1994). In this chapter we are concerned with explaining some of the plasma physics of two specific sets of observations: those of Masuda and those of Feldman *et al.* (1994). By way of introduction, a summary is given of the main results of those observations.

Feldman *et al.* considered 38 impulsive X-ray flares observed with the high resolution Yohkoh Soft X-ray Telescope (SXT). Typically, the emitting regions were found to be tiny pointlike sources (smaller than one SXT pixel, so  $V \leq 3 \times 10^{18} \text{ m}^3$ ), surrounded by fainter extended emission. The diffuse emission defined a loop structure, with the pointlike emission at the top of the loop. The electron temperature for the point source was derived spectrally; for all flares observed, the peak temperatures were uniformly close to  $2 \times 10^7 \text{ K}$ . Feldman *et al.* argued that conduction cooling would be too slow to account for the observed decay in temperature of the bright features during the cooling phase. Also, the continued appearance of the sources as pointlike during the cooling is inconsistent with conductive cooling along field lines. Assuming radiation cooling dominates, the cooling times observed imply a lower limit to the number density of electrons of order  $10^{18} \text{ m}^{-3}$ . An upper limit of  $n_e = 10^{20} \text{ m}^{-3}$  was derived by Feldman *et al.* from line intensity ratios. Adopting the average emission measure  $n_e^2 V = 3 \times 10^{54} \text{ m}^{-3}$  at peak intensity, these limits on density imply the corresponding range for the emitting volume  $3 \times 10^{14} \text{ m}^3 < V < 3 \times 10^{18} \text{ m}^3$ .

The values for electron number density derived by Feldman *et al.* are large compared with typical coronal ('quiet Sun') values, e.g.  $n_e \approx 10^{14} \text{ m}^{-3}$  (Brown and McClymont, 1975). This observation provided the initial motivation for the model presented below.

The observations of Feldman *et al.* are at variance with the predictions of the 'chromospheric evaporation' model of the heating of the flare soft X-ray emitting plasma (Acton *et al.* 1992). In the evaporation scenario, the hot, dense coronal flare plasma is supposed to be chromospheric material, evaporated from the foot-points of coronal loops by flare energy incident from above (Doschek *et al.* 1990).

The hot plasma should gradually rise up to fill the loop during the flare. These observations and others establish that the loop-tops contain a region of dense, hot, soft X-ray emitting plasma early in the flare, implying that pre-existing, coronal plasma is heated *in situ* (Feldman, 1990). Any acceptable model of flare hard and soft X-ray emission must account for such *in situ* heating. Melrose and Dulk (1984), for example, developed a model for the *in situ* heating of the coronal soft X-ray emitting plasma through absorption of radio frequency emission produced by energetic electrons trapped in a flaring coronal loop.

Masuda (1994) presented simultaneous, coaligned hard and soft X-ray images, taken with the Yohkoh Hard X-ray Telescope (HXT) and the SXT, for two impulsive limb flares. These showed that, in addition to two footpoint hard X-ray sources, a hard X-ray source was located (in both cases) at or above the apex of the loop outlined in soft X-ray. Figure 3.1 shows one of the images, for the flare which occurred on January 13, 1992. A further analysis of ten limb flares observed with the HXT showed three distinct types of hard X-ray sources associated with flares: footpoint sources (8 events/10), gradual loop-top sources (10/10) and impulsive loop-top sources (6/10). Masuda presented some estimates of the spectral indices of the footpoint and loop-top sources, based on the count ratios between adjacent energy bands of the HXT (see § 3.4).

Masuda interpreted the presence of the loop-top hard X-ray source in the context of a theoretical model for flare energy release (e.g. Forbes and Malherbe, 1986). The mechanism of the energy release was considered to be magnetic reconnection, proceeding in a region some distance above the coronal loop of interest. The hypothesised reconnection outflow impinges on the loop, creating a shocked region just above the loop. The loop-top source observed by Masuda may be evidence for the presence of a shocked region, possibly where electrons are accelerated. In this paper we assume only that accelerated electrons are introduced by some mechanism at the loop-top, and account for the loop-top hard X-ray source observed by Masuda in terms of the interaction of the electrons with the ambient plasma.

The sections of this chapter are divided as follows. In § 3.2 a physical mechanism is outlined for the production of Masuda's loop-top and footpoint hard X-ray sources, as well as the loop-top soft X-ray sources described by Feldman *et al.* This is the basis in § 3.3 for a detailed theoretical model of the photon spectra of the observed hard X-ray sources. In particular, the spectral indices of the

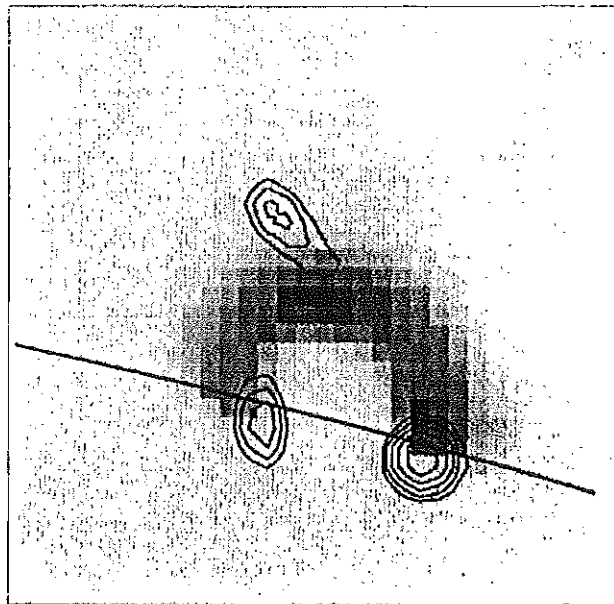


Figure 3.1: The coaligned hard and soft X-ray images obtained by Masuda (1994) for the Jan 13 flare observed at the limb of the sun (the solid line). The greyscale is the soft X-ray, and the contours represent hard X-ray emission in the 33-53 keV range. (From Kosugi, 1994.)

model loop-top and footpoint sources are determined and an expression for their relative brightness derived. In §3.4 these model spectral indices and predictions about relative brightness are compared with Masuda's data. In §3.5 the energy going into heating the model loop-top source is written down and compared with the spectral observations of temperature obtained by Feldman *et al.* §3.6 contains a discussion of possible directions for improvement of the model, which is a prelude to future work. Finally, the main results of the model are summarised in §3.7.

## 3.2 Accounting for a loop-top source

The bulk of the impulsive energy release in a solar flare goes into accelerating  $> 10$  keV electrons. These electrons precipitate from near the apex of a coronal magnetic loop in both directions along field lines to the chromosphere. In the denser layers of the solar atmosphere the electrons encounter a thick target (Brown, 1971) and are stopped, producing the hard X-ray footpoint sources observed by Masuda (1994) and a wealth of secondary flare emission.

We assume that the accelerated electrons are introduced by some means at the centre of the dense loop-top regions observed by Feldman *et al.* (1994) in soft X-rays. All the electrons then traverse, on average, half the dense region in escaping along field lines into the thinner, ambient coronal plasma.

In escaping the dense region at the top of the flaring coronal loop, the accelerated electrons traverse an intermediate thick-thin target. A given column depth of material is a thin target to a non-thermal distribution of electrons if that electron distribution remains unchanged in traversing the target. A thick target is a column depth of material sufficient to stop all the non-thermal electrons. The dense loop-top region considered here has a column depth such that it stops low energy electrons in the injected electron flux spectrum, but does not stop high energy electrons in the spectrum. This may be demonstrated as follows. The mean free path for an electron of energy  $E$  is  $\lambda(E) = E^2/n_e K$ , with  $K = 2\pi r_0^2(m_e c^2)^2 \ln \Lambda$ , where  $r_0$  is the classical radius of the electron and  $\ln \Lambda$  is the Coulomb logarithm. For a given column depth,  $N_0 = n_e l$ , the transition between thick and thin target occurs at an energy  $E_c$  defined by  $l = \lambda(E_c)/2$ , giving  $E_c = (2KN_0)^{1/2}$ . The values of Feldman *et al.* for  $n_e$  and  $V$  (quoted above) imply a range of column densities  $10^{24} \text{ m}^{-2} < n_e V^{1/3} < 7 \times 10^{24} \text{ m}^{-2}$ . The lower value of column density corresponds

to a larger, less dense source ( $V = 3 \times 10^{14} \text{ m}^3$ ,  $n_e = 10^{18} \text{ m}^{-3}$ ). If accelerated electrons are introduced at the centre of the dense region, and they encounter half this column density on their outward path, this implies  $15 \text{ keV} < E_c < 40 \text{ keV}$ . Here the values of  $\ln \Lambda$  appropriate for a hydrogen plasma with  $T_e = 10^7 \text{ K}$  and the number density quoted above are used in each case (Spitzer, 1962), namely  $\ln \Lambda = 16$  ( $n_e = 10^{20} \text{ m}^{-3}$ ) and  $\ln \Lambda = 18$  ( $n_e = 10^{18} \text{ m}^{-3}$ ). The range of non-thermal electron energies of relevance to solar flares is 10–100 keV. Consequently, a significant fraction of electrons in the accelerated electron population have energy  $E < E_e$  and so are likely to be stopped at the top of the loop. This process may provide the heating of the loop-top source necessary to make it visible in soft X-ray (Feldman *et al.*) and also produces some hard X-rays. It is argued here that this is the mechanism responsible for the loop-top hard X-ray sources observed in limb flares by Masuda. The loop-top soft X-ray source is produced by the heating of pre-existing dense coronal material, and so avoids the weakness of the chromospheric evaporation model discussed above.

### 3.3 A detailed model for the spectra of the loop-top and footpoint sources

A power law electron flux spectrum  $F_0(E) = AE^{-\delta}$  (electrons per unit time and per unit energy  $E$ ) is assumed to be injected by the flare energy release mechanism in the centre of a dense cylindrical region of column depth  $2N_0$  located at the apex of a coronal loop. This simple geometry implies that all electrons encounter the column depth  $N_0$  in escaping into the ambient coronal loop plasma.

#### 3.3.1 Evolution of the electron flux spectrum

To describe the X-ray spectrum of an intermediate thick-thin target accurately, it is necessary to describe how the electron distribution changes in traversing the target (Leach and Petrosian, 1981; 1983). This is in contrast to the thick- or thin-target limits, where only the injected electron flux spectrum needs to be specified (Brown, 1971). The treatment here follows Brown and McClymont (1975). For simplicity it is assumed that the electrons experience no change in average pitch angle as they traverse the dense region. Then the flux spectrum at column depth

$N$  has the analytic form

$$F(E, N) = \frac{EF_0 (\sqrt{E^2 + 2KN})}{\sqrt{E^2 + 2KN}}, \quad (3.1)$$

cf. Brown and McClymont (1975), and Leach and Petrosian (1981). Note that it is assumed that the electron propagation time to the footpoints is much shorter than the time scale for variation of  $F_0$ , so that the electron distribution in the flaring loop may be treated as static.

### 3.3.2 The photon spectrum from the loop-top

Following Brown and McClymont (1975), we adopt the non-relativistic, direction-integrated Bethe-Heitler cross-section for the production of bremsstrahlung photons in collisions of energised electrons with ambient particles. The spectrum (photons per unit time, per unit energy  $\varepsilon$  and per unit area at the Earth) of the loop-top source is then that of a source of column depth  $N_0$  in which the electron flux spectrum is given by Equation (3.1). This may be written

$$I_{\text{lt}}(\varepsilon) = I_{\text{th}}(\varepsilon) - I'(\varepsilon), \quad (3.2)$$

where  $I_{\text{th}}(\varepsilon)$  is the thick-target spectrum

$$I_{\text{th}}(\varepsilon) = \frac{A\kappa_{\text{BH}}\bar{Z}^2}{4\pi R^2 K} \frac{B(\delta - 2, \frac{1}{2})}{(\delta - 2)(\delta - 1)} \varepsilon^{-(\delta-1)}, \quad (3.3)$$

with  $\kappa_{\text{BH}} = \frac{8}{3}\alpha r_0^2 m_e c^2$ , and where  $\alpha$  is the fine structure constant,  $B(p, q)$  is the Beta function (Abramowitz and Stegun, 1965),  $R = 1 \text{ AU}$  and  $\bar{Z} \approx 1.4$  is an average atomic number for the solar atmosphere. The second term on the right of Equation (3.2) represents the departure from thick-target behaviour and is given by

$$I'(\varepsilon) = \frac{A\kappa_{\text{BH}}\bar{Z}^2}{4\pi R^2 K} \frac{\varepsilon^{-(\delta-1)}}{\delta - 1} G(E_c/\varepsilon, \delta), \quad (3.4)$$

with

$$G(\beta, \delta) = \int_0^1 x^{\delta-3} (1 + \beta^2 x^2)^{-\frac{1}{2}(\delta-1)} f(x) dx, \quad (3.5)$$

and with  $E_c = (2KN_0)^{\frac{1}{2}}$ ,  $f(x) = \ln[(1 + \sqrt{1-x})/(1 - \sqrt{1-x})]$ . Equations (3.2)–(3.5) are derived in the Appendix to this chapter (§3.8.1).

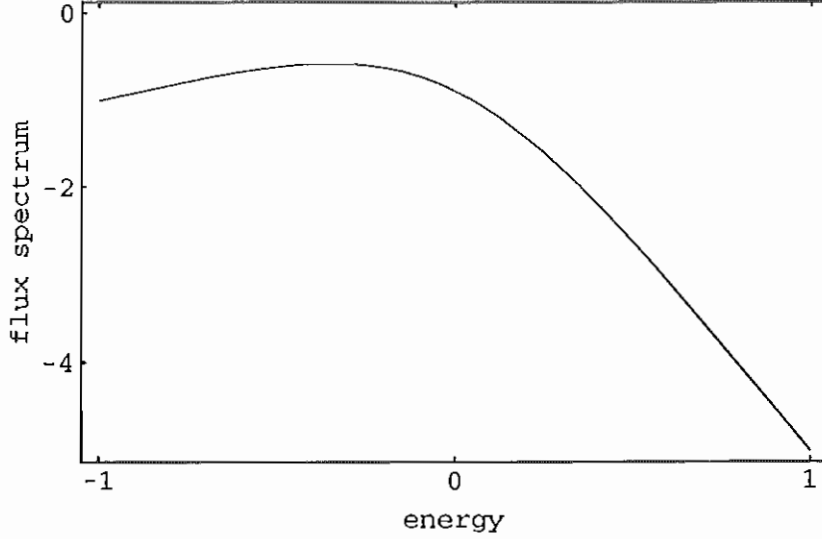


Figure 3.2: The electron flux injection spectrum  $F = F(E, N_0)$  for the footpoint source for the case  $\delta = 5$ . The graph shows  $\log(F/AE_c^{-\delta})$  as a function of  $\log(E/E_c)$ . The spectrum is depleted below  $E_c = (2KN_0)^{\frac{1}{2}}$ . For  $E \ll E_c$ ,  $F \sim E$  and for  $E \gg E_c$ ,  $F \sim E^{-\delta}$ .

### 3.3.3 The photon spectrum from the footpoints

Ignoring changes in  $F(E, N)$  in propagating from the loop-top to the footpoints, the footpoint source can be considered to be a thick target where the injection flux spectrum is  $F(E, N_0)$ , defined by Equation (3.1). This injection spectrum (illustrated in Figure 3.2) is depleted of low energy electrons, which see the loop-top dense region as a thick target.

It then follows that the spectrum of the footpoint source is  $I_{\text{fp}}(\varepsilon) = I'(\varepsilon)$ , defined by Equation (3.4). This may be obtained by the usual thick-target formulae with  $F_0(E) = F(E, N_0)$  (e.g. Brown, 1975), or simply by recognising that, if unresolved, the sum of the loop-top and footpoint spectra must be the thick-target spectrum Equation (3.3). Hence Equation (3.2) must hold with  $I'(\varepsilon) = I_{\text{fp}}(\varepsilon)$ .

### 3.3.4 The photon spectrum from between the loop-top and footpoints

If the electron flux spectrum is unchanged in propagating from the loop-top to the footpoints, then the electrons must encounter a thin target between these two regions. A spectrum  $I_a(\varepsilon)$  may be calculated for bremsstrahlung from electrons



stopped in the ambient coronal loop plasma by using the thin target formulae (e.g. Brown, 1975) with the electron flux spectrum  $F(E, N_0)$  and assigning a column depth  $N_a$  to the region. We find

$$I_a(\varepsilon) = \frac{A\kappa_{\text{BH}}\bar{Z}^2}{4\pi R^2} N_a \varepsilon^{-(\delta+1)} G'(E_c/\varepsilon, \delta), \quad (3.6)$$

with

$$G'(\beta, \delta) = \int_0^1 x^{\delta-1} (1 + \beta^2 x^2)^{-\frac{1}{2}(\delta+1)} f(x) dx. \quad (3.7)$$

Equations (3.6) and (3.7) are derived in the Appendix to this chapter (§3.8.2).

### 3.3.5 Behaviour of model spectra

Figure 3.3 shows the qualitative behaviour of the spectra  $I_{\text{lt}}$  and  $I_{\text{fp}}$ . The most important prediction of this model is clear from the figure, namely that both spectra show a break in (photon) spectral index  $\gamma$  about  $\varepsilon = E_c = (2KN_0)^{\frac{1}{2}}$ , but the sum of the two spectra does not show a break in spectral index.  $I_{\text{lt}} + I_{\text{fp}}$  is the spectrum of a thick target and so consists of a single power law (with index  $\delta - 1$ ). Equation (3.6) implies that the spectrum of the portion of the flux tube between the loop-top and footpoints also exhibits a break in spectral index about  $\varepsilon = E_c$ .

The breaks in index of the model spectra may be understood as follows. Consider first the behaviour of the spectra  $I_{\text{lt}}$ ,  $I_{\text{fp}}$  and  $I_a$  at high energies, i.e. when  $\varepsilon \gg E_c$ . At high energies the loop-top source has the spectral index  $\delta + 1$  — the spectral index of a thin target (Brown, 1975) — because high energy electrons (responsible for the high energy photons) see the loop-top region as a thin target. The footpoint source at high energies approaches a power law with index  $\delta - 1$ , because the injected spectrum at high energies is undepleted and these electrons meet a thick target at the footpoint. Finally, for high energies  $I_a$  becomes a power law with index  $\delta + 1$ , because it is a thin target to an undepleted electron spectrum. Next consider the behaviour of the model spectra at low energies, i.e. when  $\varepsilon \ll E_c$ . At low energies, the spectral index of the loop-top is  $\delta - 1$ , because low energy electrons (which produce most of the low energy photons) see the loop-top region as a thick target. The spectra  $I_{\text{fp}}$  and  $I_a$  are not power laws at low energy, because they are produced by a depleted electron flux spectrum.

The other important property of the spectra  $I_{\text{lt}}$  and  $I_{\text{fp}}$ , as seen in Figure 3.3 is that  $I_{\text{lt}}$  dominates over  $I_{\text{fp}}$  for  $\varepsilon \ll E_c$ , whilst  $I_{\text{fp}}$  dominates for  $\varepsilon \gg E_c$ . At  $\varepsilon = E_c$

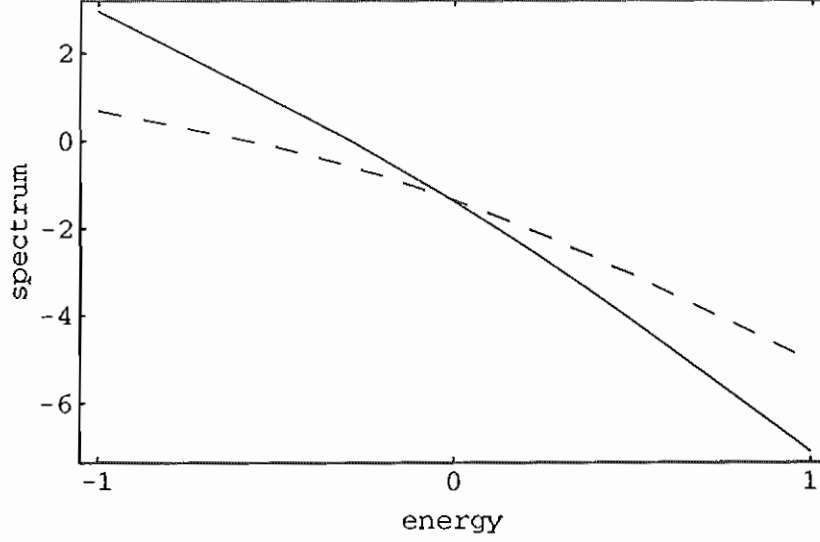


Figure 3.3: The scaled photon spectra  $\log(I_{\text{lt}}/I')$  (solid) and  $\log(I_{\text{fp}}/I')$  (dashed) plotted as a function of  $\log(\varepsilon/E_c)$ , where  $I' = 4\pi R^2 K / (A\kappa_{\text{BH}} \bar{Z}^2)$ . The loop-top source approaches spectral indices  $\delta - 1$  and  $\delta + 1$  for  $\varepsilon \ll E_c$  and  $\varepsilon \gg E_c$  respectively. The footpoint source is not a power law for  $\varepsilon \ll E_c$  but is for  $\varepsilon \gg E_c$ , when it approaches the thick-target index  $\delta - 1$ .

they are equal in magnitude. This may be understood as follows. Low energy photons are most likely to be produced by the stopping of low energy electrons, which see the loop-top region as a thick target. Consequently the loop-top is brightest at low photon energies. High energy photons must be produced by high energy electrons, which see the loop-top as a thin target and so are likely to reach the footpoints. Consequently the footpoints dominate the photon spectrum at high energies. The equivalence of the magnitude of the two spectra at  $\varepsilon = E_c$  provides an observational determination of  $E_c$  according to the model.

### 3.3.6 Ratio of count rates

To compare the predictions of the model spectra with Masuda's data, a relevant quantity is the ratio of count rates between the footpoint source and the loop-top source above a cut-off energy  $\varepsilon_0$ :

$$r(\varepsilon > \varepsilon_0) = \int_{\varepsilon_0}^{\infty} I_{\text{fp}}(\varepsilon) d\varepsilon / \int_{\varepsilon_0}^{\infty} I_{\text{lt}}(\varepsilon) d\varepsilon. \quad (3.8)$$

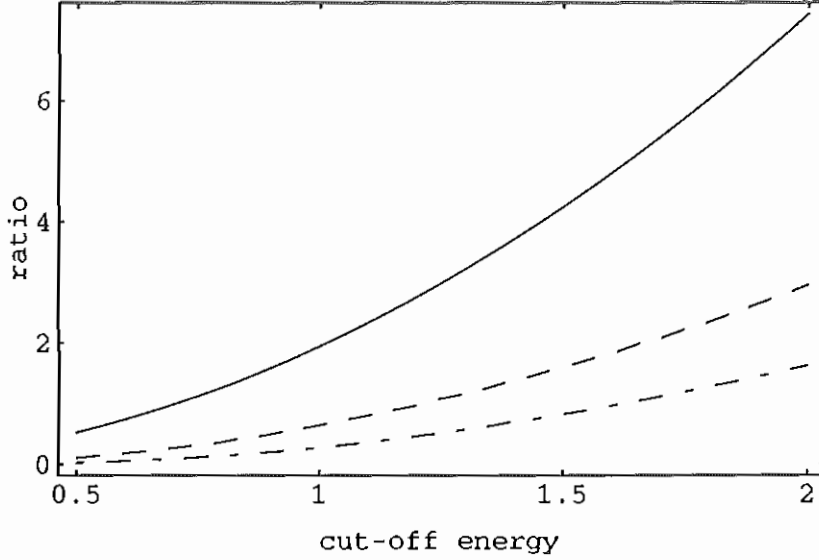


Figure 3.4: The ratio  $r(\varepsilon > \varepsilon_0)$  of counts per second at the footpoints to the loop-top above a cut-off energy  $\varepsilon_0$  plotted as a function of  $\varepsilon_0/E_c$ . The solid curve is for the case  $\delta = 5$ , the dashed curve is  $\delta = 7$  and the dot-dashed curve is  $\delta = 9$ .

We find

$$r(\varepsilon > \varepsilon_0) = \left[ \frac{B(\delta - 2, \frac{1}{2})}{(\delta - 2)\Gamma(\delta/2)J(\varepsilon_0/E_c, \delta)} - 1 \right]^{-1}, \quad (3.9)$$

with

$$J(u, \delta) = (2u)^{\frac{1}{2}(\delta-2)} \int_0^1 x^{\frac{1}{2}(\delta-4)} [1 + (x/u)^2]^{-\frac{1}{4}(\delta-2)} \times P_{\frac{1}{2}(\delta-4)}^{-\frac{1}{2}(\delta-2)} \{ [1 + (x/u)^2]^{-\frac{1}{2}} \} f(x) dx, \quad (3.10)$$

where  $P_\nu^\mu(x)$  is the associated Legendre function of the first kind (Abramowitz and Stegun, 1965). Plots are shown in Figure 3.4 of  $r(\varepsilon > \varepsilon_0)$  as a function of  $\varepsilon_0/E_c$  over an appropriate range. The function  $r(\varepsilon > \varepsilon_0)$  is a monotonically increasing function of  $\varepsilon_0/E_c$ . This is because the footpoint source is brighter at higher energies. Also,  $r(\varepsilon > \varepsilon_0)$  decreases with  $\delta$ . This is because steeper injection spectra imply more lower energy electrons, which are likely to be stopped at the loop-top, hence increasing the relative brightness of the loop-top source.

### 3.3.7 A modified model

Before a detailed comparison of the predictions of the model and Masuda's observations (Masuda, 1994) is presented, a simple change to the model needs to

be discussed. It is possible that only a fraction  $f$  of the electrons injected at the loop-top encounter the dense region, whilst a fraction  $1 - f$  avoid the dense region, encountering only the ambient coronal density. The consequences of this change are straightforward to outline. The loop-top source is an intermediate thick-thin target produced by an injection flux spectrum  $fF_0(E)$ , and the footpoint sources are thick targets with injection spectrum  $fF(E, N_0) + (1 - f)F_0(E)$ , assuming again that the electrons are stopped according to Equation (3.1). The loop-top spectrum is then  $I_{lt} = f(I_{th} - I')$ , where  $I_{th}$  and  $I'$  are given by Equations (3.3) and (3.4). The footpoint source may be obtained by the argument that the sum of the loop-top and footpoint spectra must be a thick-target spectrum for the injected flux  $F_0(E)$ . Consequently, one has  $I_{fp} = (1 - f)I_{th} + fI'$ . This modified model introduces the following changes. The loop-top source has an identical spectrum to that of the original model, but is reduced in brightness by the factor  $f$ . The footpoint source has a more complicated behaviour, but may be understood qualitatively as follows. If all the electrons encounter the loop-top dense region ( $f = 1$ ), the model is identical to the original model. If all the electrons miss the loop-top dense region ( $f = 0$ ), the loop-top source vanishes and the footpoint spectrum is that of a thick target, i.e. a power law with index  $\delta - 1$ . Consequently, for arbitrary  $f$  the spectrum is intermediate between these cases, exhibiting less of a break in index at  $\varepsilon = E_c$  than the extreme case  $f = 1$ , but agreeing at large  $\varepsilon$  with either of the extreme cases. Except where indicated below, the observations of Masuda (1994) and Feldman *et al.* (1994) are compared with the original ( $f = 1$ ) model.

## 3.4 Comparison with Masuda's observations

### 3.4.1 Masuda's spectral indices

Masuda's (1994) individual spectral indices for loop-top and footpoint sources for ten limb flares are reproduced in Table 3.1. The quoted values are approximate, derived from count rates in adjacent energy bands under the assumption that a single power law holds over both bands. Specifically, spectral indices  $\gamma$  were inferred from the ratio of count rates of the L (14–23 keV) and M1 (23–33 keV) bands (here denoted  $\gamma(M1/L)$ ) and the M1 and M2 (33–53 keV) bands ( $\gamma(M2/M1)$ ). No detailed spectra are possible with the Yohkoh instruments.

Date	$\gamma_{lt}(M1/L)$	$\gamma_{lt}(M2/M1)$	$\gamma_{fp}(M1/L)$	$\gamma_{fp}(M2/M1)$
91/12/02	5.5	5.5	3.2	6.3
91/12/15	-	-	3.5	3.9
92/01/13	2.6	4.1	$\leq 2.0$	4.0
92/02/06	6.8	$\geq 9.0$	-	-
92/02/17	5.4	$\geq 9.0$	2.7	6.7
92/04/01	-	-	3.2	3.7
92/10/04	$\leq 2.0$	5.2	2.3	3.4
92/11/05	-	-	3.9	6.5
92/11/23	5.5	6.3	3.8	4.6
93/02/17	3.6	6.1	4.1	6.0

Table 3.1: The spectral indices  $\gamma(M1/L)$  and  $\gamma(M2/M1)$  (see text) derived by Masuda (1994) for the footpoint (fp) and loop-top (lt) sources in the ten limb flares observed. A dash indicates that one source was not observed for that flare.

Spectral indices derived from count rates in such broad adjacent energy bands are subject to considerable uncertainty. Consequently, care must be taken in the comparison of the spectral predictions of the model presented above and Masuda's data. Despite these caveats, our simple model qualitatively agrees with many aspects of Masuda's data.

Masuda observed localised footpoint and loop-top sources in the higher energy bands (M1, M2) and a more diffuse X-ray emission, following the soft X-ray loop, at lower energy (L). This qualitatively agrees with our model. The thin-target emission described by  $I_a$  is seen only at lower energies because higher energy electrons (responsible for high energy photons) are less likely to be stopped between loop-top and footpoints. Masuda's loop-top and footpoint spectral indices are based on a procedure of drawing a box around each source and counting photons within the box for each energy band. This approach neglects the diffuse emission from the loop at lower energies. Consequently it is not possible to compare in detail the spectrum  $I_a$  predicted by Equation (3.6) and observation. In the remainder of this section we compare the model spectra  $I_{lt}$  and  $I_{fp}$  with Masuda's observations.

### 3.4.2 The break in spectral index

One striking aspect of Masuda's data is the break in spectral index, i.e. the difference between  $\gamma(M1/L)$  and  $\gamma(M2/M1)$ . Steepening of (unresolved) flare impulsive hard X-ray spectra at high energies is a familiar observational fact (Brown, 1971) but occurs generally in the 60–100 keV range (and sometimes as high as 500 keV), significantly higher than the steepening inferred by Masuda for the individual, resolved loop-top and footpoint spectra. The change in  $\gamma$  in the unresolved case is generally less than two and is attributed to a fundamental change in the injected electron distribution at these energies. These comments refer to the early impulsive phase of hard X-ray emission. More detailed spectral behaviour is observed in the later stages of the flare (e.g. Lin *et al.* 1981).

The model presented here predicts a break in spectral index for both the loop-top and footpoint sources at  $\varepsilon = E_c = (2KN_0)^{\frac{1}{2}}$ , owing to the passage of the injected electrons through the intermediate thick-thin target at the loop apex. As explained in §3.2, the observations of Feldman *et al.* (1994) imply that  $E_c$  is in the range 15–40 keV. So the model accounts for the observed spectral break at the right energy.

The model also predicts that if the loop-top and footpoint sources are unresolved (so that only the sum of their spectra is relevant) no break in spectral index should be observed at  $E_c$ . It is not possible to test this prediction from Masuda's published data without a detailed knowledge of the instrumental response of the Yohkoh HXT (Takakura *et al.* 1993). With the appropriate knowledge, this test of the model could be straightforwardly conducted.

### 3.4.3 Behaviour at high and low energies

The model presented above also predicts specific relations between the spectral indices of the loop-top and footpoints at high and low energies. For example, the spectrum of the loop-top at low energies (i.e.  $\varepsilon \ll E_c$ ) should be the same as that of the footpoint sources at high energies ( $\varepsilon \gg E_c$ ), namely  $\delta - 1$ . Masuda's data (in the cases where both footpoint and loop-top indices were available for the same event) roughly agree with this prediction. The greatest deviation is in the 93/02/17 event, where the indices of interest differ by 2.4.

Another prediction is that the spectral indices of the loop-top at high and low energies should differ by a factor of two, the steepening indicating the transition

between thin- and thick-target over the 10–100 keV range of electron energies. There seems to be some evidence for this in Masuda’s data. Only the event of 91/12/02 shows no change in index at the loop-top between low and high energies. The same event did show a break in the footpoint spectra between low and high energies, which is difficult to explain in the context of our simple model.

Similarly the model predicts a difference of two between the spectral indices of the loop-top and footpoint sources at high energy, with the footpoint source being harder. Masuda’s data suggest that the footpoint sources are harder than the loop-top ones, but this point needs to be confirmed by a more detailed data analysis. Indirect evidence for the prediction that the footpoint sources are harder than the loop-top is provided by the observation that the average height above the photosphere of hard X-ray sources observed by Yohkoh (based on  $\approx 100$  flares) decreases with increasing energy (Kosugi, 1993).

There is also some evidence in Masuda’s data for the other specific predictions, although there are individual discrepancies.

#### 3.4.4 Type A flare observation

Another piece of evidence for the model is provided by the event of 92/02/06, which was remarkable in two ways. The first is that, in the main (gradual) phase of the flare, only a loop-top source was observed, with no corresponding footpoint emission. The second is that the spectral indices derived were the largest of the set of observations. Masuda described this event as an example of a “super-hot” or Type A flare<sup>1</sup>. This event qualitatively agrees with the model presented above, as follows. As explained in § 3.3, the relative brightness of the footpoint source is expected to decrease with increasing  $\delta$ , as the bulk of the accelerated electrons have low energy and are stopped at the loop-top (see Figure 3.4). For a steep enough injection spectrum and sufficient column depth  $N_0$ , the footpoint source should not be visible at all. Interestingly, footpoint emission was observed by Masuda in an earlier, extremely hard impulsive episode from the same flare (see Figure 3.5). This also agrees with the model presented above: the earlier burst consisted of higher energy electrons (it was most prominent in the M2 and H bands) which escaped from the loop-top source to produce footpoint emission.

---

<sup>1</sup>See § 1.2.1 of chapter 1.

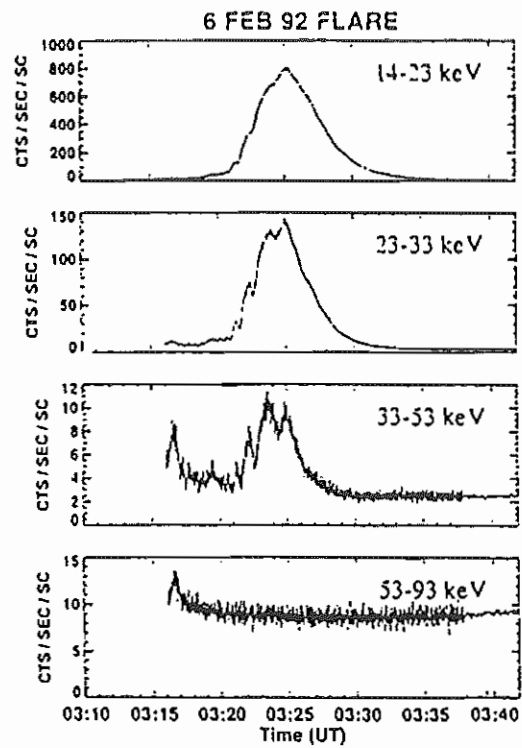


Figure 3.5: The time history of hard X-ray emission observed in the four Yohkoh bands for the flare of December 6, 1992. An early, very hard episode is seen at about 03:17. (From Masuda, 1994.)



### 3.4.5 Relative brightness of the footpoints and loop-top

The expression (3.9) (and Figure 3.4) may be compared more generally with the observation by Masuda that the loop-top impulsive source is less intense than the footpoint sources by a factor  $\leq 5$  at energies  $\geq 25$  keV. As shown in § 3.2, the observations of Feldman *et al.* imply that  $15 \text{ keV} < E_c < 40 \text{ keV}$ , so taking the cut-off energy  $\varepsilon_0 = 25 \text{ keV}$  implies  $0.6 < \varepsilon_0/E_c < 1.7$ . Consulting Figure 3.4, for reasonable  $\delta$  this range of  $\varepsilon_0/E_c$  does indeed imply a loop-top source less intense than the footpoint source by a factor less than about six. This result is subject to the caveat that Equation (3.9) does not include the instrumental response of the Yohkoh HXT (Takakura *et al.* 1993).

## 3.5 The heating of the loop-top source

When electrons are stopped at the loop-top dense region, only a small fraction of the electron energy (typically  $\approx 10^{-5}$ ) goes into producing hard X-rays. The bulk of the energy goes into collisional heating of the ambient plasma. Based on this fact, a simple model may be constructed of the heating of the loop-top source.

### 3.5.1 The energy deposited at the loop-top

The number of electrons stopped per second, per unit electron energy,  $E$ , in the dense region from  $N = 0$  to  $N = N_0$  is  $\mathcal{N} = F_0(E) - F(E, N_0)$ , and so the power deposited is  $P = \int_{E_0}^{\infty} \mathcal{N} E dE$ , where  $E_0$  is the necessary cut-off at low energy in the injected electron spectrum. The quantity  $E_0$  is probably around 10 keV, although it is difficult to determine observationally, and may be as high as 25 keV (Dennis, 1988). The expression for  $P$  may be evaluated to give

$$P = \frac{A}{\delta - 2} E_0^{-(\delta-2)} H(E_0/E_c, \delta), \quad (3.11)$$

with

$$H(\xi, \delta) = 1 - F \left[ (\delta + 1)/2, (\delta - 2)/2; \delta/2; -\xi^{-2} \right], \quad (3.12)$$

where  $F(a, b; c; x)$  is Gauss' Hypergeometric function (Abramowitz and Stegun, 1965). Equation (3.11) may be identified as containing the power injected if all the electrons are stopped, viz.  $A E_0^{-(\delta-2)}/(\delta - 2)$ , multiplied by a factor describing the fraction of electrons that are stopped ( $H$ ). Figure 3.6 shows a plot of this fraction, for relevant  $\delta$  as a function of  $E_0/E_c$ . Similar comments about the

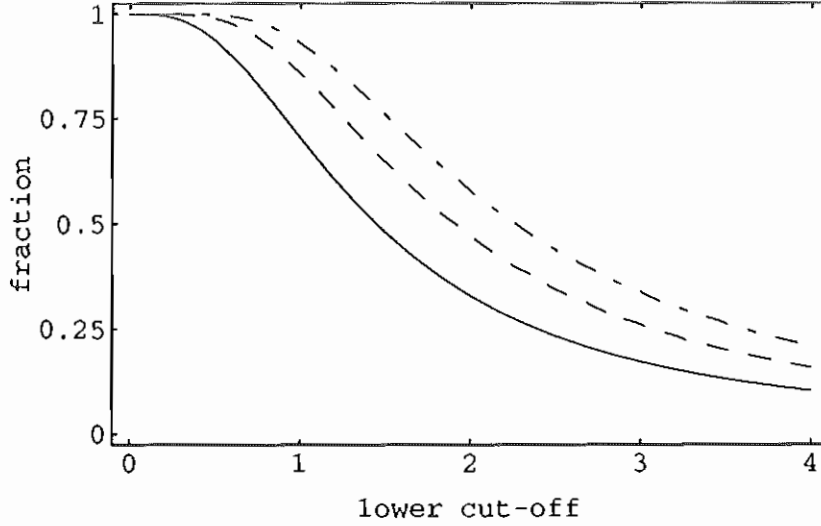


Figure 3.6: The fraction of electrons stopped at the loop-top,  $H$ , plotted as a function of  $E_0/E_c$ . The solid curve is for  $\delta = 5$ , the dashed curve  $\delta = 7$  and the dot-dashed curve  $\delta = 9$ .

general behaviour of this function can be made to those following Equations (3.9) and (3.10) above.

Equation (3.11) gives  $P$  in terms of  $A$ , which is still undetermined. Masuda quoted the loop-top count rate in the M2 band (33–53 keV) for the Jan 13 flare during its impulsive phase at 0.22 cts/s/SC, where SC refers to one of the 64 HXT subcollimators. The effective area of the HXT is  $60 \text{ cm}^2$ , so this corresponds to a photon count rate of  $2350 \text{ cts/s/m}^2$ . If this count rate corresponds to  $\int_{M2} I_{lt} d\epsilon$ , where  $I_{lt}$  is given by Equation (3.2) then we can estimate  $A$  and hence  $P$  by Equation (3.11). This approach does not take into account the detailed instrumental response of Yohkoh (Takakura *et al.* 1993), but is the best estimate possible with the available data. Taking  $E_0 = 10 \text{ keV}$  and  $\delta = 5$  we find  $2 \times 10^{20} \text{ W} < P < 7 \times 10^{20} \text{ W}$ , where the upper part of the range corresponds to the larger, less dense loop-top source ( $n_e = 10^{18} \text{ m}^{-3}$ ,  $V = 3 \times 10^{18} \text{ m}^3$ ). A characteristic impulsive timescale for the flares is about a minute, implying a total energy deposition at the loop-top in the range  $1 \times 10^{22}$ – $4 \times 10^{22} \text{ J}$ . This estimate is sensitively dependent on the cut-off energy  $E_0$ . For example, taking  $E_0 = 25 \text{ keV}$  instead of  $E_0 = 10 \text{ keV}$ , the inferred total deposited energy is in the range  $6 \times 10^{20}$ – $1 \times 10^{21} \text{ J}$ .

### 3.5.2 Comparison with the observed heating

Now let us compare the energy deposited by the energetic electrons with the energy required to account for the heating observed by Feldman *et al.* (1994). For all the 38 flares investigated by Feldman *et al.*, the maximum electron temperature observed was close to  $T_e = 2 \times 10^7$  K. This implies an energy input into the loop-top source of order  $n_e V k_B T_e$  and using the range of  $n_e$  and  $V$  derived by Feldman *et al.* we obtain the estimate of the energy going into heating the loop-top source  $10^{19}$ – $10^{21}$  J, where the upper estimate corresponds to a larger, less dense loop-top region. Comparing this estimate with the previous calculation of the energy deposited at the loop-top by the braking of electrons, clearly the  $E_0 = 25$  keV estimate of the energy deposited may be consistent with the observed heating, but the  $E_0 = 10$  keV estimate implies that significantly more energy is being deposited at the loop-top by stopping electrons than appears in the heating of the loop-top as observed by Feldman *et al.* This critical dependence on  $E_0$  is a familiar problem in the context of flare electron beam energetics (Dennis, 1988). Certainly the model provides deposition of enough energy at the loop-top by the process of stopping electrons to account for the heating observed by Feldman *et al.*

The modified model presented in §3.3.7 above is capable of producing a smaller deposition of energy at the loop-top if a small value of  $f$  is chosen, so that most electrons do not encounter the loop-top dense region. However, this solution is implausible for two reasons. As discussed in §3.3.7, if  $f$  is small, the loop-top hard X-ray source is reduced in brightness by  $f$  and the footpoint source does not exhibit a significant break in index. The calculation of  $r(\epsilon > \epsilon_0)$  in §3.4.5 implies that the brightness of the loop-top region with  $f = 1$  is qualitatively consistent with Masuda's observations, so  $f$  cannot be small. Also, Masuda's spectral index estimates (Table 3.1) do not support the prediction (valid for small  $f$ ) that the footpoint source exhibit no break in index.

Another way of resolving the possible inconsistency between the model estimate of the energy deposited by electrons and the energy associated with the observed heating is in terms of an inhomogeneous model. Specifically, suppose that the loop-top region consists of regions of dense material embedded in less dense plasma. The denser material is heated less rapidly as the energetic electrons are stopped and because of the sensitive dependence of the response of the SXT to temperature (Tsuneta *et al.* 1991), only the thinner material may be vis-

ible in soft X-rays. Then the dense regions produce hard X-rays when they stop electrons but no appreciable soft X-ray emission. The details of such a model for the heating of the loop-top region are being investigated.

### 3.6 Discussion

The model developed above accounts well for some of the wealth of observational detail provided by Yohkoh. Nevertheless, many questions remain to be answered. The most unsatisfactory aspect of the model is the description of the dense loop-top region and the introduction of the energetic electrons into this region. This part of the model is consistent with the few observational details provided by Feldman *et al.* (1994). However, the model does not address the deeper questions of the mechanisms of electron acceleration and more generally, of flare energy release. Dense coronal plasma is assumed to be located in a small region at the loop-top at the onset of the flare. This region is presumably produced by the flare energy release mechanism. The electrons may be accelerated in the dense region itself, or perhaps arrive there (already energised) from above. The dense loop-top region is rapidly heated by impinging electrons, and so should expand along field lines. Feldman *et al.* reported that the impulsive soft X-ray sources observed remained pointlike throughout the period of observation, and so a mechanism for confinement of the heated plasma is implied. A more detailed model should describe the physics of such a confinement process, and this will be the subject of future work.

Masuda's co-aligned soft and hard X-ray images appear to show a systematic displacement of 3/10 of the observed loop-top hard X-ray sources above the loop as outlined in soft X-ray. The best example is provided by the Jan 13 event (see Figure 3.1; also Masuda *et al.* 1994). The apparent displacement of the hard X-ray source in these instances was interpreted by Masuda (1994) to suggest flare energy release occurring from above. The model presented here implies spatially coincident loop-top soft and hard X-ray sources, since they arise from the interaction of energised electrons with the same dense region. Future observations will confirm or deny the reality of the displacement.

One flare energy release mechanism (involving the production of a dense loop-top region) is the theoretical model of Forbes and Malherbe (1986). Reconnection is assumed to proceed between magnetic field lines above the loop and a wedge-

shaped shock is produced where one reconnection jet (outflow) impinges on the loop, near its apex. This model has not been developed enough to predict the details of expected hard and soft X-ray emission at the loop-top. The model developed above is compatible with Forbes and Malherbe's (1986) model because it allows the possibility that electrons are energised at a remote site, say above the loop, and then propagate along field lines to the dense loop-top regions.

As discussed above, the model may imply that more energy is deposited at the loop-top than appears in soft X-ray, suggesting that this region may be highly non-uniform.

The model presented here has many restrictive assumptions that should be relaxed in a more realistic treatment. First, the change in the electron flux spectrum described by Equation (3.1) neglects changes in average pitch angle of the injected electrons. A more detailed description must take some account of this process (e.g. Leach and Petrosian, 1981). Magnetic mirroring of energetic electrons as they approach the stronger fields of the footpoints has also been neglected, although this may be an important aspect of the physics of electron precipitation to the chromosphere (e.g. Melrose and White, 1981). The gradually increasing density of the solar atmosphere with decreasing depth is treated here as a step in density, identified with the chromospheric boundary. A more detailed model should incorporate a better description of the solar atmosphere.

### 3.7 Conclusions

A simple model is presented here to account for the Yohkoh soft and hard X-ray observations of Feldman *et al.* (1994) and Masuda (1994). The basis of the model is the assumption that 10–100 keV electrons accelerated by the flare traverse the dense, small regions observed in soft X-ray by Feldman *et al.* at the apex of flaring coronal loops. The values of density and volume derived by Feldman *et al.* imply that these regions present an intermediate thick-thin target to electrons passing outwards through them. Specifically, the regions represent a column depth  $10^{24} \text{ m}^{-2} < N_0 < 7 \times 10^{24} \text{ m}^{-2}$  and are thick (thin) targets to electrons with energy much less (greater) than  $E_c = (KN_0)^{\frac{1}{2}}$ , with  $15 \text{ keV} < E_c < 40 \text{ keV}$ . A fraction of the accelerated electrons are stopped in the dense loop-top region, leading to heating of the loop-top region and production of hard X-rays via bremsstrahlung. The loop-top soft X-ray source is identified as a

region of dense coronal material, which is present at the flare onset and which is heated *in situ* by energetic electrons impinging on it. This is in contrast to ‘chromospheric evaporation’ models in which the coronal soft X-ray emission is attributed to chromospheric material evaporated into the coronal loop from its footpoints. Coincident soft and hard X-ray flare observations favour *in situ* heating over evaporation (Feldman, 1990).

Adopting a simple model for the way in which electrons lose energy in precipitating to the footpoints, theoretical individual hard X-ray spectra are derived for the loop-top dense region, the thick-target sources at the footpoints of the loop, and the thin-target region between loop-top and footpoints. The model loop-top and footpoint spectra are compared with the spectral estimates of Masuda, and the simple model is found to agree qualitatively with the data, although there are individual discrepancies. In particular, the model accounts naturally for the observed steepening in the spectral indices of both loop-top and footpoint sources between 14 keV and 53 keV, and predicts that there is no corresponding steepening in the spectral index of the sum of the loop-top and footpoint sources. The model also provides an explanation for Masuda’s Type A or “super-hot” flare observation of 92/02/06, when a loop-top hard X-ray source was seen with no corresponding footpoint emission. If the injected electron spectrum at the loop-top is steep enough, and/or the column depth of the loop-top region is large enough, almost all the electrons are stopped at the loop-top, leading to only a loop-top source. More generally, the model spectra plausibly account for the observed relative brightnesses of the footpoint and loop-top sources. They also suggest an independent observational method of determining  $E_c$ , as the photon energy at which the loop-top and footpoint sources are equally bright.

The model allows the calculation of the energy deposited in the dense loop-top region by the braking of electrons. This is compared with the heating observed by Feldman *et al.* and the model implies that (at least) enough energy is deposited at the loop-top to account for the heating observed in soft X-ray. Depending on the (observationally poorly constrained) choice of the low energy cut-off to the electron spectrum, it is possible that significantly more energy is deposited at the loop-top than appears in soft X-ray. This discrepancy, if real, may suggest that the loop-top region is highly inhomogeneous. If the loop-top region consists of dense material embedded in less dense material, the energy deposited in the dense material may raise its temperature less than if the same energy were deposited in

the less dense material. Hence the energy deposited in the dense material does not appear in soft X-ray.

In conclusion, our model qualitatively accounts for some details of recent Yohkoh hard and soft X-ray flare observations. The model is, however, clearly oversimplified and in particular does not address the central question of the mechanism of solar flare energy release. Further work, directed towards accounting for the details of the loop-top X-ray sources observed by Masuda may shed some light on this deeper problem.

## 3.8 APPENDIX

### 3.8.1 Derivation of Equations (3.2)—(3.5)

The treatment given in this section follows Brown and McClymont (1975), but has been repeated to clarify an error in that paper, as indicated below.

The direction integrated photon spectrum,  $I(\varepsilon)$ , from an unresolved source of volume  $V$  is given by (Brown, 1975)

$$4\pi R^2 I(\varepsilon) = \int_{\varepsilon}^{\infty} \left[ \int_V n_e(\mathbf{r}) \frac{dn^b}{dE}(E, \mathbf{r}) d^3\mathbf{r} \right] Q_{\varepsilon}(E) v(E) dE, \quad (3.13)$$

where  $n_e(\mathbf{r})$  is the ambient number density at a point  $\mathbf{r}$  in the source,  $dn^b(E, \mathbf{r})/dE$  is the beam number density per unit electron energy,  $E$ , at the point  $\mathbf{r}$ ,  $Q_{\varepsilon}(E)$  is the direction integrated cross section for bremsstrahlung emission, and  $v(E)$  is the velocity of an electron of energy  $E$ . We assume that the X-ray emitting region is optically thin, which is valid for  $n_e \leq 10^{23} \text{ m}^{-3}$ , a condition that is certainly always met in the chromosphere and corona (Brown, 1971). The cross section  $Q_{\varepsilon}(E)$  in Equation (3.13) is differential in photon energy  $\varepsilon$  (so its units are area per unit photon energy). For the energy range of interest in solar flare hard X-ray emission ( $< 100 \text{ keV}$ ), an approximate cross section for bremsstrahlung is provided by the non-relativistic Bethe-Heitler formula (Jackson, 1962), viz.

$$Q_{\varepsilon}(E) = \frac{\kappa_{BH} \bar{Z}^2}{\varepsilon E} \ln \frac{1 + \sqrt{1 - \varepsilon/E}}{1 - \sqrt{1 - \varepsilon/E}}, \quad (3.14)$$

where  $\bar{Z}$  is the average atomic number of the ambient plasma, and  $\kappa_{BH} = 8\alpha r_0^2 m_e c^2 / 3$ , with  $r_0$  being the classical radius of the electron and  $\alpha$  the fine structure constant. Note that, for  $\varepsilon$  less than  $E$ ,  $Q_{\varepsilon}(E)$  is zero; an electron of a particular energy cannot produce a photon of greater energy.

Most theoretical descriptions of solar flare hard X-ray emission have taken the Bethe-Heitler formula as a starting point (e.g. Lin and Hudson, 1971; Brown, 1971; Brown, 1975; Brown and McClymont, 1975), although simpler forms have also been used (e.g. Emslie and Machado, 1987). Whilst the Bethe-Heitler formula is a convenient theoretical tool (it represents the most complex cross section for which analytic descriptions of X-ray emission are possible), it is worthwhile to remember its shortcomings. States of polarisation and direction of the emitted photons have already been summed and integrated over respectively, so Equation (3.14) affords no information on the polarisation and directivity of the pho-



ton emission. Various authors have considered these questions (e.g. Brown, 1972; Brown, 1975; Leach and Petrosian, 1983). Polarimetry measurements hold the promise of distinguishing between thermal and non-thermal models for hard X-ray emission, because a directed beam of electrons produces polarised emission, whereas a uniform hot plasma does not. Unfortunately, uncertainties in measurements to date have been too large to draw useful conclusions from the data (Dennis, 1988). More definitive measurements present a challenge to instrument design. The discussion of solar flare X-ray emission presented above neglects the questions of polarisation and direction dependence of emission.

We assume axisymmetry of the electron beam, so that  $dn^b(E, \mathbf{r})/dE$  depends only on the coordinate  $z$ , and for simplicity consider a source in which the ambient number density,  $n_e$ , is constant. The the column depth of the source,  $N = n_e z$ , provides a coordinate to describe the beam. The flux spectrum at depth  $N$  of the beam,  $F(E, N)$  (as defined above), is given by  $dn^b(E, N)/dE = F(E, N)/Sv(E)$ . Equation (3.13) can then be rewritten to describe the differential emission along the beam:

$$\frac{dI}{dN} = \frac{1}{4\pi R^2} \int_{\varepsilon}^{\infty} F(E, N) Q_{\varepsilon}(E) dE. \quad (3.15)$$

Substituting Equation (3.1) with the initial flux spectrum  $F_0(E) = AE^{-\delta}$  into Equation (3.15) and changing the variable of integration to  $x = \varepsilon/E$ , we obtain

$$\frac{dI}{dN} = \frac{A\kappa_{BH}\bar{Z}^2}{4\pi R^2} \varepsilon^{-(\delta+1)} \int_0^1 x^{\delta-1} \left(1 + 2KNx^2/\varepsilon^2\right)^{-\frac{1}{2}(\delta+1)} f(x) dx, \quad (3.16)$$

where  $f(x) = \ln[(1 + \sqrt{1-x})/(1 - \sqrt{1-x})]$ . Equation (3.16) has a difference in exponent in the integrand to the corresponding expression deduced by Brown and McClymont (1975).

Thin-target behaviour can be derived from Equation (3.16) by expanding the integrand in small  $KN/\varepsilon^2$  and then integrating the result with respect to  $N$ . Keeping only the term of order  $N$ , the result is

$$I_{\text{thin}}(\varepsilon) = \frac{A\kappa_{BH}\bar{Z}^2 N}{4\pi R^2} \frac{B(\delta, \frac{1}{2})}{\delta} \varepsilon^{-(\delta+1)}, \quad (3.17)$$

where  $B(p, q) = \Gamma(p)\Gamma(q)/\Gamma(p+q)$  is the Beta function (Abramowitz and Stegun, 1965). Equation (3.17) is the usual thin-target formula (Brown, 1971).

The photon spectrum from a source of arbitrary column depth, say  $N_0$ , is obtained by integrating Equation (3.16) from  $N = 0$  to  $N = N_0$ . The result is Equations (3.2)—(3.5). In the limit  $N_0 \rightarrow \infty$ , thick-target behaviour is returned,

viz. Equation (3.3). This limit is important because it relies on the exponent in Equation (3.16) and establishes that Brown and McClymont's (1975) result is in error.

### 3.8.2 Derivation of Equations (3.6) and (3.7)

As explained above, the electron flux spectrum everywhere between the loop-top and footpoints is assumed to be  $F(E, N_0)$ , where  $F$  is given by Equation (3.1), and  $F_0(E) = AE^{-\delta}$ . Substituting this flux spectrum into Equation (3.15) and integrating with respect to  $N$  (the integrand is independent of  $N$  under the present assumptions) from  $N = 0$  to  $N = N_a$  gives Equations (3.6) and (3.7).

## Chapter 4

# Cross-field current closure below the solar photosphere

**Abstract:** A simple, two-dimensional model is developed to describe how an externally imposed current closes as a function of time below the photosphere. A vertical current density is assumed to turn on at the photospheric boundary, such that the current is directed vertically into the photosphere in one half of the photospheric boundary, and vertically out in the other half. The model implies that the closure of the current in the subphotosphere depends only on the magnetic Reynolds number  $R_M$ , which may be expressed in the ratio  $R_M = R_A/R$ , where  $R_A = \mu_0 v_A$  is the Alfvénic impedance of the photosphere and  $R = 1/\sigma_P l$  is the resistance corresponding to the conductivity  $\sigma_P$  and a characteristic length  $l$ . For  $R_M \gg 1$ , current closure occurs at a front, propagating with the Alfvén speed. For  $R_M \ll 1$ , current closure is a diffusive process ahead and behind a slowly propagating Alfvénic front. The first case is the relevant one for the Sun, where  $R_M \approx 10^8/v_A$ , for  $v_A$  in kilometres per second.

The model implies that the boundary condition of 'line-tying,' often imposed to describe the behaviour of plasma and fields at the photospheric boundary, is only valid for the Alfvén transit time of any given layer of the solar atmosphere. The consequences for the dynamics of coronal magnetic structures are explored.

## 4.1 Introduction

The question of what happens to currents that flow in the corona as they reach the photosphere is a controversial one in solar physics. Vector magnetogram data<sup>1</sup> typically show regions of strong current ( $\approx 10^{12}$  A) flowing into the photosphere in a region of one magnetic polarity and out of the photosphere in an adjacent region of opposite polarity (Moreton and Severny, 1968; Krall *et al.* 1982; Ding *et al.* 1987; Lin and Gaizauskas, 1987; Hagyard, 1988; Romanov and Tsap, 1990; Canfield *et al.* 1993; Leka *et al.* 1993; de La Beaujardière *et al.* 1993). This is interpreted as a photospheric cross-section of a coronal magnetic loop carrying an unneutralized axial current (Melrose, 1991), although a contrary opinion was expressed by Wilkinson *et al.* (1992). The current is assumed to be field-aligned in the coronal part of the loop, where gas pressure is negligible. The behaviour of this current below the photosphere — in particular whether it closes across field lines there — is open to question. Some authors (Hudson, 1987; McClymont and Fisher, 1989; Melrose, 1991) claimed that the observed currents flow through the subphotosphere along field lines, coupling the corona to the deep interior of the Sun. Other authors (e.g. Kan *et al.* 1983) argued that the large scale currents observed (which are associated with solar flares) are generated at the photosphere by fluid motions: the so-called photospheric dynamo. A third possibility is implicit in a wide class of models for coronal structures in which the boundary condition at the photosphere is taken to be the ‘line-tying’ assumption (Van Tend and Kuperus, 1978; Priest, 1982; Bray *et al.* 1991). As shown below, line-tying implies that coronal currents close in the photospheric boundary, independent of background magnetic field lines, an implication incompatible with the properties of the photosphere.

We consider a simple model for the dynamic response of the subphotospheric plasma to a current imposed from above. The objective is to determine the conditions under which the imposed current closes across field lines locally in the photosphere (as implied by the line-tying assumption) and when closure occurs far below the photosphere (as argued by Hudson, 1987). Our approach is to assume a two-dimensional, constant density, isotropically conducting photosphere threaded by a vertical, uniform magnetic field. The photosphere occupies the plane  $z \geq 0$  (no variation is permitted in  $y$ ) and a vertical current density  $J_z$  is assumed to

---

<sup>1</sup>See § 1.2.2 of chapter 1.

turn on in the photospheric boundary at a particular time ( $t = 0$ ), introducing a total current  $I_0$  into the subphotosphere. This current must close across field lines in the model subphotosphere for all later times. The problem posed is the specification of  $J_x$  and  $J_z$  for all  $x$ ,  $z$  and  $t > 0$ , which completely describes how the current closes.

The assumption that coronal magnetic structures are line-tied at the solar photosphere implies that magnetic field lines joining the photosphere to the corona are frozen-in to the subphotospheric plasma and so are fixed immovably there by the inertia of the denser plasma below. Line-tying implicitly requires that coronal currents close across field lines, as surface currents in the photospheric boundary. For example, consider a coronal arcade, subject to a shear. If the magnetic field at one line of footpoints of the arcade is assumed to be initially vertical at the photosphere (of magnitude  $B_0$ , say), then line-tying implies that after shearing, a kink appears in the field lines there. This kink implies a non-zero  $\nabla \times \mathbf{B}$  at the photosphere, and hence a non-zero surface current there. Specifically, if the kink is a departure  $\theta$  from the vertical, then a surface current  $B_0 \tan \theta / \mu_0$  must flow, perpendicular to the plane of the kinked field.

The surface current implied by line-tying must be set up by a sequence of events in which a coronal current is imposed on the photospheric boundary. To understand this point, consider Figure 4.1. A shear imposed at one row of footpoints of a coronal arcade drives a current along the coronal field lines of the arcade. If the photospheric motion is slow compared with the Alfvén propagation time in the corona, the shearing of the arcade may be considered as a sequence of magnetostatic equilibrium states in which the footpoints of the arcade are successively displaced (e.g. Low, 1977; Priest, 1982; Finn and Chen, 1990). Each equilibrium state in the sequence has a greater field-aligned current flowing in the coronal part of the arcade, and closing (because of line-tying) in the photospheric boundary at the passive footpoint. This cross-field boundary current must be set up as the magnetostatic response of the passive footpoint to an increased current density arriving from above, along the field lines.

A second example of the line-tying assumption is provided by Kuperus and Raadu's (1974) model for the support of prominences. Figure 4.2 shows the model, in which a current-carrying filament is introduced into the corona and induces surface currents in the photospheric boundary, because of line-tying. The induced currents support the filament through current-current interaction. The

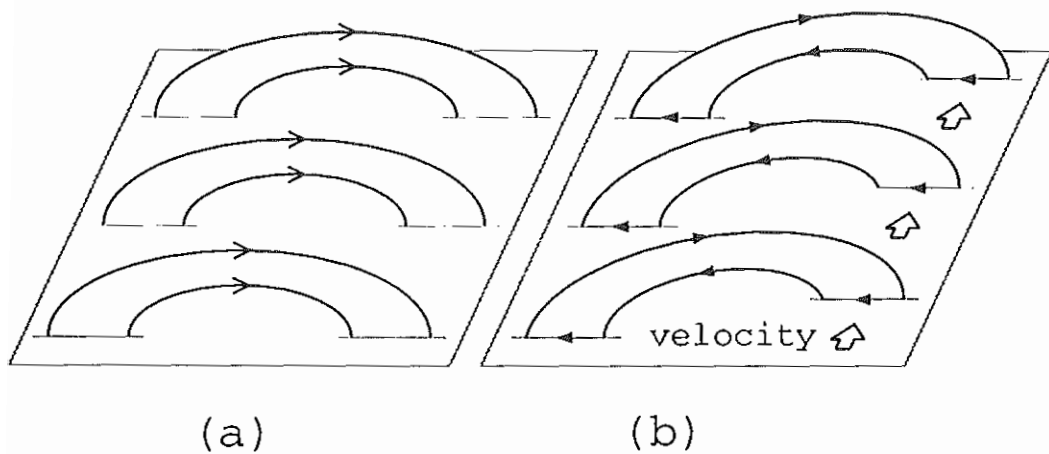


Figure 4.1: A theoretical model for the shearing of one side of a coronal arcade. In (a), the arcade is shown before any shearing: the open arrow heads denote the direction of the field. The photospheric boundary is the plane shown. In (b), the arcade is subject to a shearing velocity field in the photosphere at the right hand row of footpoints. This plasma motion drives a current in the photospheric boundary that flows along the magnetic field over the arch of the arcade. The current is denoted by the closed arrowheads of the figure. The line-tying boundary condition implies that this current closes across field lines at the passive row of footpoints, as shown.

initial (pre-filament) magnetic field is predominantly vertical at the photosphere and so current closure there must occur perpendicular to the magnetic field. The surface current induced at the photospheric boundary is the closure current for the coronal filament current, set up after the filament is introduced (e.g. Martens, 1987). Variants of the model have been proposed (Van Tend and Kuperus, 1978; Lerche and Low, 1980; Martens, 1987; Martens and Kuin, 1989; Priest and Forbes, 1990), and all rely on the same assumption about the photosphere. The model developed here tests the validity of the line-tying assumption at the photosphere by considering the response of the subphotosphere to currents imposed from above.

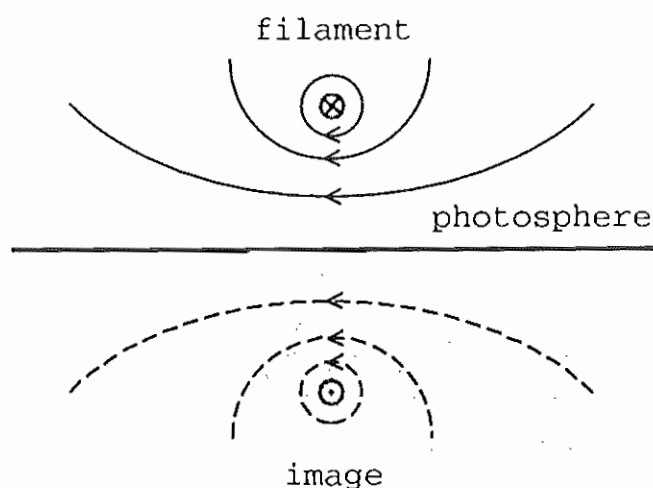


Figure 4.2: Kuperus and Raadu's (1974) model for the support of a current-carrying filament introduced into the solar atmosphere. The line-tying boundary condition is assumed to prevent the field of the introduced filament from crossing the photospheric boundary. This is modelled by placing an image filament below the solar photosphere, as shown. In the figure, only the magnetic field of the filament and its image are shown. The ambient magnetic field (not shown) is predominantly vertical. It is implicit in this model that electric currents can flow arbitrarily in the photospheric boundary.

This chapter is divided as follows. In §4.2 a simple description of current closure in a model photosphere is presented, which becomes the basis in §4.3 for a model of the response of the subphotosphere to a current applied from above. The various limiting cases in which analytical solutions to the model exist are investigated in §4.4. The general case requires numerical solution, which is discussed in §4.5, together with the consequences of the model for solar parameters. The

main results of the model are summarised in §4.6. In §4.7, the question of how the imposed current density appears in the photospheric boundary is addressed. §4.8 presents a simple model for the shearing of a coronal arcade consistent with the conclusions of the model (§4.6) developed to describe current closure in the subphotosphere. The details of various derivations have been relegated to the Appendix, §4.10.

## 4.2 Description of subphotospheric currents

Consider the following two-dimensional ( $\partial/\partial y = 0$ ) forms for fluid velocity and magnetic field, respectively, in a model photosphere (Scholer, 1970):

$$\mathbf{v} = [0, v_y(x, z, t), 0], \quad \mathbf{B} = [0, B_y(x, z, t), B_z(x)]. \quad (4.1)$$

The photosphere is assumed to occupy the half-space  $z \geq 0$ , threaded by a background field  $B_z(x)$ . For the purposes of the model we consider only those cases where  $B_z^2$  is constant. Two specific cases of interest are  $B_z = B_0$  and also the simple form

$$B_z(x) = \begin{cases} B_0 & \text{if } x > 0, \\ -B_0 & \text{if } x < 0, \end{cases} \quad (4.2)$$

representing an idealised photospheric field with a neutral (or inversion) line. These two choices are shown in Figure 4.3. The geometry adopted implies cross-field and parallel current densities

$$\mathbf{J} = \frac{1}{\mu_0} \left( -\frac{\partial B_y}{\partial z}, 0, \frac{\partial B_y}{\partial x} \right). \quad (4.3)$$

The photosphere is modelled here as a single resistive fluid with isotropic conductivity  $\sigma_P$ . The simple Ohm's law

$$\mathbf{J} = \sigma_P(\mathbf{E} + \mathbf{v} \times \mathbf{B}), \quad (4.4)$$

is assumed to apply, where  $\mathbf{E}$  is the electric field present. The use of Equation (4.4) is discussed in the Appendix to this chapter (§4.10.1).

Assuming also a constant-density photosphere, Maxwell's equations and the fluid equation of motion imply the pressure balance

$$p = p_0 - B_y^2/2\mu_0 \quad (4.5)$$



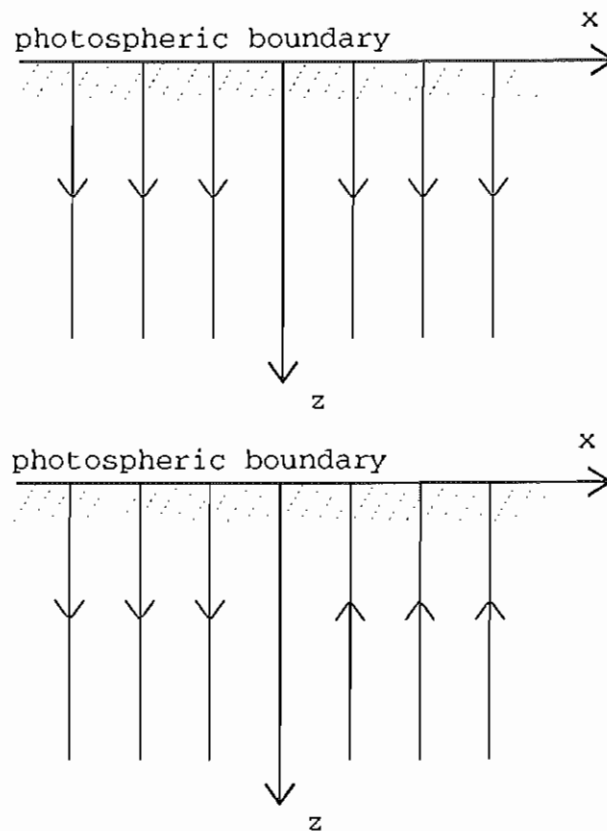


Figure 4.3: The geometry of the simple model photosphere considered, with two possible field configurations. In the upper picture the background field is uniform and in the lower picture it is oppositely directed in  $x > 0$  and  $x < 0$ .

and the partial differential equation for the magnetic field

$$\frac{\partial^2 B_y}{\partial t^2} - v_A^2 \frac{\partial^2 B_y}{\partial z^2} - \frac{1}{\gamma} \frac{\partial}{\partial t} \left( \frac{\partial^2 B_y}{\partial x^2} + \frac{\partial^2 B_y}{\partial z^2} \right) = 0, \quad (4.6)$$

where  $v_A = B_0/(\mu_0\rho_0)^{\frac{1}{2}}$  is the Alfvén speed and  $\gamma = \mu_0\sigma_P$ . The components of the current density obey the same partial differential equation and may be obtained from Equation (4.3). Equation (4.6) has been discussed by Alfvén and Fälthammar (1963), and is derived in the Appendix to this chapter (§ 4.10.1).

Several restrictive assumptions are adopted in the derivation of Equation (4.6) which require comment. The restrictive geometry adopted allows only transverse perturbations of the subphotosphere. Together with the assumption of constant density, this means that only transverse Alfvén waves are considered. These provide the mechanism of dynamic current closure. The role of magneto-acoustic waves is ignored. The stratification of the solar atmosphere is also neglected for simplicity: this is also not expected to influence the basic results presented. Inhomogeneities in the subphotospheric magnetic field are also neglected. A more sophisticated treatment would consider the role of variations in the magnetic field. The subphotosphere is assumed to be isotropically conducting. In fact, the subphotosphere is a partially ionised gas, with a significantly anisotropic conductivity (Khan, 1989). The simplest magnetohydrodynamic (MHD) description of the conductivity of the subphotosphere must involve a Hall current (with corresponding conductivity  $\sigma_H$ ) in addition to the Pederson current described here by  $\sigma_P$  (Krall and Trivelpiece, 1973). The neglect of the Hall term is consistent with the neglect of  $J_y$ , as discussed in the Appendix to this chapter (§ 4.10.1). Both would need to be considered in a more general model.

### 4.3 Model for response of the subphotosphere to a current imposed from above

A solution to Equation (4.6) in the half space  $z \geq 0$  is presented below, subject to the boundary condition

$$J_z(x, z = 0, t) = f(x)\theta(t), \quad (4.7)$$

where  $\theta(t)$  is the step function. The initial conditions assumed are those appropriate to Laplace transform problems,

$$J_z(x, z, t = 0) = \left. \frac{\partial J_z}{\partial t} \right|_{t=0} = 0. \quad (4.8)$$

Equation (4.7) prescribes a vertical current density  $f(x)$  in the photospheric boundary for  $t > 0$ . This function is assumed to be odd in  $x$ , so that current enters the half-space  $z \geq 0$  in the half-plane  $z = 0$ ,  $x > 0$  and leaves in  $z = 0$ ,  $x < 0$ . A total current  $I_0$  flows in the photosphere for  $t > 0$ , defined by:

$$I_0 \equiv \int_0^\infty dx' f(x') = - \int_{-\infty}^0 dx' f(x'). \quad (4.9)$$

This current must close across field lines in the photosphere.

The equivalent boundary and initial conditions on  $B_y$  are, respectively,

$$B_y(x, z = 0, t) = \mu_0 \phi(x) \theta(t) \quad (4.10)$$

and

$$B_y(x, z, t = 0) = \left. \frac{\partial B_y}{\partial t} \right|_{t=0} = 0, \quad (4.11)$$

with

$$\phi(x) = \int_{-\infty}^x dx' f(x'). \quad (4.12)$$

The lower limit in Equation (4.12) is determined by the requirement that  $B_y$  approaches zero for large  $x$ . A simple choice of  $f(x)$  is the delta function profile

$$f(x) = I_0 [\delta(x - x_0) - \delta(x + x_0)], \quad (4.13)$$

which implies

$$\phi(x) = \begin{cases} -I_0 & \text{if } |x| < x_0, \\ 0 & \text{otherwise.} \end{cases} \quad (4.14)$$

This choice corresponds to a current sheet directed into the model photosphere at  $x = x_0$  and out at  $x = -x_0$ . The delta function choice is considered here, along with the general case.

In the Appendix to this chapter (§4.10.2) it is shown that the Laplace transform of the solution to Equation (4.6) subject to these boundary and initial conditions is

$$\tilde{B}_y(x, z, s) = \frac{\mu_0 \alpha z}{\pi} \left( \frac{\gamma}{s} \right)^{\frac{1}{2}} \int_{-\infty}^{\infty} d\xi \phi(\xi) \frac{K_1 \left( \left\{ \gamma s [\alpha^2 z^2 + (x - \xi)^2] \right\}^{\frac{1}{2}} \right)}{[\alpha^2 z^2 + (x - \xi)^2]^{\frac{1}{2}}}, \quad (4.15)$$

with

$$\alpha^2 = \frac{s}{s + \gamma v_A^2} \quad (4.16)$$

and where  $K_1$  is the modified Bessel function of the second kind (Abramowitz and Stegun, 1965).

In general, Equation (4.15) does not correspond to a tabulated Laplace transform (e.g. Erdélyi *et al.* 1954). Various limiting cases permit inversion of this transform and these are investigated below. Consider first, however, the total current crossing the plane  $x = 0$ . It is straightforward to verify from Equation (4.15) that this quantity is  $-I_0$ , as is required by continuity of current. To describe where cross-field current closure occurs in this model photosphere for  $t > 0$ , it is only necessary to obtain the current density  $J_x$  in the plane  $x = 0$ , rather than considering  $J_x$  everywhere in  $z \geq 0$ .

An alternative way to characterise how the current closes in general is to consider the total current closing in the plane  $x = 0$  above a height  $z = h$ :

$$I_{\perp}(h, t) = -I_0 - \frac{1}{\mu_0} B_y(x = 0, z = h, t). \quad (4.17)$$

This quantity decreases from zero at  $h = 0$  to approach  $-I_0$  asymptotically as  $h$  tends to infinity.

## 4.4 Limiting cases

Various limiting cases provide insight into the general behaviour of the model.

### 4.4.1 Infinite conductivity ( $\gamma \rightarrow \infty$ )

In the limit  $\gamma \rightarrow \infty$ , Equation (4.6) becomes the one-dimensional wave equation. In the Appendix to this chapter (§4.10.3) it is shown from Equation (4.15) that

$$\lim_{\gamma \rightarrow \infty} \tilde{B}_y(x, z, s) = \frac{\mu_0}{s} \phi(x) \exp(-sz/v_A), \quad (4.18)$$

which yields the solution to the wave equation

$$\lim_{\gamma \rightarrow \infty} B_y(x, z, t) = \mu_0 \phi(x) \theta(t - z/v_A). \quad (4.19)$$

Denoting this limit ‘ $P$ ’ (for propagating), the corresponding current densities are

$$J_x^P(x, z, t) = \frac{\phi(x)}{v_A} \delta(t - z/v_A) \quad (4.20)$$

and

$$J_z^P(x, z, t) = f(x)\theta(t - z/v_A). \quad (4.21)$$

The interpretation of Equations (4.20) and (4.21) is that current closure occurs at an Alfvénic front propagating into the photosphere. In the plane  $x = 0$ , the cross-field current is

$$J_x^P(x = 0, z, t) = -\frac{I_0}{v_A}\delta(t - z/v_A), \quad (4.22)$$

so in the absence of diffusion, a propagating delta function of cross-field current is seen in the plane of symmetry of the model.

#### 4.4.2 Zero Alfvén speed ( $v_A \rightarrow 0$ )

In the limit of zero Alfvén speed, Equation (4.6) becomes the two-dimensional diffusion equation. Denoting this limit ‘ $D$ ’ (for diffusive), Equation (4.15) becomes

$$\begin{aligned} \tilde{B}_y^D(x, z, s) &= \lim_{v_A \rightarrow 0} \tilde{B}_y(x, z, s) \\ &= \frac{\mu_0 z}{\pi} \left(\frac{\gamma}{s}\right)^{\frac{1}{2}} \int_{-\infty}^{\infty} d\xi \phi(\xi) \frac{K_1\left(\{\gamma s [z^2 + (x - \xi)^2]\}^{\frac{1}{2}}\right)}{[z^2 + (x - \xi)^2]^{\frac{1}{2}}}, \end{aligned} \quad (4.23)$$

which can be inverted (Erdélyi *et al.* 1954) to give the classical Green’s function solution to the diffusion equation (Morse and Feshbach, 1953)

$$B_y^D(x, z, t) = \frac{\mu_0 z}{\pi} \int_{-\infty}^{\infty} d\xi \frac{\phi(\xi)}{z^2 + (x - \xi)^2} \exp\left\{-\frac{\gamma}{4t} [z^2 + (x - \xi)^2]\right\}. \quad (4.24)$$

It is straightforward to write down  $J_x^D$  and  $J_z^D$  from Equation (4.24) using Equation (4.3) but here note only that the cross-field current in the plane  $x = 0$  is

$$\begin{aligned} J_x^D(x = 0, z, t) &= \frac{2}{\pi} \int_0^{\infty} d\xi \phi(\xi) \\ &\quad \times \left[ \frac{\gamma z^2 / 2t}{z^2 + \xi^2} - \frac{-z^2 + \xi^2}{(z^2 + \xi^2)^2} \right] \exp\left[-\frac{\gamma}{4t}(z^2 + \xi^2)\right]. \end{aligned} \quad (4.25)$$

Figure 4.4 illustrates this current density for the delta function choice of  $f(x)$ , Equation (4.13). As  $t \rightarrow \infty$  it approaches the asymptotic form

$$J_x^D(x = 0, z, t \rightarrow \infty) = -\frac{2I_0 x_0}{\pi(x_0^2 + z^2)}. \quad (4.26)$$

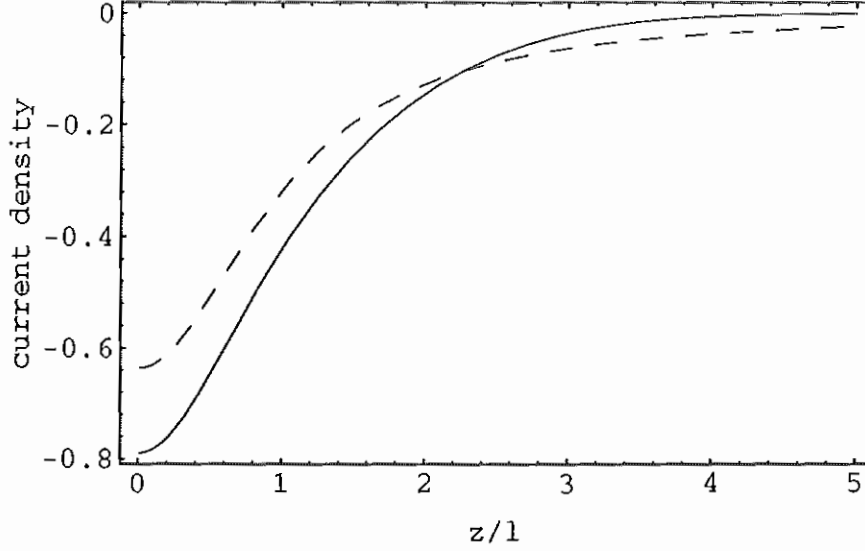


Figure 4.4: The scaled current density  $J_x^D(x=0, z, t)/(I_0/l)$  as a function of scaled distance into the photosphere for one diffusive timescale, and in the steady state limit of an infinite number of such timescales. The dashed curve is the asymptotic case.

In this limit, cross-field current closure occurs for all relevant timescales in a region just below the photospheric boundary. Figure 4.5 shows the vector field of current density  $(J_x^D, J_z^D)$  in the limit  $t \rightarrow \infty$ . This behaviour is consistent with Kuperus and Raadu's (1974) model for support of current-carrying filaments. However, as discussed below, the solar behaviour is much closer to the limit of infinite conductivity than that of zero Alfvén speed.

#### 4.4.3 Steady state ( $t \rightarrow \infty$ )

The asymptotic time behaviour of Equation (4.6) can be obtained directly by setting  $\partial/\partial t$  to zero, or more formally by evaluating  $\lim_{s \rightarrow 0} s \tilde{B}_y(x, z, s)$  using Equation (4.15). The behaviour of the system depends only on whether the Alfvén speed is zero or not.

If  $v_A = 0$ , setting  $\partial/\partial t$  to zero in Equation (4.6) gives the Poisson equation, which may be solved subject to the boundary conditions. Alternatively, the behaviour is described by Equation (4.24) in the limit  $t \rightarrow \infty$ , i.e.

$$B_y^D(x, z, t \rightarrow \infty) = \frac{\mu_0 z}{\pi} \int_{-\infty}^{\infty} d\xi \frac{\phi(\xi)}{z^2 + (x - \xi)^2}. \quad (4.27)$$

The cross-field current density in the plane of symmetry of the model correspond-

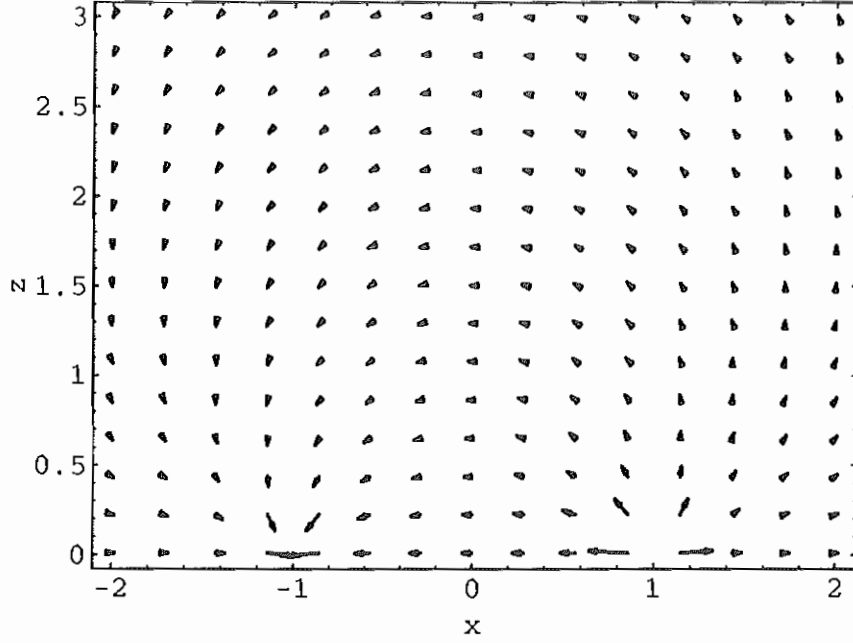


Figure 4.5: The vector field of the current density  $(J_x^D, J_z^D)$  in the asymptotic limit ( $t \rightarrow \infty$ ). For simplicity,  $x_0 = 1$  has been chosen.

ing to this field is

$$J_x^D(x=0, z, t \rightarrow \infty) = -\frac{2}{\pi} \int_0^\infty d\xi \frac{\xi f(\xi)}{z^2 + \xi^2}. \quad (4.28)$$

Equation (4.26) gives the cross-field current in the plane  $x = 0$  when the delta function choice of  $f(\xi)$  is made.

If  $v_A \neq 0$  then taking  $\lim_{s \rightarrow 0} s \tilde{B}_y(x, z, s)$  using Equation (4.15) gives

$$\lim_{t \rightarrow \infty} B_y(x, z, t) = f(x), \quad (4.29)$$

implying

$$\lim_{t \rightarrow \infty} J_x(x, z, t) = 0 \quad (4.30)$$

and

$$\lim_{t \rightarrow \infty} J_z = f(x). \quad (4.31)$$

Equations (4.30) and (4.31) imply that, for non-zero Alfvén speed, there are no cross-field currents in the model photosphere in the static limit. The physical interpretation of this result is that whenever the Alfvén speed is non-zero, a cross-field current density  $\mathbf{J}_\perp$  implies a force density  $\mathbf{J}_\perp \times \mathbf{B}$  which launches an

Alfvén wave to propagate the stress away. So in the static limit in any layer of the atmosphere, the cross-field current density must be zero. Zero Alfvén speed corresponds to an unmagnetised plasma, or an infinitely dense plasma. In either case, Alfvén waves cannot propagate to remove the stress implied by a cross-field current density.

Two other limits are of physical interest and are mentioned briefly here. The first is that of zero conductivity,  $\gamma \rightarrow 0$ . In this limit the  $v_A = 0$  steady state (Equation (4.27)) is achieved immediately at  $t = 0$ , because the diffusive timescale  $\gamma t^2$  is zero. Similarly, in the limit of infinite Alfvén speed ( $v_A \rightarrow \infty$ ), the  $v_A \neq 0$  steady state, i.e. Equation (4.29) is achieved instantly because the Alfvén timescale is zero in this limit.

#### 4.4.4 An approximation valid for large conductivity

Consider the specific choice for  $f(x)$  defined by Equation (4.13). In the limit of infinite conductivity, the cross-field current in the plane  $x = 0$  is  $J_x^P(x = 0, z, t)$ , given by Equation (4.22). This expression is independent of  $x_0$  (in contrast, for example with the corresponding expression when  $v_A = 0$ , Equation (4.26)). This suggests that for large but finite  $\gamma$ ,  $J_x(x = 0, z, t)$  does not depend strongly on the choice of  $x_0$ . Taking the limit  $x_0 \rightarrow \infty$  in Equation (4.15) allows the integral to be performed (Gradshteyn and Ryzhik, 1980), with the result

$$\tilde{B}_y(x = 0, z, s) = -\frac{\mu_0 I_0}{s} \exp \left[ -\frac{\gamma^{\frac{1}{2}} s z}{(s + \gamma v_A^2)^{\frac{1}{2}}} \right]. \quad (4.32)$$

The cross-field current implied by this magnetic field is

$$\tilde{J}_x(x = 0, z, s) = -\frac{\gamma^{\frac{1}{2}} I_0}{(s + \gamma v_A^2)^{\frac{1}{2}}} \exp \left[ -\frac{\gamma^{\frac{1}{2}} s z}{(s + \gamma v_A^2)^{\frac{1}{2}}} \right]. \quad (4.33)$$

Even these simpler forms cannot be analytically inverted, except in the limit  $\gamma \rightarrow \infty$  and at  $z = 0$ , when for example the cross-field current density becomes

$$J_x(x = 0, z = 0, t) = -I_0 \left( \frac{\gamma}{\pi t} \right)^{\frac{1}{2}} \exp \left( -\gamma v_A^2 t \right). \quad (4.34)$$

This expression shows that there is no significant current density in the photospheric boundary in this limit for large time.



## 4.5 The general case

In the general case, Equation (4.15) must be inverted numerically, since expansions in  $\gamma$  and  $v_A$  about the limits previously considered (§§4.1–4.3) are not possible. It is appropriate at this point to discuss a formal scaling procedure.

By introducing the scaled variables

$$\bar{t} = t/\tau, \quad \bar{z} = z/l, \quad \bar{x} = x/l, \quad \bar{B}_y = B_y/B_0, \quad (4.35)$$

where  $\tau$  and  $l$  are as yet undefined scale parameters, Equation (4.6) becomes

$$\frac{\partial^2 \bar{B}_y}{\partial \bar{t}^2} - c_P \frac{\partial^2 \bar{B}_y}{\partial \bar{z}^2} - c_D \frac{\partial}{\partial \bar{t}} \left( \frac{\partial^2 \bar{B}_y}{\partial \bar{x}^2} + \frac{\partial^2 \bar{B}_y}{\partial \bar{z}^2} \right) = 0. \quad (4.36)$$

Here the coefficients are

$$c_P = \frac{v_A^2 \tau^2}{l^2} \quad \text{and} \quad c_D = \frac{\tau}{\gamma l^2}. \quad (4.37)$$

The relative sizes of  $c_P$  and  $c_D$  determine whether Equation (4.6) behaves like the wave equation or the diffusion equation. In particular, the ratio  $c_P/c_D$  determines the qualitative behaviour. Taking (without loss of generality)  $\tau$  equal to the Alfvén transit time for the characteristic length  $l$  gives  $c_P = 1$  and  $c_D = 1/\gamma v_A l$ , so the ratio of coefficients is

$$\frac{c_P}{c_D} = \gamma v_A l = R_M, \quad (4.38)$$

where  $R_M$  is the magnetic Reynolds number of the subphotosphere. It is informative to write  $R_M = R_A/R$ , where  $R_A = \mu_0 v_A$  is the Alfvénic impedance and  $R = 1/\sigma_P l$  is the resistance corresponding to the conductivity  $\sigma_P$ . This shows that the behaviour of the model depends only on the ratio  $R_A/R$ .

The delta function choice of  $f(x)$  is adopted in this section. The current density is scaled so that  $\bar{J}_i = J_i/(I_0/l)$  and also the distance  $x_0$  is taken to be  $l$  for simplicity.

Davies (1978) provides the method for numerical inversion of the Laplace transform used here. A general discussion of approximate methods for inverting Laplace transforms, including Davies' can be found in Cheng *et al.* (1994). The quantity to be inverted is

$$\mathcal{L} [\bar{J}_x(\bar{x} = 0, \bar{z}, \bar{t})] = \frac{2\bar{\alpha}}{\pi} \left( \frac{R_M}{s} \right)^{\frac{1}{2}} \int_0^1 d\xi \frac{\partial}{\partial \bar{z}} \bar{z} \frac{K_1 \left\{ [R_M s (\bar{\alpha}^2 \bar{z}^2 + \xi^2)]^{\frac{1}{2}} \right\}}{(\bar{\alpha}^2 \bar{z}^2 + \xi^2)^{\frac{1}{2}}}, \quad (4.39)$$

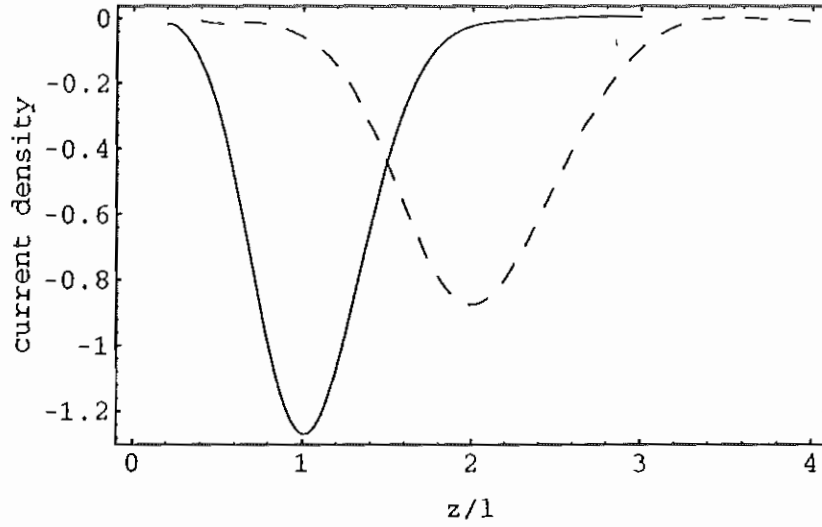


Figure 4.6:  $J_x(x = 0, z, t)/(I_0/l)$  for the case  $R_M = 10$  when  $\bar{t} = 1$  (solid curve) and  $\bar{t} = 2$  (dashed curve), i.e. at one and two Alfvén transit times. The propagating term of Equation (4.6) is dominant in this case.

where

$$\bar{\alpha} = \frac{s}{s + R_M}. \quad (4.40)$$

Figure 4.6 is a plot of the cross-field current density at one and two Alfvén transit times when  $R_M = 10$ . The perpendicular current propagates as a spreading pulse symmetrically around  $z = v_A t$ . This example is close to the propagating, or infinite conductivity limit of §4.4.1. It can also be used to test the large conductivity approximation presented in §4.4.4. Figure 4.7 is a plot of the numerical approximation to Equation (4.39) together with the approximate inverse of Equation (4.15) for the case  $R_M = 10$  at one Alfvén transit time. The large conductivity approximation is shown to be an excellent approximation for this value of  $R_M$ .

The second example considered is the intermediate case  $R_M = 1$ , where both the propagating and diffusive terms of the Equation (4.6) are influential. Figure 4.8 shows that a peak in current density propagates but lags behind  $z = v_A t$ , and the behaviour has more in common with the diffusive limit of §4.4.2 than the previous example.

Figure 4.9 is for  $R_M = 1/10$ , close to the diffusive limit of §4.4.2. Current closure occurs in the first few characteristic lengths below the photosphere for many Alfvén transit times. For times less than an Alfvén transit time, but greater

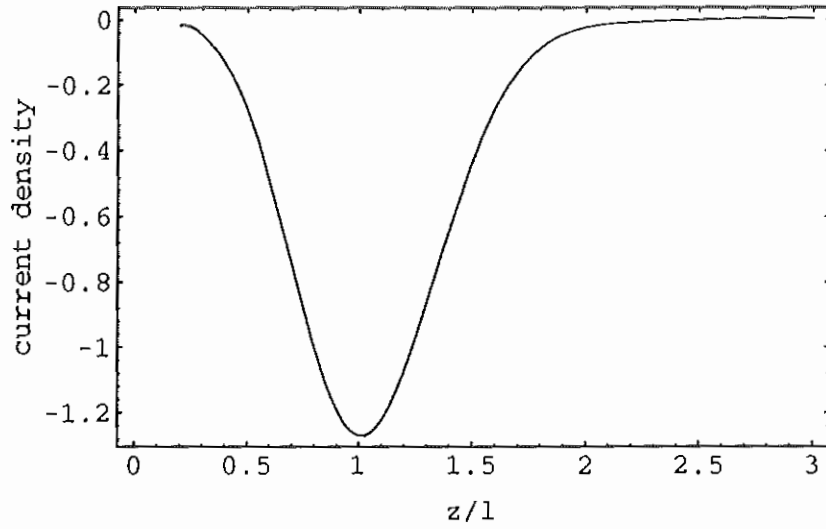


Figure 4.7: The cross-field current density  $J_x(x = 0, z, t)/(I_0/l)$  for the case  $R_M = 10$  at  $\bar{t} = 1$  calculated using the approximate (large conductivity) expression Equation (4.33), and also the 'exact' expression Equation (4.15). The current density derived from the exact expression is shown as a solid curve and that derived from the approximate expression as a dashed curve, although they agree almost to within the thickness of the line.

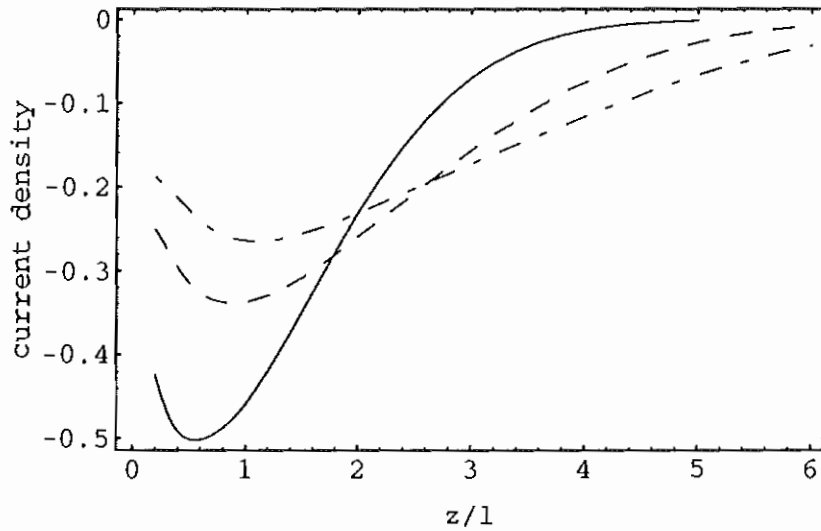


Figure 4.8:  $J_x(x = 0, z, t)/(I_0/l)$  for the case  $R_M = 1$  at one (solid curve), two (dashed curve) and three (dot-dashed curve) Alfvén transit times.

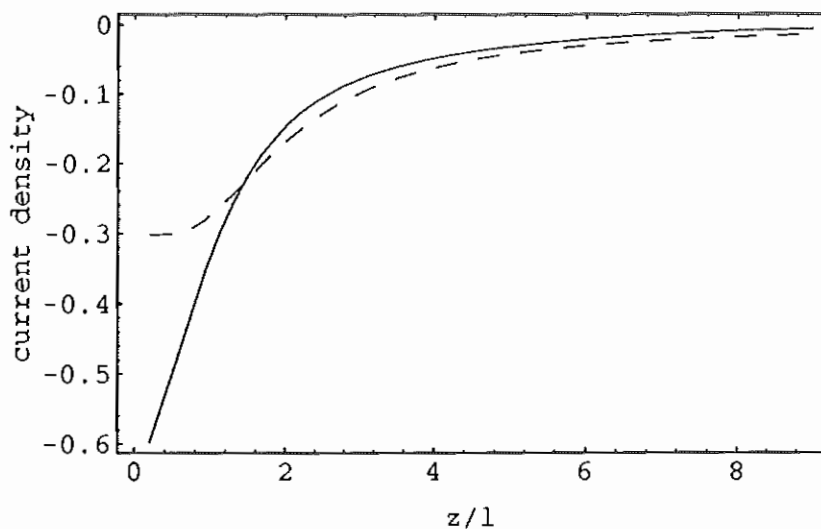


Figure 4.9: Scaled current density  $J_x(x = 0, z, t)/(I_0/l)$  in the photosphere at one (solid curve) and twenty (dashed curve) Alfvén times for the case  $R_M = 0.1$ . The diffusive term of equation (6) is dominant in this instance.

than the diffusive timescale, the asymptotic diffusive behaviour of Equation (4.26) is established ahead of  $z = v_A t$ .

In Figure 4.10, the fraction of current closing in the first characteristic length below the photosphere,  $I_\perp(l, \bar{t})$ , is shown, at two and four Alfvén transit times ( $\bar{t} = 2, 4$  respectively) as a function of the magnetic Reynolds number  $R_M = R_A/R$ . The quantity  $I_\perp$  is defined by Equation (4.17) above. For small  $R_M$ , the behaviour is diffusive and substantial cross-field closure occurs just below the photospheric boundary. (It follows from Equation (4.24) that the value  $1/2$  is expected when  $R_M = 0$ , as seen in the figure.) For large  $R_M$  the behaviour is propagating and after several Alfvén times there is no appreciable current closing in the region of interest.

The typical solar value taken here is  $R_A/R \approx 10^8/v_A$ , where  $v_A$  is in kilometres per second, corresponding to a characteristic length  $\approx 1$  Mm (Khan 1989). For reasonable values of the photospheric Alfvén speed, this implies a behaviour close to the infinite conductivity limit of §4.4.1. Imposed currents which turn on in the photosphere close at an Alfvénic front propagating into the subphotosphere, with only weak diffusion of cross-field current density about  $z = v_A t$ .

For solar parameters ( $R_A/R \approx 10^8$ ), Equation (4.17) (see also Figure 4.10) implies that after two Alfvén transit times, the fraction of current closing in the

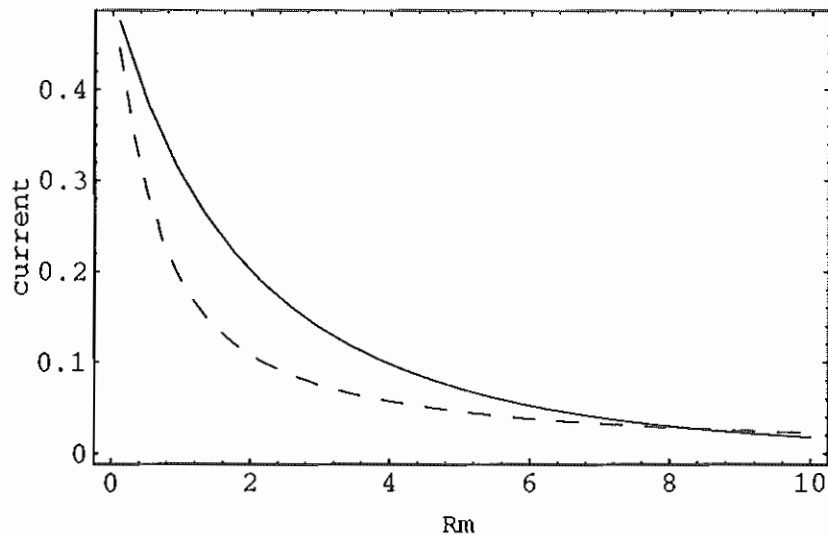


Figure 4.10: The fraction of the total current  $I_0$  closing in the first characteristic length  $l$  below the photospheric boundary as a function of the magnetic Reynolds number  $R_M$  at two (solid curve) and four (dashed curve) Alfvén transit times of  $l$ .

first characteristic length below the photospheric boundary is of order several percent. So the cross-field current has propagated out of the region of interest in a brief time.

## 4.6 Discussion

In the sections above, a simple model is formulated to describe the time-dependent response of the subphotospheric plasma to a current imposed from above. The main results may be summarised as follows:

1. Cross-field current closure in the photosphere is a dynamic process. The stress implied by a cross-field current density  $\mathbf{J}_\perp$  is propagated away by Alfvén waves.
2. In the static limit, currents imposed along field lines at the photospheric boundary flow along field lines below the photosphere.
3. The time evolution of cross-field current closure in the model depends only on the magnetic Reynolds number  $R_M$ , which may be written as the ratio  $R_M = R_A/R$ , where  $R_A = \mu_0 v_A$  is the Alfvénic impedance and  $R = 1/\sigma_P l$

is the resistance corresponding to the conductivity  $\sigma_P$  and the characteristic length  $l$ . For  $R_M \gg 1$ , current closure occurs at an Alfvénic front propagating into the photosphere, with only weak diffusion about the front. For  $R_M \ll 1$ , current closure is a diffusive process, with cross-field currents flowing just below the photosphere for many Alfvén times.

4. Solar parameters imply  $R_M \gg 1$ . So after several Alfvén times, current closure occurs deep in the photosphere.

These results imply that the line-tying assumption is valid only on a timescale of order the Alfvén transit time of a given layer of the subphotosphere. Models of coronal magnetic structures based on line-tying at the photosphere need to be reconsidered in this light.

## 4.7 Line-tying revisited

The model presented in §§4.3–4.5 above assumes a prescribed current density appears in the photospheric boundary at a particular time. A weakness of the model is that it does not describe how that current density is produced, or arrives at the photospheric boundary. Implicitly, the cross-field current density which closes the imposed current density must propagate from above, along field lines to the photosphere. This is relevant to describe the process of ‘shearing’ a coronal magnetic arcade — introduced in §4.1 above — for example. Assuming the region above the photosphere is perfectly conducting, the cross-field closure of the current before it arrives at the photosphere must occur in a propagating Alfvénic front. Behind that front, plasma is set into motion. Equivalently, the passage of the front establishes an electric field. The current density that appears in the boundary is the result of the reflection of the electric field of the incident front from the photospheric boundary. In this section the existing model is modified to describe the arrival of such a front, and its reflection from the photospheric boundary. The line-tying boundary condition is tested by the model, and found to be an inaccurate description of the behaviour of fields and plasma at the photospheric boundary.

### 4.7.1 A reflection coefficient for the photosphere

For simplicity, the corona-chromosphere/photosphere transition is modelled by two adjacent, uniform regions with an abrupt change in density and conductivity at the boundary. The corona is described by region '1', a perfectly conducting fluid occupying  $z < 0$  with Alfvén speed  $v_{A1}$ . The chromosphere/subphotosphere is modelled by region '2' ( $z > 0$ ), where the conductivity has the finite value  $\sigma_P$  and the Alfvén speed has the value  $v_{A2}$  ( $v_{A2} \ll v_{A1}$ ). Hereafter, for simplicity region '2' is referred to as the subphotosphere. Both regions are assumed to be threaded by a uniform background magnetic field of magnitude  $B_0$  in the  $z$ -direction. A one-dimensional model for the reflection of a perturbation incident on the  $z = 0$  boundary from  $z < 0$  is considered, in which  $\partial/\partial x = \partial/\partial y = 0$ . Assuming transverse, incompressible perturbations of the model atmosphere, the velocity  $v_y^{(2)}(z, t)$  in the subphotosphere satisfies the partial differential equation

$$\frac{\partial^2 v_y^{(2)}}{\partial t^2} - v_{A2}^2 \frac{\partial^2 v_y^{(2)}}{\partial z^2} - \frac{1}{\gamma} \frac{\partial^3 v_y^{(2)}}{\partial t \partial z^2} = 0, \quad (4.41)$$

where  $\gamma = \mu_0 \sigma_P$ . In the coronal region, the velocity is  $v_y^{(1)}(z, t)$ , which satisfies the wave equation  $\partial^2 v_y^{(1)}/\partial t^2 - v_{A1}^2 \partial^2 v_y^{(1)}/\partial z^2 = 0$ .

The Laplace transform of the solution to Equation (4.41), subject to the initial conditions

$$v_y^{(2)}(z, t = 0) = \left. \frac{\partial v_y^{(2)}}{\partial t} \right|_{t=0} = 0, \quad (4.42)$$

and assuming the velocity perturbations are bounded at infinity, is

$$\tilde{v}_y^{(2)}(z, s) = \frac{A'(s)}{s} \exp[-a(s)z], \quad (4.43)$$

where  $a^2 = \gamma s \alpha_2^2$  and  $\alpha_2^2 = s/(s + \gamma v_{A2}^2)$ . Equation (4.43) does not correspond to a tabulated Laplace transform.

The question to be resolved is the response of the system to the arrival of a velocity disturbance originating in the corona. For simplicity, assume that an Alfvénic front propagates towards  $z = 0$ , carrying behind it a constant velocity  $v_0$ , so that the front arrives at the origin at  $t = 0$ . (This is appropriate if, for instance, the coronal field lines are being driven at a constant velocity at  $z = -\infty$ , and the inertia of the coronal plasma is ignored.) Then the velocity of the plasma in  $z < 0$  following the arrival of the front at the photospheric boundary can be written

$$v_y^{(1)}(z, t) = v_0 + [g(t + z/v_{A1}) - v_0] \theta(t + z/v_{A1}), \quad (4.44)$$

where  $g(t + z/v_{A1})$  describes the reflection of the incident disturbance from the photospheric boundary. Laplace transforming Equation (4.44) gives

$$\check{v}_y^{(1)}(z, s) = v_0/s + [\check{g}(s) - v_0/s] \exp(sz/v_{A1}). \quad (4.45)$$

The magnetic fields corresponding to the (Laplace transformed) velocities (4.45) and (4.43) are obtained from the  $y$ -component of the momentum equation, Equation (4.92) in the Appendix, which is valid whether  $\sigma_P$  is finite or not. Laplace transforming Equation (4.92) gives

$$\frac{d\check{B}_y}{dz} = \frac{\mu_0 \rho}{B_0} [s\check{v}_y - v_y(z, t = 0)]. \quad (4.46)$$

Integrating this equation in regions '1' and '2' and determining the constants of integration by matching to the fields ahead of the front in each case, gives

$$\check{B}_y^{(1)}(z, s) = \frac{B_0}{v_{A1}} \{[\check{g}(s) - v_0/s] \exp(sz/v_{A1}) - v_0/s\} \quad (4.47)$$

and

$$\check{B}_y^{(2)}(z, s) = -\frac{A'(s) B_0}{a(s) v_{A2}^2} \exp[-a(s)z]. \quad (4.48)$$

Next we require continuity of  $v_y$  and  $B_y$  in the plane  $z = 0$  to relate the behaviour in the two regions. Setting Equations (4.45) and (4.43) equal at  $z = 0$  and Equations (4.47) and (4.48) equal at  $z = 0$  gives two equations for  $\check{g}(s)$  and  $A'(s)$  which may be solved to give

$$\check{g}(s) = \frac{2v_0}{s[1 + v_{A1}/a(s)v_{A2}^2]}, \quad (4.49)$$

and

$$A'(s) = \check{g}(s) s. \quad (4.50)$$

Equation (4.49) corresponds to a tabulated Laplace transform and so may be inverted (e.g. Erdélyi *et al.* 1954) to give  $g(t) = v_0[R(t) + 1]$ , where

$$R(t) = \frac{2}{v_{A2}^2 - v_{A1}^2} \left\{ (v_{A2}^2 + v_{A1}^2)/2 - v_{A1} v_{A2} \operatorname{erf} \left[ (\gamma v_{A2}^2 t)^{\frac{1}{2}} \right] - v_{A2}^2 \exp \left[ -v_{A2}^2 \left( 1 - v_{A2}^2/v_{A1}^2 \right) \gamma t \right] \operatorname{erfc} \left[ \frac{v_{A2}}{v_{A1}} (\gamma v_{A2}^2 t)^{\frac{1}{2}} \right] \right\}. \quad (4.51)$$

Here  $\operatorname{erf}(x)$  and  $\operatorname{erfc}(x)$  refer to the error function and its complement respectively (Abramowitz and Stegun, 1965).



Some insight into Equation (4.51) is provided by considering limiting cases. First, consider the limit of a perfectly conducting subphotosphere. Then,

$$\lim_{\gamma \rightarrow \infty} R(t) = \frac{v_{A2} - v_{A1}}{v_{A2} + v_{A1}}, \quad (4.52)$$

which is recognisable as the reflection coefficient for Alfvén waves encountering a density step, and may be denoted  $\alpha_{12}$  (see chapter 2). Perfect reflection occurs in the limit  $v_{A2} \ll v_{A1}$ , when  $g = 0$ . Equation (4.52) allows the identification of  $R(t)$  as a generalised, time-dependent reflection coefficient for our model. Irrespective of conductivity, perfect reflection ( $R = -1$ ) is obtained in the limit  $v_{A2} \rightarrow 0$ , i.e. when the model subphotosphere is infinitely dense.

Equation (4.51) can also be better understood if it is appropriately scaled. Introducing the scaled parameters

$$\bar{t} = t/(l/v_{A2}), \quad \bar{z} = z/l, \quad \text{and} \quad \bar{v}_y = v_y/v_0, \quad (4.53)$$

where  $l$  is some characteristic length, we obtain the dimensionless form

$$R(\bar{t}) = \frac{2}{1-r^2} \left\{ (1+r^2)/2 - r \operatorname{erf} \left[ (R_M \bar{t})^{\frac{1}{2}} \right] - \exp \left[ - (1-r^{-2}) R_M \bar{t} \right] \operatorname{erfc} \left[ (R_M \bar{t})^{\frac{1}{2}} / r \right] \right\}, \quad (4.54)$$

where

$$r = v_{A1}/v_{A2} \quad \text{and} \quad R_M = \gamma v_{A2} l. \quad (4.55)$$

The variable  $R_M$  is the magnetic Reynolds number of the model subphotosphere. Figure 4.11 shows the value of  $R(\bar{t})$  for  $r = 10$  and two values of  $R_M$ .

The behaviour of Equation (4.54) in the limits of small and large arguments of the error functions is given by

$$R(\bar{t}) \approx \begin{cases} -1 + 4(R_M \bar{t})^{\frac{1}{2}} / \pi^{\frac{1}{2}} r & \text{if } \bar{t} \ll R_M^{-1}, \\ (1-r)/(1+r) & \text{if } \bar{t} \gg R_M^{-1}. \end{cases} \quad (4.56)$$

Consequently, at small times the interface is almost perfectly reflecting, but at large times approaches the infinite conductivity value  $\alpha_{12} = (1-r)/(1+r)$ . This behaviour can be clearly seen in Figure 4.11. The behaviour for large and small times may be understood as follows. The reflection coefficient depends only on the velocity of the subphotosphere close to the boundary  $z = 0$ . If the subphotosphere is infinitely conducting, the subphotosphere close to the boundary is almost instantaneously set into motion behind a propagating front.

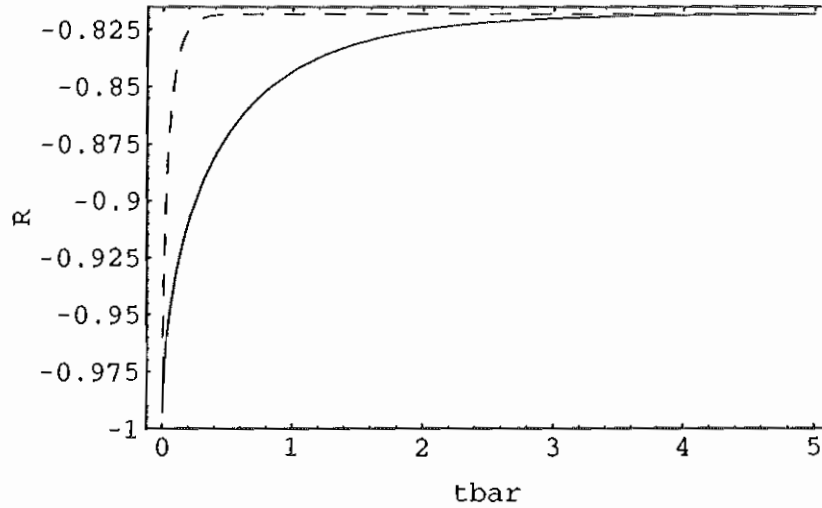


Figure 4.11: The generalised reflection coefficient  $R(\bar{t})$  for  $r = 10$  and  $R_M = 1$  (solid) and  $R_M = 10$  (dashed) as a function of time. For small times the reflection is almost perfect, but at large times  $R$  approaches the infinite conductivity value  $\alpha_{12}$  (see below).

The reflection coefficient  $\alpha_{12}$  is obtained as a result. If the subphotosphere is finitely conducting, the plasma in the subphotosphere close to  $z = 0$  is set into motion over a longer timescale as diffusive processes occur. Consequently, for times  $\bar{t} \ll R_M^{-1}$ , reflection is almost perfect. Figure 4.12 shows the velocity of the subphotosphere as it is set into motion. This figure was calculated from Equation (4.43) using Equations (4.49) and (4.50) and the numerical Laplace inversion procedure discussed in §4.5.

As explained above, for solar parameters  $R_M \gg 1$  and so this model suggests that it is appropriate to treat the subphotosphere as perfectly conducting when considering the reflection of fronts incident from above. Incidentally, this model justifies the neglect of the finite conductivity of the subphotosphere in the model for energy transfer in a solar flare presented in chapter 2.

#### 4.7.2 Comparison with the Earth's magnetosphere

The generalised reflection coefficient (4.54) may be compared with the predictions of a boundary condition on plasma and fields often invoked to describe the reflection of an Alfvénic front from the Earth's magnetosphere-ionosphere boundary (e.g. Goertz and Boswell, 1979; Scholer, 1970). The magnetosphere is modelled as

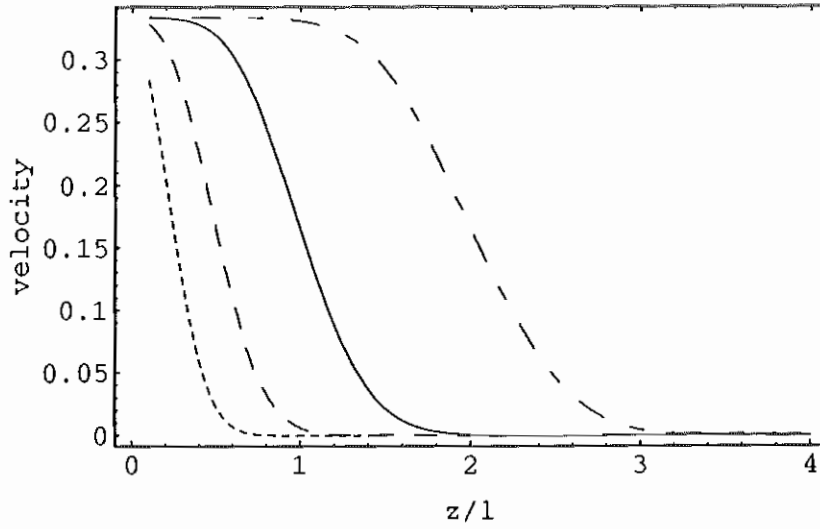


Figure 4.12: The velocity of the impinged medium,  $v_y^{(2)}$  in the case  $R_M = 10$ ,  $r = 5$  as a function of  $z/l$  at one quarter (small dashes), one half (dashed), one (solid) and two (dot-dash) Alfvén transit times of the characteristic length  $l$ . The expected value in the limit of large time is one third.

an infinitely conducting medium and the ionosphere is an adjacent thin, finitely conducting region. If no motion is induced in the ionosphere by the incident front, and that there is no transmission of the front through the ionosphere, Ampere and Faraday's Maxwell equations imply the boundary condition on the electric field  $E_x$  at the magnetosphere-ionosphere boundary ( $z = 0$ ):

$$\left[ \frac{\partial E_x}{\partial z} + \mu_0 \Sigma_P \frac{\partial E_x}{\partial t} \right]_{z=0} = 0. \quad (4.57)$$

Here  $\Sigma_P$  is the height integrated Pederson conductivity of the ionosphere, from  $z = 0$  to a depth where the field  $B_y$  is assumed to be zero, owing to the non-transmission through the lower region. The non-transmission argument relies on the ionosphere being thin and bounded below by a non-conducting medium (the atmosphere), in which Alfvén waves cannot propagate.

The boundary condition (4.57) may be used as follows. Consider the electric field of an incident ('i') and reflected ('r') wave in the magnetosphere:  $E_x = f_i(t - z/v_A) + f_r(t + z/v_A)$ . Applying the boundary condition Equation (4.57) gives

$$f_r = \frac{1 - R_M}{1 + R_M} f_i, \quad (4.58)$$

where  $R_M$  is the magnetic Reynolds number of the ionosphere.

Two limits of Equation (4.58) have simple interpretations. When  $R_M \gg 1$ ,  $f_r = -f_i$ , implying perfect reflection. Then  $E_x$  is zero at the boundary, i.e. the boundary is behaving as a perfectly conducting metallic plate. This is perfect line-tying. At the other extreme, when  $R_M \ll 1$ , twice the incident amplitude is produced at the boundary. This is the *free end* boundary condition. Physically, the ionosphere is an insulator in this limit and so the field lines have no identity there: the magnetospheric field lines can move without restriction in the plane of the boundary.

As explained above,  $R_M \gg 1$  is the appropriate limit for the solar photosphere, and so a naive application of the boundary condition (4.57) implies perfect reflection for an Alfvénic front incident on the photosphere from above, independent of the density step at  $z = 0$ . The reason for the discrepancy between this prediction and the result implied by Equation (4.54) is that the assumptions adopted in deriving Equation (4.57), whilst appropriate to the magnetosphere-ionospheric boundary, are inappropriate for the photospheric boundary. Alfvénic fronts incident on the photosphere can propagate into the subphotosphere, setting it into motion in the process. The solar atmosphere is not a thin layer, bounded below by a non-conducting region.

## 4.8 Modelling the shearing of an arcade

The models developed above imply that the line-tying boundary condition is not appropriate to describe the ‘shearing’ of a coronal magnetic arcade (see §4.1 above). In the following section a simple model is developed to describe the evolution of a coronal arcade subject to a shearing velocity flow at one row of footpoints. The model is consistent with the results summarised in §4.6 above, and is similar to the model for energy propagation into a solar flare presented in chapter 2. In common with that model it does not describe the coronal part of the arcade as force-free, which is a requirement of any realistic model. This limitation does not affect the qualitative results presented here however.

### 4.8.1 A two-dimensional model

The coronal arcade is modelled here as a two-dimensional structure ( $\partial/\partial y = 0$ ) in which a background field  $\mathbf{B} = B_0 \hat{\mathbf{z}}$  joins two ‘subphotospheric regions’ ( $z < 0$  and  $z > l$ ) via a coronal section. It is assumed that there is only weak variation in the magnetic structure of the arcade in the direction of the axis of the arcade. Figure 4.13 illustrates the reasoning behind this geometry.

The arcade is assumed to be subject to a shearing velocity in the plane  $z = 0$  and the evolution of the system is determined. The shearing velocity is assumed to be of the form

$$v_y(x, z = 0, t) = v_0 \varphi(x) \theta(t), \quad (4.59)$$

where  $\varphi(x)$  is an even function in  $x$ . We also assume that  $\varphi(0) = 1$  and  $\varphi(\infty) = 0$ . The simplest choice of  $\varphi$  is

$$\varphi(x) = \begin{cases} 1 & \text{if } |x| < x_0, \\ 0 & \text{otherwise,} \end{cases} \quad (4.60)$$

where  $x_0$  defines the width of the shearing velocity field in  $x$ . For the simple geometry of this model and assuming infinite conductivity in the coronal portion of the arcade, the velocity of the arcade for times less than  $\tau_A = l/v_{A1}$  (where  $v_{A1}$  is the coronal Alfvén speed) is

$$v_y(x, z, t) = v_0 \varphi(x) \theta(t - z/v_{A1}). \quad (4.61)$$

That is to say the coronal part of the arcade is set into motion with speed  $v_0$  behind a propagating Alfvénic front. The magnetic field corresponding to Equation (4.61) can be found from the  $y$ -component of the momentum equation, (Equation (4.92) in the Appendix) to be

$$B_y(x, z, t) = -\frac{B_0 v_0}{v_{A1}} \varphi(x) \theta(t - z/v_{A1}). \quad (4.62)$$

The current densities corresponding to this magnetic field are

$$J_x(x, z, t) = -\frac{B_0 v_0}{\mu_0 v_{A1}^2} \varphi(x) \delta(t - z/v_{A1}), \quad (4.63)$$

and

$$J_z(x, z, t) = -\frac{B_0 v_0}{\mu_0 v_{A1}} \frac{d\varphi}{dx} \theta(t - z/v_{A1}). \quad (4.64)$$

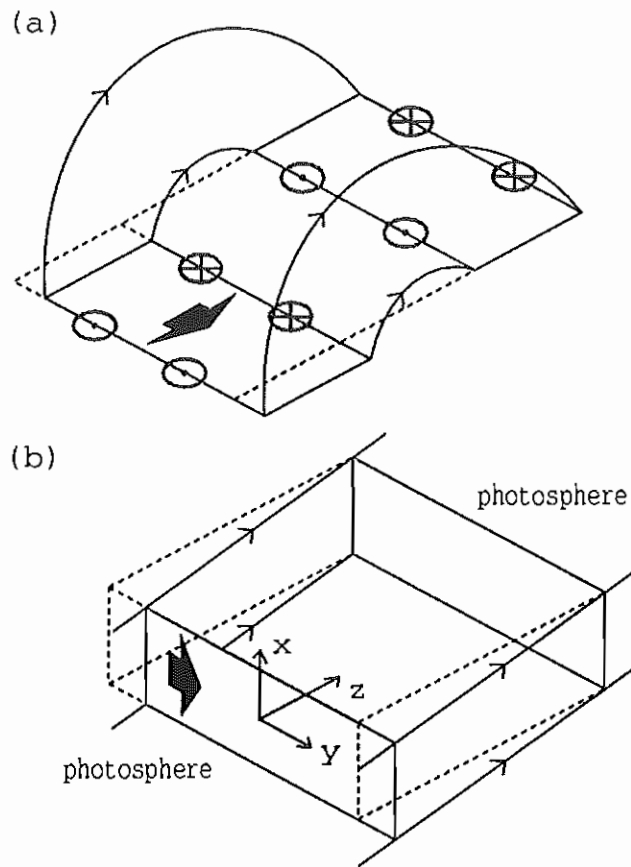


Figure 4.13: The geometry of a coronal magnetic arcade is shown in (a). The arcade is subject to a shearing velocity flow (dark arrow) at one row of footpoints, which establishes the current system shown. The simple two-dimensional model for the shearing process developed here is shown in (b). No variation is permitted in the direction of the axis of the arcade (the  $y$ -direction), and the curvature of the magnetic field (shown by the arrowed lines) is neglected. The current system in (b) has been omitted for clarity.

If a total current  $I_0$  flows in the circuit established by the passage of the front, i.e.  $I_0 \equiv \int_0^\infty J_z(x, z < v_{A1}t, t) dx$ , we have that

$$I_0 = \frac{B_0 v_0}{\mu_0 v_{A1}}. \quad (4.65)$$

The electric field associated with the passage of the front is  $E_x = -v_y B_0$ . This implies a  $z$  component to the Poynting flux  $S_z = E_x B_y / \mu_0$ . Integrating over  $x$  gives the power the Poynting flux supplies to the advancing front:

$$P_S = 2R_{A1} I_0^2 \int_0^\infty dx \varphi(x)^2, \quad (4.66)$$

where  $R_{A1} = \mu_0 v_{A1}$  is the Alfvénic impedance of the coronal part of the arcade. The driven footpoint at  $z = 0$  acts as an ideal MHD generator, supplying energy at a constant rate to the Alfvénic front. The rates at which energy goes into the component of magnetic field  $B_y$  and the bulk velocity  $v_y$  at the front, i.e.  $P_{\text{mag}}$  and  $P_{\text{kin}}$  respectively, may also be calculated, to give

$$P_{\text{mag}} = P_{\text{kin}} = \frac{1}{2} P_S. \quad (4.67)$$

Equation (4.67) implies two things about the energetics of the ‘shearing’ of this model arcade. First, the statement of energy conservation (i.e. the Poynting theorem) for the system has the simple form  $P_S = P_{\text{kin}} + P_{\text{mag}}$ . Second, the passage of the front involves equipartition of energy between the kinetic and magnetic components  $P_{\text{kin}}$  and  $P_{\text{mag}}$ .

The system evolves through repeated reflections of the Alfvénic front from the photospheric boundaries,  $z = l$  and  $z = 0$ . The subphotospheric regions are treated as infinitely conducting regions with a lower Alfvén speed  $v_{A2}$ , following the conclusions of the models presented above. The boundary conditions imposed are Equation (4.59) at  $z = 0$  and continuity of  $E_x$  and  $B_y$  in the photospheric boundary  $z = l$  behind fronts.

Consider the system just after  $2k$  reflections of the Alfvénic front. Denoting the magnetic fields ahead and behind the front by  $b_{2k-1}\varphi(x)$  and  $b_{2k}\varphi(x)$  respectively, and the corresponding velocities by  $v_{2k-1}\varphi(x)$  and  $v_{2k}\varphi(x)$ , the boundary conditions described above imply the relations

$$b_{2k} - b_{2k-1} = -\frac{B_0}{v_{A1}}(v_{2k} - v_{2k-1}), \quad (4.68)$$

and

$$v_{2k} = v_0. \quad (4.69)$$

Similarly, considering the system after  $2k + 1$  reflections and applying the boundary conditions at  $z = l$  implies the pair of relations

$$b_{2k+1} - b_{2k} = \frac{B_0}{v_{A1}}(v_{2k+1} - v_{2k}), \quad (4.70)$$

and

$$b_{2k+1} - b_{2k-1} = -\frac{B_0}{v_{A2}}(v_{2k+1} - v_{2k-1}). \quad (4.71)$$

Equations (4.68), (4.69), (4.70) and (4.71) may be combined to give

$$b_{2k+2} - b_{2k+1} = b_{2k+1} - b_{2k} = -\alpha_{12}(b_{2k} - b_{2k-1}). \quad (4.72)$$

This Equation may be applied iteratively to obtain the evolution of the magnetic field;

$$b_{2k} = b_0 \left[ 1 - 2\alpha_{12} \frac{1 - (-\alpha_{12})^k}{1 + \alpha_{12}} \right]. \quad (4.73)$$

Equation (4.72) implies that  $b_{2k+1} = (b_{2k} + b_{2k+2})/2$ . Returning to Equation (4.70), the velocity in the arcade evolves according to

$$v_{2k+1} = v_0 \left[ 1 - (-\alpha_{12})^{k+1} \right]. \quad (4.74)$$

Assuming  $\alpha_{12} \neq -1$ , Equation (4.74) describes how the entire arcade — and in particular the passive footpoint — is set into motion as momentum is transferred across from the driving footpoint. Equilibrium is achieved when the whole arcade is moving with the asymptotic velocity  $v_\infty = v_0$ . The current flowing in the arcade following each successive reflection of a front is given by

$$I_i = -b_i/\mu_0, \quad (4.75)$$

so using Equation (4.73) the asymptotic value of current is

$$I_\infty = -\frac{R_{A1}}{\mu_0 R_{A2}} I_0. \quad (4.76)$$

A non-zero final current flows in the arcade because in the time required to transfer momentum from the driving to the passive footpoint — to bring it up to speed  $v_0$  — the driving footpoint is displaced more than the passive footpoint. Hence the whole arcade is sheared (i.e. does not have its magnetic field perpendicular to the neutral line) in the asymptotic limit, implying a non-zero current, viz.  $I_\infty$ . The final shear of the arcade is defined by

$$\theta_\infty = \tan^{-1}(b_\infty/B_0) = \tan^{-1}(v_0/v_{A2}). \quad (4.77)$$



An important special case is the limit of line-tied behaviour, i.e. when the subphotospheric medium is a perfect reflector of the incident fronts,  $\alpha_{12} = -1$ . Then  $v_{2k+1} = 0$  at each reflection from  $z = l$ , since the subphotosphere cannot be set into motion from above in this limit. The velocity being imposed at each reflection from  $z = 0$  is  $v_{2k} = v_0$  and so no equilibrium is possible here. As the driving and passive footpoints are successively displaced with each reflection, the current flowing in the arcade increases with each reflection. From Equations (4.73) and (4.75), in this case  $I_\infty = \infty$ . Presumably an ideal MHD instability or reconnection would begin above a critical value of the current, to allow relaxation of the system. This model is analogous to that of Haerendel (1980; 1983; 1987; 1988; 1990; 1994) for the stressing and relaxation of magnetospheric magnetic field lines. In Haerendel's model a 'fracture zone' or dissipative region is set up to relieve the stress associated with incompatible ideal MHD motions of a system of magnetospheric field lines.

If the equilibrium behaviour of the system is achieved only after many reflections of Alfvénic fronts, it is relevant to discuss the characteristic secular timescale for the process described above. From Equation (4.74) it follows that the time taken for the velocity of the passive footpoint to reach a fraction  $f$  of the asymptotic value  $v_0$  is

$$t_f = \left[ \frac{\ln(1-f)^2}{\ln(-\alpha_{12})} - 1 \right] \tau_A, \quad (4.78)$$

where both logarithmic terms have fractional arguments and so are negative. If  $v_{A2} \ll v_{A1}$ ,  $-\alpha_{12} \approx 1 - 2R_{A2}/R_{A1}$  and the characteristic time becomes  $t_l \approx l/2v_{A2}$ . For typical solar values this time is a few hours, and so if one footpoint of a solar arcade is continuously driven, the passive footpoint is set into motion in about this time.

### 4.8.2 The role of the subphotosphere

The model developed in the previous section assumes a driving velocity  $v_0$  is maintained at the row of footpoints  $z = 0$  for all time. A more realistic boundary condition is to assume that a layer of finite depth in the subphotosphere is initially set into motion with velocity  $v_0$ , but then loses speed as its initial momentum is transferred into motion of the plasma behind fronts propagating away, both upwards (into the coronal portion of the arcade) and downwards (into the sub-

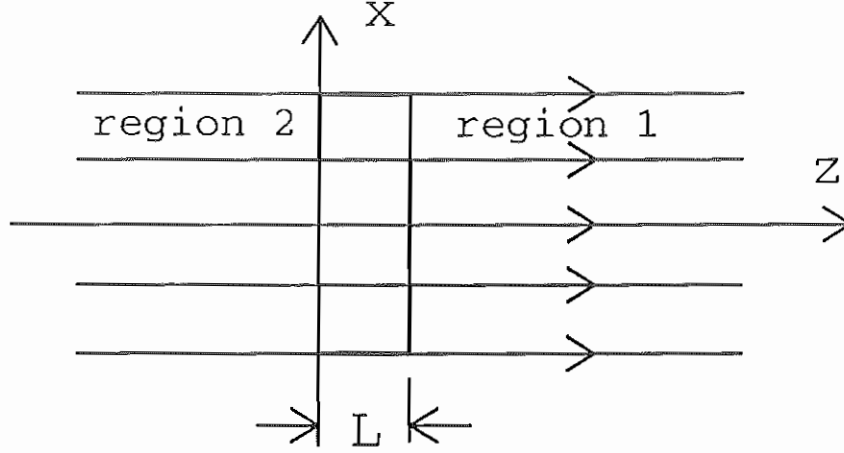


Figure 4.14: The shearing of the arcade is assumed here to be driven by a subphotospheric layer of thickness  $L$ . Region 1 is the subphotospheric part of the arcade and region 2 is the coronal part.

photospheric part). A simple two-dimensional model of this process is developed here.

For simplicity, assume that the driving layer is a thin layer, of thickness  $L$ . Here 'thin' implies that times of interest are longer than an Alfvén transit time of the layer. The layer is assumed to be the uppermost part of the subphotosphere, which is again assumed to have Alfvén speed  $v_{A2}$  and to occupy the region  $z > 0$ . The coronal part of the arcade ( $z < 0$ ) is assumed to have Alfvén speed  $v_{A1}$ . Figure 4.14 illustrates the arrangement.

The velocities in the coronal ('1') and subphotospheric ('2') parts of the arcade after  $t = 0$  may be written

$$v_y^{(1)}(x, z, t) = f(t + z/v_{A1}) \varphi(x), \quad (4.79)$$

and

$$v_y^{(2)}(x, z, t) = g(t - z/v_{A1} + L/v_{A2}) \varphi(x). \quad (4.80)$$

If the driving layer is thin, a single velocity,  $v_y^L$ , can be assumed for it, i.e.

$$v_y^L(x, t) = v_y^{(1)}(x, 0, t) = v_y^{(2)}(x, L, t). \quad (4.81)$$

Equations (4.80), (4.79) and (4.81) imply  $g(t) = f(t)$ . Physically, the amplitude of the outgoing disturbance in both directions is determined just by the velocity of the driving layer at a given time.

Using the  $y$ -component of the momentum equation (Equation (4.92) in the Appendix to this chapter), the magnetic fields corresponding to the velocities  $v_y^{(1)}$  and  $v_y^{(2)}$  are

$$B_y^{(1)}(x, z, t) = \frac{B_0}{v_{A1}} f(t + z/v_{A1}) \varphi(x), \quad (4.82)$$

and

$$B_y^{(2)}(x, z, t) = -\frac{B_0}{v_{A2}} f(t - z/v_{A1} + L/v_{A2}) \varphi(x). \quad (4.83)$$

In Equations (4.82) and (4.83) it is assumed that there is no  $y$ -component of magnetic field ahead of the propagating disturbance.

The complete description of the system requires the determination of  $f(t)$ . This may be achieved as follows. Integrating the  $y$ -component of the momentum equation (Equation (4.92) in the Appendix) over all  $x$  and over the thickness of the driving layer in  $z$ , we obtain

$$\rho_2 \frac{d}{dt} \int_0^\infty dx \int_0^L dz v_y^L(x, t) = \frac{B_0}{\mu_0} \int_0^\infty dx [B_y^{(2)}(x, L, t) - B_y^{(1)}(x, 0, t)]. \quad (4.84)$$

Substituting Equations (4.81), (4.82) and (4.83) into Equation (4.84) yields the differential equation for  $f(t)$ :

$$\frac{df}{dt} = -\frac{v_{A2}}{L} \left(1 + \frac{v_{A2}}{v_{A1}}\right) f \quad (4.85)$$

which implies that

$$f(t) = v_0 \exp \left[ -\frac{v_{A2}}{L} \left(1 + \frac{v_{A2}}{v_{A1}}\right) t \right], \quad (4.86)$$

where it has been assumed that  $v_y^L(x, 0) = v_0 \varphi(x)$ . Equation (4.86) describes how the driving layer is braked as it radiates momentum behind the outward propagating Alfvénic fronts. The two terms in the exponent of Equation (4.86) represent the subphotospheric (the first term) and the coronal (the second term) contributions to the braking. For  $v_{A2} \ll v_{A1}$ , the dominant contribution is from the Alfvénic front propagating into the subphotosphere. Then, the characteristic time for the braking of the driving layer is  $t_L \approx L/v_{A2}$ . The motion of the driving layer is brought to a halt in a time of order the Alfvén transit time of a subphotospheric layer of thickness the same as the driving layer. For solar values, the thickness of the driving layer is unknown, but this analysis suggests that the braking owing to Alfvénic fronts propagating downwards is an important effect. For example, for a driving layer of thickness  $10^4$  m, the layer is brought to rest in seconds.

The transfer of momentum behind the propagating fronts can be explicitly shown, as follows. From Equation (4.79), the  $y$ -component of momentum in the motion above the photosphere,  $M^{(1)}$ , increases at the rate

$$\frac{dM^{(1)}}{dt} = 2\rho_1 v_{A1} f(t) \int_0^\infty dx \varphi(x). \quad (4.87)$$

Similarly, from Equation (4.80), the rate at which the  $y$ -component of momentum increases in the region  $z > L$  is given by

$$\frac{dM^{(2)}}{dt} = 2\rho_2 v_{A2} f(t) \int_0^\infty dx \varphi(x). \quad (4.88)$$

Finally, defining  $M_L(t)$  as the momentum of the driving layer at time  $t$ , it is easy to show from Equation (4.81) that

$$\frac{dM_L}{dt} = 2\rho_2 L \frac{df(t)}{dt} \int_0^\infty dx \varphi(x). \quad (4.89)$$

Comparison of Equations (4.87), (4.88), (4.89) and Equation (4.85) shows that  $dM_L/dt = -(dM^{(1)}/dt + dM^{(2)}/dt)$ , i.e. momentum is conserved in the braking of the driving layer.

## 4.9 Conclusions

In this chapter, a two-dimensional model is developed to describe the dynamic response of the subphotosphere to a current density, imposed along field lines from the corona. The objective is to determine the conditions under which the current closes immediately below the photosphere, and those under which current closure occurs deep in the subphotosphere. The conclusion of the model (summarised in § 4.6) is that solar parameters imply that current closure occurs locally only for an Alfvén transit time of a given layer of the subphotosphere. In the static limit, currents flow along field lines through the photosphere.

This result is inconsistent with the assumptions about current closure implicit in the boundary condition of ‘line-tying’, often applied to describe the behaviour of magnetic fields at the photosphere. The line-tying assumption is tested in § 4.7 above by the construction of a model for the reflection of an incident Alfvénic front from the photosphere. The model shows that the subphotosphere may be treated as an infinitely conducting medium of greater density for this purpose.

In § 4.8, a model is presented to describe the shearing of a coronal magnetic arcade by a velocity imposed at one row of footpoints. The model is consistent

with the conclusions of § 4.6 and § 4.7. The model implies that momentum transfer occurs between rows of footpoints of the arcade so that the passive row of footpoints is set into motion, with a characteristic time  $t_l = l/2v_{A2}$ , where  $l$  is the length of the arcade, and  $v_{A2}$  is the subphotospheric Alfvén speed. For solar parameters, this time is a few hours. The model is, however, unrealistic because it assumes the entire subphotosphere at the driving footpoint is initially set into motion. This deficiency is addressed in § 4.8.2, where it is assumed that a thin upper layer of the subphotosphere is initially set into motion, rather than the whole subphotosphere. The driving layer generates Alfvénic fronts that propagate both upwards (into the corona) and downwards (into the subphotosphere), transferring momentum away from the driving layer. The dominant ‘braking’ of the driving layer is due to the downwards propagating front, because of the greater density of the subphotosphere. The timescale for the braking process is  $t_L = L/v_{A2}$ , where  $L$  is the thickness of the driving layer. For solar parameters, this process is likely to be important.

## 4.10 APPENDIX

### 4.10.1 Derivation of Equation (4.6) and discussion of the use of Equation (4.4)

Consider the two-dimensional geometry defined by Equation (4.1). The Maxwell equation  $\text{div } \mathbf{B} = 0$  is automatically satisfied for this choice of  $\mathbf{B}$  and the fluid equation of motion

$$\rho \left( \frac{\partial \mathbf{v}}{\partial t} + \mathbf{v} \cdot \text{grad } \mathbf{v} \right) = -\text{grad } p + \mathbf{J} \times \mathbf{B} \quad (4.90)$$

has the components

$$\frac{\partial}{\partial x} \left( p + B_y^2/2\mu_0 \right) = 0, \quad (4.91)$$

$$\rho \frac{\partial v_y}{\partial t} = \frac{B_0}{\mu_0} \frac{\partial B_y}{\partial z}, \quad (4.92)$$

and

$$\frac{\partial}{\partial z} \left( p + B_y^2/2\mu_0 \right) = 0. \quad (4.93)$$

Equations (4.91) and (4.93) imply Equation (4.5).

As noted in the above chapter, an important feature of the electrical conductivity of the solar photosphere is its anisotropy. Here we briefly consider this point, and show that the choice of geometry given by Equation (4.1) allows only the discussion of an isotropically conducting subphotosphere.

In the linear, one fluid approximation the appropriate (static) generalised Ohm's law is (e.g. Krall and Trivelpiece, 1973; Alfvén and Fälthammar, 1963)

$$\mathbf{J} = \sigma (\mathbf{E} + \mathbf{v} \times \mathbf{B}), \quad (4.94)$$

where

$$\sigma = \begin{pmatrix} \sigma_P & \sigma_H & 0 \\ -\sigma_H & \sigma_P & 0 \\ 0 & 0 & \sigma_{\parallel} \end{pmatrix}.$$

Here  $\sigma_P$  and  $\sigma_H$  are the *Pederson* and *Hall* cross-conductivities respectively and  $\sigma_{\parallel}$  is the parallel conductivity, where:

$$\sigma_P = \frac{ne^2}{m_e} \left( \frac{\nu_{ne}}{\nu_{ne}^2 + \omega_e^2} + \frac{m_e}{m_i} \frac{\nu_{ni}}{\nu_{ni}^2 + \omega_i^2} \right), \quad (4.95)$$

$$\sigma_H = \frac{ne^2}{m_e} \left( \frac{-\omega_e}{\nu_{ne}^2 + \omega_e^2} + \frac{m_e}{m_i} \frac{\omega_i}{\nu_{ni}^2 + \omega_i^2} \right), \quad (4.96)$$

and

$$\sigma_{\parallel} = \frac{ne^2}{m_e} \left( \frac{1}{\nu_{ne}} + \frac{m_e}{m_i} \frac{1}{\nu_{ni}} \right). \quad (4.97)$$

Here  $\omega_{\alpha}$  is the gyrofrequency for species  $\alpha$  and  $\nu_{ni}$  is the collision frequency between species  $i$  and the neutral background. The generalisation to a variety of ion species is straightforward.

The relative sizes of  $\sigma_P$  and  $\sigma_H$  determine whether the cross-field conduction below the photosphere will be significantly anisotropic. For example, if a field  $E_x$  is applied and  $\mathbf{v} = 0$  then the resulting cross field currents are in the ratio  $J_x/J_y = -\sigma_P/\sigma_H$ . Khan (1989) calculated the relative sizes of the cross-field conductivities  $\sigma_P$ ,  $\sigma_H$  for the subphotospheric region, based on solar atmosphere models (e.g. Spruit 1974) and with a field appropriate for sunspots ( $B = 0.15$  T). Khan (1989) found that the cross-field conductivities are non-zero in the weakly ionised regions of the solar atmosphere, beginning with the photosphere, where  $n_{HII}/n_{HI} \approx 10^{-4}$  (Priest, 1982). For the subphotospheric regions of interest,  $\sigma_P \approx -\sigma_H$ . Just below the photosphere,  $|\sigma_{H,P}| \approx 10^2 \text{ Sm}^{-1}$ , rising quickly to  $\approx 10^5 \text{ Sm}^{-1}$  at depths of greater than 1 Mm. The cross field conductivities are slowly increasing functions of depth beyond this point. Khan (1989) integrated the cross field conductivities to a depth of about 1 Mm, and found the values  $|\Sigma_{H,P}| \approx 10^{11} \text{ S}$ , which are used in this chapter. These estimates were greater than those of previous authors who had neglected the dominant contribution from the partially ionised, subphotospheric regions. Khan's estimates also suggest that anisotropy is likely to be an important feature of subphotospheric conduction. It is not enough to assume an isotropic conductivity  $\sigma_{\parallel}$  at and below the photosphere (cf. Kovitya and Cram, 1983).

The simple geometry chosen here — i.e. Equation (4.1) — is not consistent with an anisotropic Ohm's law, as follows. Taking the product of the matrix  $\sigma$  and the vector  $\mathbf{v} \times \mathbf{B}$  gives a contribution to the current density  $\mathbf{J}$  with  $y$  component  $-\sigma_H v_y B_0$ . This will be inconsistent with the requirement  $J_y = 0$  unless  $\sigma_H = 0$ .

Setting  $\sigma_H = 0$  and  $\sigma_{\parallel} = \sigma_P$  for simplicity, we have the simple Ohm's law (4.4). The electric field may be written  $\mathbf{E} = \sigma_P^{-1} \mathbf{J} - \mathbf{v} \times \mathbf{B}$ . Taking the curl of this expression in the given geometry and using the Maxwell Faraday equation  $\text{curl } \mathbf{E} = -\partial \mathbf{B} / \partial t$  together with Equation (4.3), we obtain

$$\frac{\partial B_y}{\partial t} = \frac{1}{\gamma} \left( \frac{\partial^2 B_y}{\partial z^2} + \frac{\partial^2 B_y}{\partial x^2} \right) + B_0 \frac{\partial v_y}{\partial z}, \quad (4.98)$$

where  $\gamma = \mu_0 \sigma_P$ .

Equation (4.98) and Equation (4.92) give Equation (4.6), under the assumption of constant density  $\rho$ . According to Equation (4.3), the components of current density obey the same equation, as does  $v_y$ .

#### 4.10.2 Derivation of Equation (4.15)

To restate, we want to solve Equation (4.6) subject to the boundary and initial conditions (4.10) and (4.11) respectively, and with the additional assumption that

$$\lim_{z \rightarrow \infty} B_y(x, z, t) = 0. \quad (4.99)$$

Laplace transforming Equation (4.6) with the initial conditions (4.11) gives the elliptic partial differential equation (e.g. Zwillinger, 1992)

$$-s^2 \check{B}_y + v_A^2 \frac{\partial^2 \check{B}_y}{\partial z^2} + \frac{s}{\gamma} \frac{\partial}{\partial t} \left( \frac{\partial^2 \check{B}_y}{\partial x^2} + \frac{\partial^2 \check{B}_y}{\partial z^2} \right) = 0, \quad (4.100)$$

where  $\check{B}_y = \check{B}_y(x, z, s)$  denotes the Laplace transform of  $B_y(x, z, t)$ . Next, Fourier transforming Equation (4.100) in  $x$  produces the simple ordinary differential equation

$$\frac{d^2 \hat{\check{B}}_y}{dz^2} = \beta(k, s)^2 \hat{\check{B}}_y, \quad (4.101)$$

where

$$\beta(k, s) = \alpha \left( k^2 + \gamma s \right)^{\frac{1}{2}}, \quad \alpha^2 = \frac{s}{s + \gamma v_A^2}, \quad (4.102)$$

and where  $\hat{\check{B}}_y(k, z, s)$  is the Fourier transform of  $\check{B}_y(x, z, s)$ . The solution of Equation (4.101) which satisfies Equation (4.99) is the decaying exponential, and so the Laplace transform of the solution to Equation (4.6) may be written

$$\check{B}_y(x, z, s) = \frac{1}{2\pi} \int_{-\infty}^{\infty} dk A(k, s) \exp[-\beta(k, s)z + ikx]. \quad (4.103)$$

The coefficient  $A(k, s)$  in Equation (4.103) is determined by setting  $z = 0$  and hence recognising that  $A(k, s)$  is the Fourier transform of  $\check{B}_y(x, 0, s)$ . Consequently,

$$A(k, s) = \int_{-\infty}^{\infty} dx' \check{B}_y(x', 0, s) \exp(-ikx'), \quad (4.104)$$

where

$$\check{B}_y(x', 0, s) = \mu_0 \phi(x')/s. \quad (4.105)$$



Equation (4.105) is obtained by taking the Laplace transform of the initial condition (4.11). Substituting Equation (4.104) with Equation (4.105) back into Equation (4.103) and reversing the order of integration, we obtain

$$\tilde{B}_y(x, z, s) = \frac{\mu_0}{\pi s} \int_{-\infty}^{\infty} dx' \phi(x') \int_0^{\infty} dk \exp[-\beta(k, s)z] \cos k(x - x'). \quad (4.106)$$

The integral over  $k$  in this expression may be evaluated (Gradshteyn and Ryzhik, 1980) to give

$$\int_0^{\infty} dk \exp[-\alpha(k^2 + \gamma s)^{\frac{1}{2}}z] \cos k(x - x') = \alpha z (\gamma s)^{\frac{1}{2}} \Upsilon(x, x', z, s), \quad (4.107)$$

where

$$\Upsilon(x, x', z, s) = \frac{K_1\left(\{\gamma s [\alpha^2 z^2 + (x - x')^2]\}^{\frac{1}{2}}\right)}{[\alpha^2 z^2 + (x - x')^2]^{\frac{1}{2}}}. \quad (4.108)$$

Substituting Equation (4.107) into Equation (4.106) yields Equation (4.15).

### 4.10.3 Derivation of Equation (4.18) from (4.15)

Equation (4.15) may be written

$$\tilde{B}_y(x, z, s) = \mu_0 \int_{-\infty}^{\infty} d\xi \phi(\xi) H(x, \xi, z, s), \quad (4.109)$$

with

$$H(x, \xi, z, s) \equiv \frac{\alpha z}{\pi} \left(\frac{\gamma}{s}\right)^{\frac{1}{2}} \Upsilon(x, \xi, z, s), \quad (4.110)$$

where  $\Upsilon(x, \xi, z, s)$  is defined by Equation (4.108). It is easy to show that

$$\lim_{\gamma \rightarrow \infty} H(x, \xi, z, s) = 0 \quad \text{if } x \neq \xi, \quad (4.111)$$

and by reference to a table of integrals (Gradshteyn and Ryzhik, 1980),

$$\int_{-\infty}^{\infty} d\xi H(x, \xi, z, s) = \frac{1}{s} \exp[-(\gamma s)^{\frac{1}{2}}z]. \quad (4.112)$$

Together, Equations (4.111) and (4.112) imply that

$$\lim_{\gamma \rightarrow \infty} H(x, \xi, z, s) = \frac{1}{s} \exp(-sz/v_A) \delta(x - \xi), \quad (4.113)$$

and this identification allows the integral in Equation (4.109) to be performed in the limit of infinite conductivity, to give Equation (4.18).

## Chapter 5

# An equivalent circuit for Alfvén waves in a stratified atmosphere

**Abstract:** An equivalent circuit is derived to represent linear, vertically propagating Alfvén waves in a horizontally stratified atmosphere with applied vertical magnetic field. A transmission line circuit is identified for arbitrary density and conductivity profiles, although an explicit input impedance can only be written down for particular cases.

By way of example, the model is applied to Alfvén waves generated at the solar photosphere and propagating in the solar chromosphere, following Hollweg (1972). The chromosphere is modelled as a region with bi-exponential density variation. Alfvén waves are reflected and transmitted at the discontinuity in scale height, a process described by adding a terminating impedance to the transmission line. For the case of equal scale heights in the two regions, a series  $RC$  circuit can also represent the input impedance, although frequency-dependent circuit elements are required. The equivalent circuits arrived at provide a simple model of Alfvén wave propagation in the solar chromosphere, which is relevant to the coronal heating problem, and to solar flares. The role of stratification in defining the circuits has not been looked at before.

## 5.1 Introduction

An equivalent circuit approach has often been adopted by solar theorists to describe the bulk plasma physics of energy storage and conversion in the solar atmosphere (Spicer, 1982). In particular, the circuit approach has found application in the description of a flaring coronal loop (for a review see Melrose, 1993), and in the long-standing problem of coronal heating (Ionson, 1982; 1984).

One criticism of the circuit theory approach is that it is only an approximation to the underlying plasma physics. The relevant circuits are generally deduced by qualitative reasoning, rather than derived from first principles (i.e. the fluid equation of motion and Maxwell's equations). Consequently, the picture is incomplete. For example, a simple circuit model of a flaring coronal loop does not describe the propagation of magnetic energy at the Alfvén speed in the loop (Melrose, 1993).

A rigorous circuit theory description of the propagation of Alfvén waves was provided by Scheurwater and Kuperus (1988; cf. Haerendel, 1983). Scheurwater and Kuperus (1988) derived a transmission line circuit to describe Alfvén wave propagation in a uniform, weakly damped plasma, and also considered the circuit description of the reflection of the wave from a density step. This chapter extends the approach of Scheurwater and Kuperus (1988) to derive a circuit describing Alfvén wave propagation in a stratified, damped plasma. Scheurwater and Kuperus (1989) also considered the generalisation to a non-uniform plasma, but restricted their attention to a weakly varying plasma. Here we consider a plasma with arbitrary density variation (and conductivity variation) in the direction of a uniform, background magnetic field. This is particularly relevant to the solar wind, where significantly non-WKB waves are observed (Hollweg, 1972). The objective is to determine the role of stratification in defining the circuit elements. The model considers only Alfvén waves propagating parallel to the background magnetic field, and perpendicular to the stratification. Consequently, there is no need to consider refraction, and magnetohydrodynamic (MHD) mode coupling.

The model is applied to the case of an ideal, bi-exponential atmosphere, following Hollweg (1972). This particular density profile is relevant because the density profile in detailed solar atmosphere models is well approximated as a piecewise exponential for describing wave propagation (Hollweg, 1972; 1978; 1981; 1984).

## 5.2 Alfvén waves in a stratified atmosphere

Consider a stratified plasma, i.e. with variation only in the  $z$  direction, threaded by a uniform background magnetic field  $\mathbf{B}_0 = B_0 \hat{\mathbf{z}}$ . The plasma is assumed to have a finite conductivity,  $\sigma_P(z)$  and to obey the Ohm's law

$$\mathbf{J} = \sigma_P(z) (\mathbf{E} + \mathbf{v} \times \mathbf{B}). \quad (5.1)$$

Then the linearised MHD equations and Maxwell's equations permit incompressible, transverse perturbations  $\mathbf{B} = B \hat{\mathbf{b}}$  and  $\mathbf{E} = E \hat{\mathbf{b}} \times \hat{\mathbf{z}}$ , which satisfy the pair of equations

$$\frac{\partial B}{\partial t} + \frac{\partial E}{\partial z} = 0, \quad (5.2)$$

and

$$\frac{\partial E}{\partial t} + [\mu_0 \sigma_P(z)]^{-1} \frac{\partial^2 B}{\partial z \partial t} + v_A(z)^2 \frac{\partial B}{\partial z} = 0. \quad (5.3)$$

For simplicity, we consider only harmonically varying perturbed fields ( $\sim e^{i\omega t}$ ). Following Scheurwater and Kuperus, a voltage,  $V(z)$ , and current,  $I(z)$ , may be assigned to the perturbed field quantities according to the relations

$$E(z, t) = \frac{V(z)}{l} e^{i\omega t} \quad \text{and} \quad B(z, t) = \frac{\mu_0 I(z)}{l} e^{i\omega t}, \quad (5.4)$$

where  $l$  is a characteristic length. With these definitions, the time averaged Poynting flux through a square of area  $l^2$  (perpendicular to  $z$ ) is  $\frac{1}{2} \text{Re}(VI^*)$ . Substituting  $V$  and  $I$ , as defined by Equation (5.4) into Equations (5.2) and (5.3), gives the coupled pair of ordinary differential equations

$$\frac{dV}{dz} = -z_A I, \quad (5.5)$$

and

$$\frac{dI}{dz} = -\frac{V}{z_B(z)}, \quad (5.6)$$

where

$$z_A = i\omega \mu_0, \quad (5.7)$$

and

$$z_B(z) = \frac{\mu_0 v_A(z)^2}{i\omega} + \frac{1}{\sigma_P(z)}. \quad (5.8)$$

Equations (5.5) and (5.6) may be combined to give a single equation describing the variation in complex impedance,  $Z(z) \equiv V/I$ , in the plasma;

$$\frac{dZ}{dz} = -z_A + \frac{1}{z_B(z)} Z^2. \quad (5.9)$$

Equations (5.5) and (5.6) — or alternatively, Equation (5.9) — describe the variation of current and voltage in a transmission line, with series impedance  $z_A$  per unit length, and shunt impedance  $z_B(z)$  per unit length (see the Appendix, § 5.5.1). Comparison of Equations (5.7) and (5.8) with the impedance of standard circuit elements from circuit theory,

$$Z_{\text{ind}} = i\omega L, \quad Z_{\text{cap}} = \frac{1}{i\omega C}, \quad Z_{\text{res}} = R, \quad (5.10)$$

allows the identification of the transmission line elements. Specifically we may write  $z_A = i\omega l_A$ , to identify a series inductance  $l_A = \mu_0$  per unit length; and  $z_B(z) = [i\omega c_B(z)]^{-1} + r_B(z)$ , to identify a shunt capacitance,  $c_B(z) = [\mu_0 v_A(z)^2]^{-1}$ , and shunt resistance,  $r_B(z) = [\sigma_P(z)]^{-1}$ , per unit length. Figure 5.1 illustrates the transmission line composed of these elements.

Equation (5.9) admits several simple solutions. If the impedance is assumed to be independent of distance  $z$ , then the solution is  $Z = (z_A z_B)^{\frac{1}{2}}$ . In particular, this is appropriate when the plasma is lossless, and then  $Z = \mu_0 v_A$ , the Alfvénic impedance of the plasma. More generally, if the element  $z_B$  is assumed independent of  $z$ , then the ordinary differential equation (5.9) may be analytically solved for the impedance  $Z(z)$ . It is necessary to specify a load impedance, say  $Z_h \equiv Z(h)$ . The input impedance,  $Z_0 \equiv Z(0)$ , obtained this way is

$$Z_0 = \eta \frac{Z_h + i\eta \tan(2\zeta h)}{\eta + iZ_h \tan(2\zeta h)}, \quad (5.11)$$

where  $\eta = (z_A z_B)^{\frac{1}{2}}$  and  $\zeta = (-z_A/z_B)^{\frac{1}{2}}$ . Equation (5.11) is the input impedance considered by Scheurwater and Kuperus (1988).

The rest of this chapter is devoted to another exact solution of Equation (5.9), namely that of an ideal stratified atmosphere with exponential density variation. This case is appropriate to describe the propagation of Alfvén waves, generated at the photosphere, through the chromosphere.

### 5.3 Alfvén waves in an exponential atmosphere

Consider a region ‘1’ of horizontally stratified plasma with density variation

$$\rho_1 = \rho_{01} \exp(-z/\Lambda_1), \quad (5.12)$$

(where  $\Lambda_1$  is the scale height) and ambient magnetic field  $\mathbf{B}_0 = B_0 \hat{\mathbf{z}}$ . The linearised MHD equations with this density profile lead to the solution for harmonic, transverse, incompressible velocity perturbations (Ferraro, 1954; Ferraro

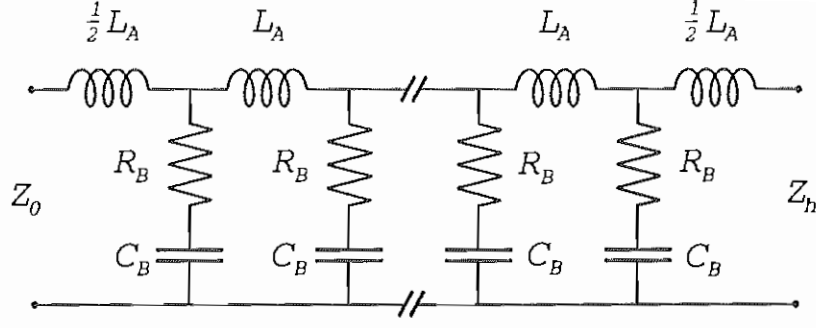


Figure 5.1: The transmission line derived for Alfvén wave propagation in a stratified atmosphere. The elements depicted are related to those defined above as follows:  $L_A = l_A \delta z$ ,  $R_B = r_B(z)/\delta z$ , and  $C_B = c_B(z)\delta z$ , where  $\delta z$  is an incremental length in the direction of stratification. The length of line shown represents propagation from  $z = 0$  (where the input impedance is  $Z_0$ ), to  $z = h$  (where the load impedance is  $Z_h$ ).

and Plumpton, 1958)

$$v_1(z, t) = \left[ AH_0^{(1)}(2\sigma_1 \xi_1) + BH_0^{(2)}(2\sigma_1 \xi_1) \right] \exp(i\omega t), \quad (5.13)$$

where

$$\xi_1 = \exp(-z/2\Lambda_1), \quad \sigma_1 = \Lambda_1 \omega / v_{A1}, \quad (5.14)$$

$A$  and  $B$  are constants (with the dimensions of velocity), and  $v_{A1} = B_0/(\rho_{01}\mu_0)^{\frac{1}{2}}$  is the Alfvén velocity at  $z = 0$ .  $H_0^{(1)}(x)$  and  $H_0^{(2)}(x)$  are the Hankel functions (Abramowitz and Stegun, 1965). Equation (5.13) describes Alfvén waves propagating vertically in a horizontally stratified, exponential atmosphere, and has attracted much attention and application in solar models (e.g. Hollweg, 1972; 1978; 1981; 1984; Rosner *et al.* 1986). Note that the (dimensionless) parameter  $\sigma_1$  is of order the ratio of the scale height to the wavelength of the propagating wave. Also, resistivity and viscosity have been neglected in the derivation of Equation (5.13).

To first order, the electric field associated with Equation (5.13) is given by  $\mathbf{E}_1 = -\mathbf{v}_1 \times \mathbf{B}_0$ , and has magnitude

$$E_1(z, t) = -B_0 \left[ AH_0^{(1)}(2\sigma_1 \xi_1) + BH_0^{(2)}(2\sigma_1 \xi_1) \right] \exp(i\omega t). \quad (5.15)$$

The Faraday-Maxwell equation gives the corresponding magnetic field of the wave to be

$$B_1(z, t) = -i \frac{B_0 \xi_1}{v_{A1}} \left[ AH_1^{(1)}(2\sigma_1 \xi_1) + BH_1^{(2)}(2\sigma_1 \xi_1) \right] \exp(i\omega t). \quad (5.16)$$

Without loss of generality, axes are taken such that  $\mathbf{v}_1 = v_1 \hat{y}$ ,  $\mathbf{E}_1 = E_1 \hat{x}$  and  $\mathbf{B}_1 = B_1 \hat{y}$ .

Equations (5.13), (5.15) and (5.16) may be physically interpreted as a propagating wave solution, as follows. The time averaged Poynting vector,  $\mathbf{P} = \frac{1}{2} \text{Re}(\mathbf{E} \times \mathbf{B}^*)$ , is in the  $z$  direction, is second order (in the linearised fields) and has magnitude (Hollweg, 1972)

$$P = \frac{B_0^2}{2\mu_0} \frac{|A|^2 - |B|^2}{\pi\omega\Lambda_1}. \quad (5.17)$$

Equation (5.17) allows the identification of  $AH^{(1)}(2\sigma_1\xi_1)$  and  $BH^{(2)}(2\sigma_1\xi_1)$  as upward and downward going waves respectively (where  $+z$  is the ‘upward’ direction). Alternatively, in the limit  $\Lambda_1 \rightarrow \infty$  (so that  $\rho_1 \rightarrow \rho_{01}$ ) the solutions above become upward and downward going, attenuated plane waves with coefficients  $A, B$  respectively. The uniform density limit is important in interpreting several of the results derived below.

### 5.3.1 A bi-exponential chromosphere

Next consider (after Hollweg, 1972), a plasma where region ‘1’ occupies  $0 \leq z \leq h$  and a region ‘2’, with scale height  $\Lambda_2$ , occupies  $z \geq h$ . In region ‘2’, the plasma density is given by

$$\rho_2 = \rho_{02} \exp(-z/\Lambda_2). \quad (5.18)$$

Comparing Equations (5.12) and (5.18), continuity of density at  $z = h$  implies  $\rho_{02} = \rho_{01} \exp(-h/\Lambda_1)$ .

The bi-exponential density variation described above was suggested as an approximate model of the density variation in the solar chromosphere by Hollweg (1972), based on a quiet chromosphere model. In Hollweg’s model,  $z = 0$  represents the photosphere, and (for reference) the appropriate scale heights are

$$\Lambda_1 = 185 \text{ km} \quad \text{and} \quad \Lambda_2 = 1125 \text{ km}, \quad (5.19)$$

with the break in scale height occurring at  $h = 1950$  km. The discontinuity in scale height at  $z = h$  is a good approximation to the true (smooth) density variation for waves with wavelength longer than the scale over which the smooth transition occurs. The bi-exponential density model well approximates the quiet chromosphere model considered by Hollweg (1972) up to a height of  $10^4$  km. The increase in scale height through the chromosphere occurs because temperature is

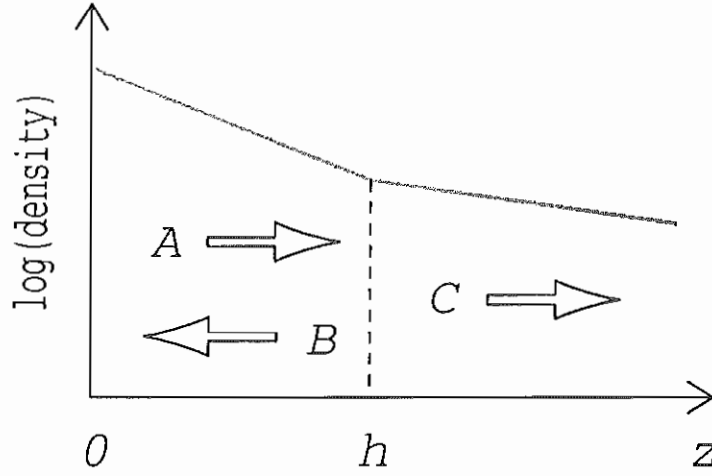


Figure 5.2: The geometry of the model for Alfvén wave propagation in a bi-exponential chromosphere. Waves are generated at  $z = 0$  and propagate to the break in scale height at  $z = h$ , where they are reflected or transmitted. The coefficients  $A$ ,  $B$  and  $C$  describe the incident, reflected and transmitted waves respectively.

increasing towards the corona. Extending this approach, the density variation of the solar atmosphere from the photosphere to the corona may be modelled by a piecewise exponential density variation (Hollweg, 1978; 1981).

Introducing the parameters

$$\xi_2 = \exp[-(z - h)/2\Lambda_2] \quad \text{and} \quad \sigma_2 = \Lambda_2\omega/v_{A2}, \quad (5.20)$$

where  $v_{A2} = v_{A1} \exp(h/2\Lambda_1)$  is the Alfvén velocity at  $z = h$ , the corresponding solutions to Equations (5.13), (5.15) and (5.16) may be written down. For example, the velocity variation in region '2' is

$$v_2(z, t) = [CH_0^{(1)}(2\sigma_2\xi_2) + DH_0^{(2)}(2\sigma_2\xi_2)] \exp(i\omega t). \quad (5.21)$$

After Hollweg (1972), incoming waves from  $z = \infty$  are ignored (i.e.  $D = 0$ ). The model then describes parallel propagating Alfvén waves, generated at the photosphere or below and traversing the chromosphere. Figure 5.2 illustrates the geometry of the model.

The incident, reflected and transmitted waves are related by the boundary conditions of continuity of  $v_j$  and  $B_j$  ( $j = 1, 2$ ) at  $z = h$ . This process defines the reflection ( $R$ ) and transmission ( $T$ ) coefficients

$$R \equiv \frac{B}{A} = \frac{H_0^{(1)}(\gamma)H_1^{(1)}(\beta) - H_0^{(1)}(\beta)H_1^{(1)}(\gamma)}{H_0^{(2)}(\beta)H_1^{(1)}(\gamma) - H_0^{(1)}(\gamma)H_1^{(2)}(\beta)} \quad (5.22)$$



and

$$T \equiv \frac{C}{A} = \frac{-4i}{\pi\beta [H_0^{(2)}(\beta)H_1^{(1)}(\gamma) - H_0^{(1)}(\gamma)H_1^{(2)}(\beta)]}, \quad (5.23)$$

where the notation

$$\alpha = \frac{2\Lambda_1\omega}{v_{A1}}, \quad \beta = \frac{2\Lambda_1\omega}{v_{A2}}, \quad \gamma = \frac{2\Lambda_2\omega}{v_{A2}} \quad (5.24)$$

is introduced. Note that  $\alpha = 2\sigma_1$  and  $\gamma = 2\sigma_2$ , in terms of the notation introduced above. A special case of Equations (5.22) and (5.23) is that of equal scale heights in the two matched regions, i.e.  $\Lambda_1 = \Lambda_2$ . Then  $\beta = \gamma$  so that  $R = 0$ ,  $T = 1$ . This is the expected result for a single stratified plasma: only an upward propagating wave exists.

Equations (5.22) and (5.23) were derived by Hollweg (1972), who imposed the additional constraint that the waves are harmonically driven at  $z = 0$ . Hollweg (1972) thereby defined  $A$  in terms of the amplitude of the driving velocity, but for present purposes that step is not required.

### 5.3.2 The input impedance

The next step is to derive the input impedance describing the Alfvén waves given by Equations (5.13) and (5.21) above. Following the procedure of § 5.2, for the given waves, matched at  $z = h$ , the voltage and current defined by Equation (5.4) are given by

$$V(z) = \begin{cases} V_i H_0^{(1)}(2\sigma_1\xi_1) + V_r H_0^{(2)}(2\sigma_1\xi_1) & \text{if } 0 \leq z \leq h \\ V_t H_0^{(1)}(2\sigma_2\xi_2) & \text{if } z \geq h, \end{cases} \quad (5.25)$$

and

$$I(z) = \begin{cases} i(\xi_1/Z_1) [V_i H_1^{(1)}(2\sigma_1\xi_1) + V_r H_1^{(2)}(2\sigma_1\xi_1)] & \text{if } 0 \leq z \leq h \\ i(\xi_2/Z_2) V_t H_1^{(1)}(2\sigma_2\xi_2) & \text{if } z \geq h. \end{cases} \quad (5.26)$$

Here

$$V_i = -B_0 I A, \quad V_r = R V_i, \quad V_t = T V_i, \quad (5.27)$$

and the characteristic impedances

$$Z_1 = \mu_0 v_{A1} \quad \text{and} \quad Z_2 = \mu_0 v_{A2} \quad (5.28)$$

are introduced.  $Z_1$  and  $Z_2$  are the impedances that would be assigned to corresponding plane waves at the origin and at  $z = h$  respectively, since (for example)

$$Z_1 = \frac{Z_0}{n_{A1}}, \quad (5.29)$$

where  $Z_0 = (\mu_0/\epsilon_0)^{\frac{1}{2}}$  is the impedance of free space ( $Z_0 \approx 377 \Omega$ ) and  $n_{A1} = c/v_{A1}$  is the refractive index of a plane Alfvén wave at  $z = 0$ .

The complex impedance associated with the wave is then given by

$$Z(z) = \begin{cases} -i(Z_1/\xi_1) [H_0^{(1)} + RH_0^{(2)}] / [H_1^{(1)} + RH_1^{(2)}] & \text{if } 0 \leq z \leq h \\ -i(Z_2/\xi_2) H_0^{(1)}/H_1^{(1)} & \text{if } z \geq h, \end{cases} \quad (5.30)$$

where the arguments of the Hankel functions are  $2\sigma_1\xi_1$  for  $0 \leq z \leq h$  and  $2\sigma_2\xi_2$  for  $z \geq h$ . It is straightforward to check that in the limit  $\Lambda_1, \Lambda_2 \rightarrow \infty$ , i.e. the limit of a uniform density plasma, Equation (5.30) reduces to  $Z_1$ , the impedance of an Alfvén wave in a uniform medium.

The input impedance,  $Z_0$ , and load impedance,  $Z_h$ , for the model are given by

$$Z_0 = -iZ_1 \frac{H_0^{(1)}(\alpha) + RH_0^{(2)}(\alpha)}{H_1^{(1)}(\alpha) + RH_1^{(2)}(\alpha)}, \quad (5.31)$$

and

$$Z_h = -iZ_2 \frac{H_0^{(1)}(\gamma)}{H_1^{(1)}(\gamma)}. \quad (5.32)$$

### 5.3.3 An equivalent circuit when $\Lambda_1 = \Lambda_2$

For the case of matching scale heights in regions ‘1’ and ‘2’ — i.e. a single stratified plasma — as remarked above the reflection coefficient  $R$  is zero so that Equation (5.31) becomes

$$Z_0 = -iZ_1 \frac{H_0^{(1)}(\alpha)}{H_1^{(1)}(\alpha)}. \quad (5.33)$$

Equation (5.33) may be written in the form

$$Z_0 = \frac{Z_1}{J_1(\alpha)^2 + Y_1(\alpha)^2} \{2/\pi\alpha - i[J_0(\alpha)J_1(\alpha) + Y_0(\alpha)Y_1(\alpha)]\}, \quad (5.34)$$

where  $J_i(x)$  and  $Y_i(x)$  are Bessel functions of the first and second kinds respectively (Abramowitz and Stegun, 1965). In Equation (5.34) the combination  $J_0J_1 + Y_0Y_1$  is positive for all  $\alpha$ . For large  $\alpha$ ,  $Z_0$  approaches  $Z_1$ , the impedance of a uniform density plasma. This may be understood by noting that  $\alpha$  is the ratio of the scale height to the wavelength of the Alfvén wave at  $z = 0$ . If this ratio is large, the density does not change appreciably over a wavelength and so the wave encounters an almost uniform medium.

Equation (5.34) could be interpreted as the input impedance to a transmission line, following the approach of § 5.2 above. However, it may also be interpreted as

the input impedance to a series  $RC$  circuit, with frequency-dependent elements, as follows. Comparison of Equation (5.34) with the impedance of standard circuit elements from circuit theory, Equation (5.10), allows the identification

$$Z_0(\omega) = R_0(\omega) + \frac{1}{i\omega C_0(\omega)}, \quad (5.35)$$

where

$$R_0(\omega) = \frac{2Z_1}{\pi\alpha [J_1(\alpha)^2 + Y_1(\alpha)^2]}, \quad (5.36)$$

and

$$C_0(\omega) = \frac{J_1(\alpha)^2 + Y_1(\alpha)^2}{\omega Z_1 [J_0(\alpha)J_1(\alpha) + Y_0(\alpha)Y_1(\alpha)]}. \quad (5.37)$$

Equations (5.36) and (5.37) describe a frequency-dependent resistance and capacitance respectively, and establish that the input impedance in the case  $r = 1$  may be represented by a series  $RC$  circuit, with frequency-dependent elements. The frequency dependence of the elements does not obscure their unique identification as resistive and capacitive by their phase. The phase, in turn is uniquely specified by the requirement that the input impedance reduce to  $Z_1$  in the limit of a uniform density medium, i.e. as  $\Lambda_1 \rightarrow \infty$ . The positive definiteness of the combinations of Bessel functions in Equation (5.37) is essential to this line of argument. Note that in the uniform density limit, only a resistance remains; the capacitance (and the form of the resistance for finite  $\Lambda_1$ ) contain the information about the stratification of the plasma.

The resistive and capacitive elements  $R_0(\omega)$  and  $C_0(\omega)$  may be interpreted as follows. It is easy to confirm that

$$\frac{1}{2} |I(0)|^2 R_0(\omega) = l^2 P, \quad (5.38)$$

where  $P$  is the magnitude of the time averaged Poynting vector, given by Equation (5.17). Equation (5.38) identifies  $R_0(\omega)$  as the radiation resistance of the generator at  $z = 0$  (see the Appendix to this chapter, § 5.5.2).

The interpretation of  $C_0(\omega)$  is slightly more involved. In the Appendix to this chapter (§ 5.5.2) it is shown that  $1/C_0(\omega)$  is a measure of the magnetic energy stored in the wave.

### 5.3.4 An equivalent circuit when $\Lambda_1 \neq \Lambda_2$

Following the theory outlined in § 5.2, a transmission line with series inductance  $l_{A1} = \mu_0$  per unit length and a shunt capacitance  $c_{B1}(z) = \xi_1^2/\mu_0 v_{A1}^2$  per unit

length is appropriate to describe Alfvén wave propagation in region ‘1’. There are no resistive elements down the line because the plasma is assumed to be lossless.

The process of reflection and transmission of Alfvén waves in the model chromosphere is described by the termination of the transmission line at  $z = h$  in a load impedance,  $Z_h$ , defined by Equation (5.32).  $Z_h$ , like  $Z_0$  in the case  $\Lambda_1 = \Lambda_2$ , can be represented by a transmission line (following §5.2), or by a series  $RC$  circuit with frequency-dependent elements. The series circuit is described by:

$$Z_h(\omega) = R_h(\omega) + \frac{1}{i\omega C_h(\omega)}, \quad (5.39)$$

where

$$R_h(\omega) = \frac{2Z_2}{\pi\gamma [J_1(\gamma)^2 + Y_1(\gamma)^2]}, \quad (5.40)$$

and

$$C_h(\omega) = \frac{J_1(\gamma)^2 + Y_1(\gamma)^2}{\omega Z_2 [J_0(\gamma)J_1(\gamma) + Y_0(\gamma)Y_1(\gamma)]}. \quad (5.41)$$

The load capacitance,  $C_h(\omega)$ , and load resistance,  $R_h(\omega)$ , are physically interpreted as were  $C_0(\omega)$  and  $R_0(\omega)$  (see §5.3.3).

## 5.4 Conclusions

The equivalent circuit approach is one that is widely used in solar physics to describe the bulk energetics of flares, and of coronal heating. The circuits considered are usually deduced in an ad hoc fashion, rather than being rigorously derived from the plasma equation of motion and Maxwell’s equations. Consequently they neglect some aspects of the plasma physics, and in particular neglect wave propagation.

Kuperus and Scheurwater (1988; cf. Haerendel, 1983) rigorously derived an equivalent circuit to describe Alfvén wave propagation in a uniform magnetised plasma. This chapter extends their approach to describe Alfvén wave propagation in a stratified plasma, relevant for example to Alfvén waves generated at the photosphere and propagating upwards in the solar chromosphere. Scheurwater and Kuperus (1989) also considered the case of a stratified plasma, but their approach applies only to a plasma with a slowly varying density profile. The model developed here is appropriate for an arbitrary density profile and conductivity, in the direction of stratification. As an example, the model is applied to Alfvén wave

propagation and reflection in the bi-exponential chromosphere model of Hollweg (1972).

## 5.5 APPENDIX

### 5.5.1 The transmission line equations

This section of the Appendix establishes that Equation (5.9) represents the variation in impedance of a transmission line, as discussed above.

Consider the choice of constituent element for a transmission line shown in Figure 5.3. The transmission line is assumed to be composed of infinitely many such elements. From the rules for combining impedances, the input impedance for this element is given by

$$Z(z) = \frac{1}{2}z_A\delta z + \left[ \frac{1}{\frac{1}{2}z_A\delta z + Z(z + \delta z)} + \frac{\delta z}{z_B(z)} \right]^{-1}. \quad (5.42)$$

Rearranging this equation and expanding in  $\delta z$  we obtain

$$\frac{Z(z + \delta z) - Z(z)}{\delta z} = -z_A + \frac{Z(z + \delta z)^2}{z_B(z)} + \mathcal{O}(\delta z^2). \quad (5.43)$$

Taking the limit  $\delta z \rightarrow 0$  in Equation (5.43) gives precisely Equation (5.9).

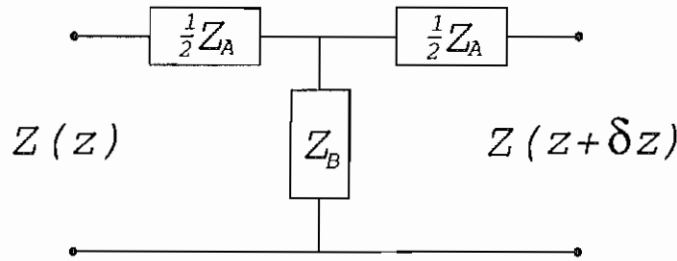


Figure 5.3: The constituent element for the transmission line, representing the change in impedance between  $z$  and  $z + \delta z$ . The elements depicted are related to those defined above as follows:  $Z_A = z_A\delta z$ , and  $Z_B = z_B(z)/\delta z$ .

### 5.5.2 Interpreting the input impedance

The interpretation of the series circuit elements assigned to the input impedance (§ 5.3.2 above) follows from the ‘complex’ Poynting theorem, i.e. the Poynting theorem applied to fields harmonically varying in time (Jackson, 1975). The specific treatment here follows Scheurwater and Kuperus (1988).

The Ampere and Faraday Maxwell equations (omitting displacement current), with the assumption of harmonic time variation ( $\sim e^{i\omega t}$ ) give the complex Poynting theorem

$$\frac{1}{2}\mathbf{J}^* \cdot \mathbf{E} + 2i\omega w_B + \text{div } \mathbf{P}_c = 0, \quad (5.44)$$

where  $\mathbf{P}_c = \mathbf{E} \times \mathbf{B}^*/2\mu_0$  is the complex Poynting vector ( $\mathbf{P} = \text{Re}(\mathbf{P}_c)$  is the usual, time averaged Poynting vector), and  $w_B = \mathbf{B} \cdot \mathbf{B}^*/4\mu_0$  is the energy density in magnetic fields.

Assuming the field geometry used in this chapter, expression (5.44) is integrated over the volume of a box, of cross section  $l$  by  $l$ , and length from  $z = 0$  to  $z = z_0$ . The complex Poynting vector is in the  $z$  direction and so gives a surface integral contribution at  $z = 0$  and  $z = z_0$ . The contribution at  $z = 0$  is related to the circuit parameters  $I(0)$  and  $V(0)$  by

$$-\frac{1}{2}V(0)I(0)^* = \iint_{z=0} \mathbf{P}_c \cdot d\mathbf{S}. \quad (5.45)$$

Writing  $Z(0) = V(0)/I(0)$ , the volume integral of Equation (5.44) together with Equation (5.45) allows the input impedance to be identified:

$$Z(0) = \frac{2}{|I(0)|^2} \left( \frac{1}{2} \int_V \mathbf{J}^* \cdot \mathbf{E} dV + 2i\omega \int_V w_B dV + \iint_{z=z_0} \mathbf{P}_c \cdot d\mathbf{S} \right). \quad (5.46)$$

For the lossless medium considered in § 5.3,  $\mathbf{J}^* \cdot \mathbf{E}$  is purely imaginary, and by definition  $w_B$  is purely real, so writing  $Z(0) = R + iX$ , the real and imaginary parts of the input impedance may be determined:

$$R = \frac{2}{|I(0)|^2} \iint_{z=z_0} \mathbf{P} \cdot d\mathbf{S}, \quad (5.47)$$

and

$$X = \frac{2}{|I(0)|^2} \left[ \frac{1}{2} \int_V \text{Im}(\mathbf{J}^* \cdot \mathbf{E}) dV + 2\omega \int_V w_B dV + \iint_{z=z_0} \text{Im}(\mathbf{P}_c) \cdot d\mathbf{S} \right]. \quad (5.48)$$

Equations (5.47) and (5.48) allow the circuit elements assigned to the input impedance to be physically interpreted. The resistive part of  $Z(0)$ ,  $R$ , is proportional to the ( $z$ -independent) Poynting flux, and is termed the radiation resistance of the generator of the wave. The reactive part,  $X$ , involves the energy stored in the magnetic field of the wave together with contributions from the imaginary Poynting flux and the imaginary rate of energy exchange between the fields and plasma. For a plasma with exponential density variation (see § 5.3), all three terms in Equation (5.48) contribute to  $X = -1/\omega C_0(\omega)$ , where  $C_0(\omega)$  is given by Equation (5.37).

# REFERENCES

- Abramowitz, M. and Stegun, I. A., (1965) *Handbook of Mathematical Functions*, (Dover: New York).
- Acton, L. W. *et al.*, (1992) "The morphology of  $20 \times 10^6$  K plasma in large non-impulsive solar flares," *Publ. Astron. Soc. Japan*, **44**, L71.
- Akasofu, S. -I., (1984) "An essay on sunspots and solar flares," *Planet. Space Sci.*, **32**, 1469.
- Akasofu, S. -I., (1994) "Assessing the magnetic reconnection paradigm," *EOS*, **75**, 1.
- Alfvén, H. and Carlqvist, P., (1967) "Currents in the solar atmosphere and a theory of solar flares," *Solar Phys.*, **1**, 220.
- Alfvén, H. and Fälthammar, C.-G., (1963) *Cosmical Electrodynamics*, 2nd ed. (Oxford University Press: Oxford).
- Aschwanden, M. J. and Güdel, M., (1992) "The coevolution of decimetric millisecond spikes and hard X-ray emission during solar flares," *Astrophys. J.*, **401**, 736.
- Benz, A. O., (1985) "Radio spikes and the fragmentation of flare energy release," *Solar Phys.*, **96**, 357.
- Benz, A. O., (1986) "Millisecond radio spikes," *Solar Phys.*, **104**, 99.
- Bray, R. J., Cram, L. E., Durrant, C. J. and Loughhead, R. E., (1991) *Plasma Loops in the Solar Corona*, (Cambridge University Press: Cambridge).
- Brown, J. C., (1971) "The deduction of energy spectra of non-thermal electrons in flares from the observed dynamic spectra of hard X-ray bursts," *Solar Phys.*, **18**, 489.
- Brown, J. C., (1972) "The directivity and polarisation of thick target X-ray bremsstrahlung from solar flares," *Solar Phys.*, **26**, 441.
- Brown, J. C., (1975) "The interpretation of spectra, polarization and directivity of solar hard X-rays" in *Solar Gamma-, X-, and EUV Radiation*, (ed. S. R. Kane) IAU Symposium No. 68 (D. Reidel: Dordrecht) 245.



- Brown, J. C., Correia, E., Fárník, F., Garcia, H., Hénoux, J.-C., La Rosa, T. N., Machado, M. E., Nakajima, H. and Priest, E. R., (1994) "Energy release in solar flares," *Solar Phys.*, **153**, 19.
- Brown, J. C. and McClymont, A. N., (1975) "The height distribution of flare hard X-rays in thick and thin target models," *Solar Phys.*, **41**, 135.
- Brown, J. C. and Smith, D. F., (1980) "Solar flares," *Rep. Prog. Phys.*, **43**, 125.
- Brown, J. C., Spicer, D. S. and Melrose, D. B., (1979) "Production of a collisionless conduction front by rapid coronal heating and its role in solar hard X-ray bursts," *Astrophys. J.*, **228**, 592.
- Canfield, R. C., de La Beaujardière, J.-F., Fan, Y., Leka, K. D., McClymont, A. N., Metcalf, T. R., Mickey, D. L., Wülser, J.-P. and Lites, B. W., (1993) "The morphology of flare phenomena, magnetic fields, and electric currents in active regions. I. Introduction and methods," *Astrophys. J.*, **411**, 362.
- Cheng, A. H.-D., Sidauruk, P. and Abousleiman, Y., (1994) "Approximate inversion of the Laplace transform," *The Mathematica Journal*, **4**, 76.
- Cowling, T. G., (1976) *Magnetohydrodynamics*, 2nd ed. (Adam Hilger: Bristol).
- Davies, B., (1978) *Integral Transforms and Their Applications*, Applied Mathematical Sciences vol. 25 (Springer: New York).
- de La Beaujardière, J.-F., Canfield, R. C. and Leka, K. D., (1993) "The morphology of flare phenomena, magnetic fields, and electric currents in active regions. II. NOAA active region 6233 (1990 August)," *Astrophys. J.*, **411**, 378.
- Dennis, B. R., (1988) "Solar flare hard X-ray observations," *Solar Phys.*, **118**, 49.
- Ding, Y. J., Ifong, Q. F., Hagyard, M. J., DeLoach, A. C., Liu, X. P., (1987) "Explorations of electric current system in solar active regions. I. Empirical inferences of the current flows," *Solar Phys.*, **109**, 307.
- Doschek, G. A. *et al.*, (1990) "Chromospheric explosions" in *Energetic Phenomena on the Sun*, (eds. M. R. Kundu, B. Woodgate and E. J. Schmal) (Kluwer: Dordrecht) 305.
- Emslie, A. G. and Machado, M. E., (1987) "On the hard X-ray spatial structure during the impulsive phase of solar flares," *Solar Phys.*, **107**, 263.
- Erdélyi, A., (1954) *Tables of Integral Transforms*, vols. I and II (McGraw-Hill: New York).
- Feldman, U., (1990) "The beam-driven chromospheric evaporation model for solar flares: A model not supported by observations from nonimpulsive large flares," *Astrophys. J.*, **364**, 322.
- Feldman, U., Hiei, E., Phillips, K. J. H., Brown, C. M. and Lang, J., (1994) "Very impulsive solar flares observed with the Yohkoh spacecraft," *Astrophys. J.*, **421**, 843.

- Ferraro, V. C. A., (1954) "On the reflection and refraction of Alfvén waves," *Astrophys. J.*, **119**, 393.
- Ferraro, V. C. A. and Plumpton, C., (1958) "Hydromagnetic waves in a horizontally stratified atmosphere," *Astrophys. J.*, **127**, 459.
- Finn, J. M. and Chen, J., (1990) "Equilibrium of solar coronal arcades," *Astrophys. J.*, **349**, 345.
- Forbes, T. G. and Malherbe, J. M., (1986) "A shock condensation mechanism for loop prominences," *Astrophys. J.*, **302**, L67.
- Goertz, C. K. and Boswell, R. W., (1979) "Magnetosphere-ionosphere coupling," *J. Geophys. Res.*, **84**, 7239.
- Gosling, J. T., (1993) "The solar flare myth," *J. Geophys. Res.*, **98**, 18937.
- Gradshteyn, I. S. and Ryzhik, I. M., (1980) *Table of Integrals, Series, & Products*, (Academic Press: New York).
- Haerendel, G., (1980) "Auroral particle acceleration – an example of a universal plasma process," *ESA Journal*, **4**, 1980.
- Haerendel, G., (1983) "An Alfvén wave model for auroral arcs" in *High-Latitude Plasma Physics*, (ed. B. Hultqvist and T. Hagfors) (Plenum Press: New York) 515.
- Haerendel, G., (1987) "On the potential role of concentrated field-aligned currents in solar physics" in *Small Scale Plasma Processes in the Solar Chromosphere/Corona, Interplanetary Medium and Planetary Magnetospheres*, Proceedings of 21st ESLAB Symposium, ESA SP-275 (Reidel: Dordrecht) 205.
- Haerendel, G., (1988) "Cosmic linear accelerators" in *Proceedings of an International School & Workshop on Plasma Astrophysics*, vol. 1, ESA SP-285 (Reidel: Dordrecht) 37.
- Haerendel, G., (1990) "Field-aligned currents in the Earth's magnetosphere" in *Physics of Magnetic Flux Ropes*, (ed. C. T. Russel, E. R. Priest and L. C. Lee) American Geophysical Union Monograph No. 58 (American Geophysical Union: Washington) 539.
- Haerendel, G., (1994) "Acceleration from field-aligned potential drops," *Astrophys. J. Suppl.*, **90**, 2.
- Hagyard, M. J., (1988) "Observed non-potential magnetic fields and the inferred flow of electric currents at a location of repeated flaring," *Solar Phys.*, **115**, 107.
- Hesse, M., (1991) "Recent developments in the theory of three-dimensional magnetic reconnection" in *Advances in Solar System Magnetohydrodynamics*, (ed. E. R. Priest) (Cambridge University Press: Cambridge) 221.
- Hesse, M. and Schindler, K., (1988a) "General magnetic reconnection, parallel electric fields, and helicity," *J. Geophys. Res.*, **93**, 5547.

- Hesse, M. and Schindler, K., (1988b) "A theoretical foundation of general magnetic reconnection," *J. Geophys. Res.*, **93**, 5559.
- Heyvaerts, J., Priest, E. R. and Rust, D. M., (1977) "An emerging flux model for the solar flare phenomena," *Astrophys. J.*, **216**, 123.
- Hollweg, J. V., (1972) "Supergranulation-driven Alfvén waves in the solar chromosphere and related phenomena," *Cosmic Electrodynamics*, **2**, 423.
- Hollweg, J. V., (1978) "Alfvén waves in the solar atmosphere," *Solar Phys.*, **56**, 305.
- Hollweg, J. V., (1981) "Alfvén waves in the solar atmosphere. II. Open and closed magnetic flux tubes," *Solar Phys.*, **70**, 25.
- Hollweg, J. V., (1984) "Resonances of coronal loops," *Astrophys. J.*, **277**, 392.
- Hudson, H. S., (1987) "Subphotospheric current systems and flares," *Solar Phys.*, **113**, 315.
- Hudson, H. S., (1994) "Thermal plasmas in the solar corona: the Yohkoh soft X-ray observations" in *Proceedings of Kofu Symposium*, (eds. S. Enome and T. Hirayama) NRO Report No. 360 (NRO: Minamisaku) 1.
- Hudson, H., Haisch, B. and Strong, K. T., (1994) "Comment on "The solar flare myth"," *J. Geophys. Res.* (preprint: in press).
- Ionson, J. A., (1982) "Resonant electrodynamic heating of stellar coronal loops: an LRC circuit analog," *Astrophys. J.*, **254**, 318.
- Ionson, J. A., (1984) "A unified theory of electrodynamic coupling in coronal magnetic loops: the coronal heating problem," *Astrophys. J.*, **276**, 357.
- Jackson, J. D., (1975) *Classical Electrodynamics*, 2nd ed. (John Wiley & Sons: New York).
- Kan, J. R., Akasofu, S.-I. and Lee, L. C., (1983) "A dynamo theory of solar flares," *Solar Phys.*, **84**, 153.
- Khan, J. I., (1989) "The cross-field resistance of the solar photosphere," *Proc. Astr. Soc. Aust.*, **7**, 13.
- Kosugi, T., (1993) "Hard X-ray solar flares observed by Yohkoh and particle acceleration" in *Physics of Solar and Stellar Coronae*, (eds. J. F. Linsky and S. Serio) G. S. Vaiana Memorial Symposium (Kluwer: Dordrecht) 131.
- Kosugi, T., (1994) "High-energy solar flare observations by Yohkoh: a review" in *Proceedings of Kofu Symposium*, (eds. S. Enome and T. Hirayama) NRO Report No. 360 (NRO: Minamisaku) 11.
- Kovitya, P. and Cram, L., (1983) "Electrical conductivity in sunspots and the quiet corona," *Solar Phys.*, **84**, 45.

- Krall, K. R., Smith, Jr., J. B., Hagyard, M. J., West, E. A. and Cummings, N. P., (1982) "Vector magnetic field evolution, energy storage, and associated photospheric velocity shear within a flare-productive active region," *Solar Phys.*, **79**, 59.
- Krall, N. A. and Trivelpiece, A. W., (1973) *Principles of Plasma Physics*, (McGraw-Hill: New York).
- Kuperus, M. and Raadu, M. A., (1974) "The support of prominences formed in neutral sheets," *Astron. Astrophys.*, **31**, 189.
- Lang, K. R., (1992) *Astrophysical Data*, vol. 1, Planets and Stars (Springer-Verlag: New York).
- Lau, Y. -T. and Finn, J. M., (1990) "Three-dimensional kinematic reconnection in the presence of field nulls and closed field lines," *Astrophys. J.*, **350**, 672.
- Leach, J. and Petrosian, V., (1981) "Impulsive phase of solar flares. I. Characteristics of high energy electrons," *Astrophys. J.*, **251**, 781.
- Leach, J. and Petrosian, V., (1983) "Impulsive phase of solar flares. II. Characteristics of the hard X-rays," *Astrophys. J.*, **269**, 715.
- Leka, K. D., Canfield, R. C., McClymont, A. N., de La Beaujardière, J.-F., Fan, Y. and Tang, F., (1993) "The morphology of flare phenomena, magnetic fields, and electric currents in active regions. II. NOAA active region 5747 (1989 October)," *Astrophys. J.*, **411**, 370.
- Lerche, I. and Low, B. C., (1980) "Cylindrical prominences and the magnetic influence of the photospheric boundary," *Solar Phys.*, **66**, 285.
- Lin, R. P. and Hudson, H. S., (1971) "10-100 keV electron acceleration and emission from solar flares," *Solar Phys.*, **17**, 412.
- Lin, R. P., Schwartz, R. A., Pelling R. M. and Hurley K. C., (1981) "A new component of hard X-rays in solar flares," *Astrophys. J.*, **251**, L109.
- Lin, Y. and Gaizauskas, V., (1987) "Coincidence between H $\alpha$  flare kernels and peaks of observed longitudinal electric current densities," *Solar Phys.*, **109**, 81.
- Low, B. C., (1977) "Evolving force-free magnetic fields. I. The development of the preflare stage," *Astrophys. J.*, **212**, 234.
- Machado, M. E., Moore, R. L., Hernandez, A. M., Rovira, M. G., Hagyard, M. J. and Smith Jr., J. B., (1988) "The observed characteristics of flare energy release. I. Magnetic structure at the energy release site," *Astrophys. J.*, **326**, 425.
- Martens, P. C. H., (1987) "Preflare energy build-up in a filament circuit," *Solar Phys.*, **107**, 95.
- Martens, P. C. H. and Kuin, N. P. M., (1989) "A circuit model for filament eruptions and two-ribbon flares," *Solar Phys.*, **122**, 263.

- Masuda, S. (1994). Hard X-ray sources and the Primary Energy Release Site in Solar Flares, University of Tokyo.
- Masuda, S., Kosugi, T., Hara, H., Tsuneta, S. and Ogawara, Y., (1994) "A loop-top hard X-ray source in a compact solar flare as evidence of magnetic reconnection," *Nature*, **371**, 495.
- McClymont, A. N. and Fisher, G. H., (1989) "On the mechanical energy available to drive solar flares" in *Solar System Plasma Physics*, (ed. J. H. Waite, J. L. Burch, & R. L. Moore) American Geophysical Union Monograph No. 54 (American Geophysical Union: Washington) 219.
- Melrose, D. B., (1990) "Particle acceleration processes in the solar corona," *Aust. J. Phys.*, **43**, 703.
- Melrose, D. B., (1991) "Neutralized and unneutralized current patterns in the solar corona," *Astrophys. J.*, **381**, 306.
- Melrose, D. B., (1992) "Energy propagation into a flare kernel during a solar flare," *Astrophys. J.*, **387**, 403.
- Melrose, D. B., (1993) "Solar flares: current dissipation or magnetic annihilation?," *Aust. J. Phys.*, **46**, 167.
- Melrose, D. B. and Dulk G. A., (1984) "Radio-frequency heating of the coronal plasma during flares," *Astrophys. J.*, **282**, 308.
- Melrose, D. B. and McClymont, A. N., (1987) "The resistances of the photosphere and of a flaring coronal loop," *Solar Phys.*, **113**, 241.
- Melrose, D. B. and White, S. M., (1981) "Precipitation from an asymmetric magnetic flux tube," *J. Geophys. Res.*, **86**, 2183.
- Moore, R. L., Hagyard, M. J. and Davis, J. M., (1987) "Flare research with the NASA/MSFC vector magnetograph: Observed characteristics of sheared magnetic fields that produce flares," *Solar Phys.*, **113**, 347.
- Moore, R. *et al.*, (1980) "The thermal X-ray flare plasma" in *Solar Flares*, (ed. P. A. Sturrock) (Colorado Associated University Press: Boulder, Colorado) 341.
- Moreton, G. E. and Severny, A. B., (1968) "Magnetic fields and flares in the region CMP 20 September 1963," *Solar Phys.*, **3**, 282.
- Morse, P. M. and Feshbach, H., (1953) *Methods of Theoretical Physics*, (McGraw-Hill: New York).
- Parker, E. N., (1979) *Cosmical Magnetic Fields: Their Origin and Their Activity*, (Clarendon: Oxford).
- Priest, E. R., (1982) *Solar Magnetohydrodynamics*, (D. Reidel: Dordrecht).

- Priest, E. R., (1992) "Basic magnetic configuration and energy supply processes for an interacting flux model of eruptive solar flares" in *Eruptive Solar Flares*, (eds. Z. Švestka, B. V. Jackson and M. E. Machado) Lecture Notes in Physics 399 (Springer-Verlag: Berlin) 15.
- Priest, E. R. and Forbes, T. G., (1989) "Steady magnetic reconnection in three dimensions," *Solar Phys.*, **119**, 211.
- Priest, E. R. and Forbes, T. G., (1990) "Magnetic field evolution during prominence eruptions and two ribbon flares," *Solar Phys.*, **126**, 319.
- Raadu, M. A., (1989) "The physics of double layers and their role in astrophysics," *Phys. Rep.*, **178**, 27.
- Romanov, V. A. and Tsap, T. T., (1990) "Magnetic fields and flare activity," *Sov. Astron.*, **34**, 656.
- Rosner, R., Low, B. C. and Holzer, T. E., (1986) "Physical processes in the solar corona" in *Physics of the Sun*, (ed. P. A. Sturrock) vol. 2, The Solar Atmosphere (D. Reidel: Dordrecht) 135.
- Rust, D. M., Sakurai, T., Gaizauskus, V., Hofman, A., Martin, S. M., Priest, E. R. and Wang, J., (1994) "Preflare state," *Solar Phys.*, **153**, 1.
- Scheurwater, R. (1989). *Generation and Propagation of Hydromagnetic Waves in Astrophysical Plasmas*, University of Utrecht.
- Scheurwater, R. and Kuperus, M., (1988) "Equivalent circuit representation of Alfvén waves," *Astron. Astrophys.*, **194**, 213.
- Schindler, K., Hesse, M. and Birn, J., (1991) "Magnetic field-aligned electric potentials in nonideal plasma flows," *Astrophys. J.*, **380**, 293.
- Scholer, M., (1970) "On the motion of artificial ion clouds in the magnetosphere," *Planet. Space Sci.*, **18**, 977.
- Sonnerup, B. U. Ö., Ip, J. and Phan, T.-D. , (1990) "Steady magnetic field reconnection" in *Physics of Magnetic Flux Ropes*, (ed. C. T. Russell, E. R. Priest and L. C. Lee) American Geophysical Union Monograph No. 58 (American Geophysical Union: Washington) 539.
- Spicer, D. S., (1982) "Magnetic energy storage and conversion in the solar atmosphere," *Space Sci. Rev.* , **31**, 350.
- Spicer, D. S. and Brown, J. C., (1980) "A classification scheme for solar flares," *Solar Phys.*, **67**, 385.
- Spitzer, L., (1962) *Physics of Fully Ionised Gases*, (Interscience: New York).
- Spruit, H. C., (1974) "A model of the solar convection zone," *Solar Phys.*, **34**, 277.
- Sturrock, P. A., (1980) "Flare models" in *Solar Flares*, (ed. P. A. Sturrock) a Monograph from the Skylab Solar Workshop II (Colorado Associated University Press: Boulder) 411.

- Sturrock, P.A., (1986) "Rapid fluctuations in solar flares" in *Rapid Fluctuations in Solar Flares*, (eds. B. R. Dennis, L. E. Orwig and A. L. Kiplinger) NASA Conference Publication 2449 (NASA Science and Technical Information Branch: Maryland) 1.
- Švestka, Z., (1976) *Solar Flares*, (D. Reidel: Holland).
- Takakura, T., Inada, M., Makishima, K., Kosugi, T., Sakao, T., Masuda, S., Sakurai, T. and Ogawara, Y., (1993) "Time variation of the hard X-ray image during the early phase of solar impulsive bursts," *Publ. Astron. Soc. Japan*, **45**, 737.
- Tanaka, K., (1986) "Solar flare X-ray spectra of Fe XXVI and Fe XXV from the Hinotori satellite," *Publ. Astron. Soc. Japan*, **38**, 225.
- Tsuneta S. *et al.*, (1991) "The soft X-ray telescope for the Solar-A mission," *Solar Phys.*, **136**, 37.
- van den Oord, G. H. J., (1990) "The electrodynamic of beam/return current systems in the solar corona," *Astron. Astrophys.*, **234**, 496.
- van Driel-Gesztelyi, L., Hofman, A., Démoulin, P., Schmieder, B. and Csepura, G., (1994) "Relationship between electric currents, photospheric motions, chromospheric activity, and magnetic field topology," *Solar Phys.*, **149**, 309.
- Van Tend, W. and Kuperus, M., (1978) "The development of coronal electric current systems in active regions and their relation to filaments and flares," *Solar Phys.*, **59**, 115.
- Vasyliunas, V. M., (1975) "Theoretical models of magnetic field line merging, 1," *Rev. Geophys. Space Sci.*, **13**, 303.
- Volwerk, M. (1993). *Strong Double Layers in Astrophysical Plasmas*, University of Utrecht.
- Wilkinson, L. K., Emslie, A. G. and Gary, G. A., (1992) "On neutralized currents in the solar corona," *Astrophys. J.*, **392**, L39.
- Zaitsev, V. V. and Stepanov, A. V., (1991) "On the dynamo theory of solar flares," *Sov. Astron.*, **35**, 189.
- Zaitsev, V. V. and Stepanov, A. V., (1992) "Towards the circuit theory of solar flares," *Solar Phys.*, **139**, 343.
- Zirin, H., (1988) *Astrophysics of the Sun*, (Cambridge University Press: Cambridge).
- Zwillinger, D., (1992) *Handbook of Differential Equations*, 2nd ed. (Academic Press: Boston).